Title

A SENSORIMOTOR TRANSFORMATION FOR IMAGE-STABILIZING EYE MOVEMENTS AND ITS IMPLICATIONS FOR DISEASE

Author

Harris, Scott Christopher

Publication Date

2024

Peer reviewed|Thesis/dissertation

A SENSORIMOTOR TRANSFORMATION FOR IMAGE-STABILIZING EYE MOVEMENTS AND ITS IMPLICATIONS FOR DISEASE

by
Scott Christopher Harris

DISSERTATION
Submitted in partial satisfaction of the requirements for degree of
DOCTOR OF PHILOSOPHY

in

Neuroscience

in the

GRADUATE DIVISION
of the
UNIVERSITY OF CALIFORNIA, SAN FRANCISCO

Approved:

DocuSigned by:
Evan Feinberg
A51CA4992E3C4CE...

Evan Feinberg
Chair

DocuSigned by:
Kevin Bender
DocuSigned by:

Kevin Bender

DocuSigned by:
Felice Dunn
DocuSigned by:

Felice Dunn

DocuSigned by:
Marla Feller
DocuSigned by:

Marla Feller

DocuSigned by:
Massimo Scanziani
4AF406E430B7472...

Massimo Scanziani

Committee Members

ACKNOWLEDGEMENTS

I am grateful to the mentors, colleagues, and experimental subjects who have encouraged me to continue learning.

CONTRIBUTIONS

The work presented in Chapter 2 of this dissertation is a reprint of content that appears in the following publication:

Harris, S. C., & Dunn, F. A. (2023). Asymmetric retinal direction tuning predicts optokinetic eye movements across stimulus conditions. *Elife*, *12*, e81780.

The data presented in Chapter 3 of this dissertation was collected in collaboration with Drs. Annika Balraj and Felice Dunn.

A SENSORIMOTOR TRANSFORMATION FOR IMAGE-STABILIZING EYE MOVEMENTS AND ITS IMPLICATIONS FOR DISEASE

SCOTT HARRIS

ABSTRACT

When an animal moves through its environment, relative motion between the eye and the world can blur vision. The optokinetic reflex is an innate behavior that counteracts this possibility by responding to the slippage of the visual scene on the retina with counteracting, image-stabilizing eye movements. Previous work identified that ON direction selective retinal ganglion cells, a particular class of motion-sensitive neuron in the retina, are responsible for detecting the global image motion that occurs during self-movement. However, it has been less clear how the information encoded by ON direction selective retinal ganglion cells is used by downstream circuits to inform eye movements. Here, I investigate these mechanisms in mice. Using a combination of electrophysiology, behavioral data, and computational modeling, I demonstrate that a linear subtraction of activity from ON direction selective retinal ganglion cells with different directional tunings can predict the trajectory of optokinetic eye movements across several conditions. I then show how this close connection between the activity of neurons in the retina and a measurable behavioral response can also be used to establish sensitive methods of disease detection. Together, this work demonstrates how deep mechanistic understandings of sensorimotor transformations can reveal important translational insights and applications.

TABLE OF CONTENTS

LIST OF FIGURES

List of Abbreviations

A/P	Anterior/Posterior, in reference to axes along the vertebrate body plan
AOS	The accessory optic system
ChAT	Choline acetyltransferase
DRP	Density recovery profile
DSI	Direction selectivity index
DT	Diphtheria toxin
DTR	Diphtheria toxin receptor, or transgenic mice expressing the diphtheria toxin receptor in M-opsin expressing photoreceptors
E/I	The ratio of excitatory post synaptic current to inhibitory post synaptic current as measured during voltage clamp recordings
EPSC	Excitatory post synaptic current, as measured in a voltage-clamp recording
HEPES	N-(2-Hydroxyethyl)piperazine-N′-(2-ethanesulfonic acid)
I-V	Current to voltage relationship
Inf	Inferior, in reference to Inferior ON direction selective retinal ganglion cells, or an inferiorly traversing visual stimulus
IPSC	Inhibitory post synaptic current, as measured in a voltage-clamp recording
IQR	Interquartile range
M/L	Medial/Lateral, in reference to axes along the vertebrate body plan
MTN	Medial terminal nucleus of the accessory optic system
LED	Light-emitting diode

LTN	Lateral terminal nucleus of the accessory optic system
ND	Null direction
NMDA	N-methyl-D-aspartate, in reference to the corresponding glutamate receptor
NOT/DTN	Nucleus of the optic tract/dorsal terminal nucleus of the accessory optic system
NSAID	Nonsteroidal anti-inflammatory drug
oDSGC	ON direction selective retinal ganglion cell
ooDSGC	ON-OFF direction selective retinal ganglion cell
OKR	Optokinetic reflex, also called optokinetic nystagmus
PD	Preferred direction
PFA	Paraformaldehyde
PSD-95	Post synaptic density protein 95
PSTH	Peristimulus time histogram
RGC	Retinal ganglion cell
SAC	Starburst amacrine cell
SEM	Standard error of the mean
Sup	Superior, in reference to Superior ON direction selective retinal ganglion cells, or a superiorly traversing visual stimulus
TTL	Transistor-to-transistor logic
VGluT3	Vesicular glutamate transporter 3
Vm	Subthreshold membrane potential, or membrane potential
VOR	Vestibulo-ocular reflex

CHAPTER 1. INTRODUCTION AND FRAMEWORK

1.1 Overview

The natural world is composed of an overwhelming amount of information. From microscopic molecules to colossal galaxies, matter and energy take a tremendous diversity of forms. To survive, organisms must attend to the narrow bands of information that are meaningful to their existence. For instance, the carnivorous plant *Dionaea muscipula* contains dedicated mechanosensory hairs along the surface of its foliage because it is critically important to know when a small insect crosses one of its leaves for the plant's capacity to acquire nutrients (Darwin, 1888; Volkov et al., 2008). *Dionaea muscipula* does not have receptors devoted to detecting 100-8000 Hz vocalizations, however, because it is much less concerned with listening in on human conversation (humans, in contrast, do have such receptors [Oxenham, 2018, Schwartz 2003]).

The evolutionary processes that guide the development of sensory apparati span millennia, but the results can be remarkably precise. In the mouse visual system, for instance, the spectral sensitivity of cone photoreceptors varies systematically across retinal topography to match the corresponding distribution of incident wavelengths from the mouse's natural environment (Qiu et al., 2021). Beyond photoreceptors, compact retinal circuits parse and process information, leading to neurons with increasingly complex tuning properties. The second-order bipolar cells are organized into ~15 types (Tsukamoto and Omi, 2017), while the tertiary retinal ganglion cells (RGCs) come in ~40 types that are each responsible for detecting a particular spatiotemporal pattern (or patterns) of light (Baden et al., 2016; Sanes and Masland, 2015). While it can sometimes

be more challenging to directly relate the tuning properties of RGCs to specific salient and behaviorally relevant features of the environment, their collective refinement is nonetheless apparent: as an early information bottleneck for vision, the population of RGC responses defines a basis set from which the remainder of visual neurons derive their tuning. Thus, only RGC types that encode ethologically relevant information are likely to survive evolutionary filters.

The refinement of sensory circuits over evolution can be interpreted in the context of efficiency (Barlow, 1961). In this framework, limited resources result in evolutionary pressures to capture the most salient information from the environment for the lowest biological cost. Center-surround organization, adaptation, and the spatial organization of retinal mosaics are each an example of how the visual system has evolved to favor efficiency (Buchsbaum et al., 1997; Doi et al., 2012; Huang and Rao, 2011; Meister and Berry, 1999; Pitkow and Meister, 2012; Roy et al., 2021). In the case of RGCs, physical space is a limited resource: in order to extract the maximum amount of information from a particular point in the visual scene, at least one RGC of each type must be packed into a small, overlapping retinal area. This, along with metabolic considerations, places an inherent limit on the possible number of RGC types. Thus, there is little room for waste, with each constituent RGC type serving a critical role for vision.

In this dissertation, I focus on a particular mammalian RGC type with an especially clear ethological function (Oyster, 1968; Oyster and Barlow, 1967; Patterson et al., 2022; Sun et al., 2006; Wang et al., 2023). Natural head and body movements cause displacement of the eye in space that can blur vision. ON direction selective retinal ganglion cells (oDSGCs) are tasked with detecting this blur so that it can be counteracted.

oDSGCs are tuned to encode the direction and speed of global image motion, called retinal slip, that arises during self-movement. This information is then passed to a handful of brainstem nuclei that move the eyes in the same direction as the slip so as to offset blur and preserve vision (Simpson, 1984). This compensatory behavior is called the optokinetic reflex (OKR), and its significance is underscored by the diversity of animals, from insects to humans, in which it is observed (Fenk et al., 2022; Masseck and Hoffmann, 2009; Zeil et al., 1989).

Here, my broad goal is to understand how the motion information captured by oDSGCs informs OKR behavior. Decades of work has established a close connection between oDSGCs and OKR. Manipulations that disrupt direction selectivity in oDSGCs similarly disrupt OKR (Yonehara et al., 2016; Yoshida et al., 2001). oDSGCs and OKR also have matched speed tuning (Oyster et al., 1972). Moreover, oDSGC axons exclusively project to - and are the only RGCs to innervate - the brainstem nuclei that are responsible for generating OKR (collectively referred to as the accessory optic system, AOS [Dhande et al., 2015; Giolli et al., 2006]). Together, this work has established the ethological relevance of oDSGCs in detecting the visual information that drives OKR. A substantial body of literature has also explored the neurobiological mechanisms that support oDSGC direction tuning and axon guidance (Al-Khindi et al., 2022; Euler et al., 2002; Lilley et al., 2019; Mani et al., 2023; Osterhout et al., 2015; Sivyer et al., 2019; Summers and Feller, 2022; Sun et al., 2015; Vaney et al., 2001; Wei, 2018; Wei et al., 2011; Yonehara et al., 2016, 2011; Yoshida et al., 2001). However, it is unclear exactly how information encoded by oDSGCs is parsed by downstream neurons in the visual system to adaptively produce behavior.

In Chapter 2, I ask how motion information from oDSGCs is used by the brain to inform behavior under normal, healthy conditions. A key result is that oDSGCs are highly sensitive to small, stimulus-derived input changes, and that this sensitivity is propagated to OKR behavior. This insight leads to the discovery that a highly linear model of brainstem processing is sufficient to account for how oDSGC activity is integrated to drive OKR. In Chapter 3, I ask how these processes change in disease. The data show that oDSGCs are similarly sensitive to input changes caused by photoreceptor degeneration as they are to stimulus-derived input changes. Moreover, this sensitivity is again propagated to OKR behavior, suggesting that the same linear model of brainstem processing may apply. This result positions OKR as a potentially valuable biomarker of mild degeneration.

Chapters 2 and 3 are independent explorations of oDSGC physiology and OKR behavior that are fully self-contained. When read together, however, they highlight the importance of connecting deep mechanistic understandings of sensory physiology with their significance for measurable behaviors. The fundamental role of sensory systems is to act as information filters - parsing the world for only that content which is most relevant to an organism, with the ultimate purpose of informing behavior. Grounding examinations of sensory systems in terms of how the information that they encode, and the ways that they encode it, influences organisms' ability to achieve their goals thus appropriately connects molecular and cellular physiology to the broader unraveling of ecology. After all, it is precisely ecological forces that have shaped the remarkable nuance and complexity of sensory systems over evolutionary timescales.

1.2 Related publications and other works

The work described in Chapter 2 of this dissertation has appeared in previous publications and conference proceedings (see *Contributions* for additional information):

- Harris, S. C., & Dunn, F. A. (2023). Asymmetric retinal direction tuning predicts optokinetic eye movements across stimulus conditions. Elife, 12, e81780.
- Harris, S. C., & Dunn, F. A. (2022). Asymmetries in the vertical optokinetic reflex result from disproportionate excitation to complementary ON direction-selective retinal ganglion cell types. Investigative Ophthalmology & Visual Science, 63(7), 47-47.

The work described in Chapter 3 of this dissertation has not been previously published. However, several manuscripts in preparation are expected to include these data and ideas. The tentative titles of these manuscripts include:

- Identification of a neural pathway with heightened sensitivity to mild neurodegeneration
- Objective methods for detecting early photoreceptor loss in retinitis pigmentosa

Related work which is not reported on in this dissertation includes the following:

- Della Santina, L., Yu, A. K., Harris, S. C., Soliño, M., Ruiz, T. G., Most, J., Kuo, Y. M., Dunn, F. A., & Ou, Y. (2021). Disassembly and rewiring of a mature converging excitatory circuit following injury. Cell reports, 36(5).

- Kiraly, J. K., Harris, S. C., Al-Khindi, T., Dunn, F. A., & Kolodkin, A. L. (2024). PyOKR: A Semi-Automated Method for Quantifying Optokinetic Reflex Tracking Ability. Journal of Visualized Research. JoVE (Journal of Visualized Experiments).
- Harris, S. C., & John, J. (2024). ScottHarris17/Bassoon: Bassoon (v1.2.0). Zenodo. https://doi.org/10.5281/zenodo.11089975

1.3 References

Al-Khindi, T., Sherman, M.B., Kodama, T., Gopal, P., Pan, Z., Kiraly, J.K., Zhang, H., Goff, L.A., du Lac, S., Kolodkin, A.L., 2022. The transcription factor Tbx5 regulates direction-selective retinal ganglion cell development and image stabilization. Curr. Biol. https://doi.org/10.1016/j.cub.2022.07.064

Baden, T., Berens, P., Franke, K., Román Rosón, M., Bethge, M., Euler, T., 2016. The functional diversity of retinal ganglion cells in the mouse. Nature 529, 345–350. https://doi.org/10.1038/nature16468

Barlow, H.B., 1961. Possible Principles Underlying the Transformations of Sensory Messages, in: Rosenblith, W.A. (Ed.), Sensory Communication. The MIT Press, pp. 216–234. https://doi.org/10.7551/mitpress/9780262518420.003.0013

Buchsbaum, G., Gottschalk, A., Barlow, H.B., 1997. Trichromacy, opponent colours coding and optimum colour information transmission in the retina. Proc. R. Soc. Lond. B Biol. Sci. 220, 89–113. https://doi.org/10.1098/rspb.1983.0090

Darwin, C., 1888. Insectivorous Plants. J. Murray.

Dhande, O.S., Stafford, B.K., Lim, J.-H.A., Huberman, A.D., 2015. Contributions of Retinal Ganglion Cells to Subcortical Visual Processing and Behaviors. Annu. Rev. Vis. Sci. 1, 291–328. https://doi.org/10.1146/annurev-vision-082114-035502

Doi, E., Gauthier, J.L., Field, G.D., Shlens, J., Sher, A., Greschner, M., Machado, T.A., Jepson, L.H., Mathieson, K., Gunning, D.E., Litke, A.M., Paninski, L., Chichilnisky, E.J., Simoncelli, E.P., 2012. Efficient Coding of Spatial Information in the Primate Retina. J. Neurosci. 32, 16256–16264. https://doi.org/10.1523/JNEUROSCI.4036-12.2012

Euler, T., Detwiler, P.B., Denk, W., 2002. Directionally selective calcium signals in dendrites of starburst amacrine cells. Nature 418, 845–852. https://doi.org/10.1038/nature00931

Fenk, L.M., Avritzer, S.C., Weisman, J.L., Nair, A., Randt, L., Mohren, T.L., Siwanowicz, I., Maimon, G., 2022. Muscles that move the retina augment compound-eye vision in Drosophila. Nature 612, 116–122. https://doi.org/10.1038/s41586-022-05317-5

Giolli, R.A., Blanks, R.H.I., Lui, F., 2006. The accessory optic system: basic organization with an update on connectivity, neurochemistry, and function, in: Büttner-Ennever, J.A. (Ed.), Progress in Brain Research, Neuroanatomy of the Oculomotor System. Elsevier, pp. 407–440. https://doi.org/10.1016/S0079-6123(05)51013-6

Huang, Y., Rao, R.P.N., 2011. Predictive coding. WIREs Cogn. Sci. 2, 580–593. https://doi.org/10.1002/wcs.142

Lilley, B.N., Sabbah, S., Hunyara, J.L., Gribble, K.D., Al-Khindi, T., Xiong, J., Wu, Z., Berson, D.M., Kolodkin, A.L., 2019. Genetic access to neurons in the accessory optic system reveals a role for Sema6A in midbrain circuitry mediating motion perception. J. Comp. Neurol. 527, 282–296. https://doi.org/10.1002/cne.24507

Mani, A., Yang, X., Zhao, T.A., Leyrer, M.L., Schreck, D., Berson, D.M., 2023. A circuit suppressing retinal drive to the optokinetic system during fast image motion. Nat. Commun. 14, 5142. https://doi.org/10.1038/s41467-023-40527-z

Masseck, O.A., Hoffmann, K.-P., 2009. Comparative Neurobiology of the Optokinetic Reflex. Ann. N. Y. Acad. Sci. 1164, 430–439. https://doi.org/10.1111/j.1749-6632.2009.03854.x

Osterhout, J.A., Stafford, B.K., Nguyen, P.L., Yoshihara, Y., Huberman, A.D., 2015. Contactin-4 Mediates Axon-Target Specificity and Functional Development of the Accessory Optic System. Neuron 86, 985–999. https://doi.org/10.1016/j.neuron.2015.04.005

Oxenham, A.J., 2018. How We Hear: The Perception and Neural Coding of Sound. Annu. Rev. Psychol. 69, 27–50. https://doi.org/10.1146/annurev-psych-122216-011635

Oyster, C.W., 1968. The analysis of image motion by the rabbit retina. J. Physiol. 199, 613–635. https://doi.org/10.1113/jphysiol.1968.sp008671

Oyster, C.W., Barlow, H.B., 1967. Direction-Selective Units in Rabbit Retina: Distribution of Preferred Directions. Science 155, 841–842. https://doi.org/10.1126/science.155.3764.841

Oyster, C.W., Takahashi, E., Collewijn, H., 1972. Direction-selective retinal ganglion cells and control of optokinetic nystagmus in the rabbit. Vision Res. 12, 183–193. https://doi.org/10.1016/0042-6989(72)90110-1

Patterson, S.S., Bembry, B.N., Mazzaferri, M.A., Neitz, M., Rieke, F., Soetedjo, R., Neitz, J., 2022. Conserved circuits for direction selectivity in the primate retina. Curr. Biol. CB 32, 2529-2538.e4. https://doi.org/10.1016/j.cub.2022.04.056

Pitkow, X., Meister, M., 2012. Decorrelation and efficient coding by retinal ganglion cells. Nat. Neurosci. 15, 628–635. https://doi.org/10.1038/nn.3064

Qiu, Y., Zhao, Z., Klindt, D., Kautzky, M., Szatko, K.P., Schaeffel, F., Rifai, K., Franke, K., Busse, L., Euler, T., 2021. Natural environment statistics in the upper and lower visual field are reflected in mouse retinal specializations. Curr. Biol. 31, 3233-3247.e6. https://doi.org/10.1016/j.cub.2021.05.017

Roy, S., Jun, N.Y., Davis, E.L., Pearson, J., Field, G.D., 2021. Inter-mosaic coordination of retinal receptive fields. Nature 592, 409–413. https://doi.org/10.1038/s41586-021-03317-5

Sanes, J.R., Masland, R.H., 2015. The Types of Retinal Ganglion Cells: Current Status and Implications for Neuronal Classification. Annu. Rev. Neurosci. 38, 221–246. https://doi.org/10.1146/annurev-neuro-071714-034120

Schwartz, D.A., Howe, C.Q., Purves, D., 2003. The Statistical Structure of Human Speech Sounds Predicts Musical Universals. J. Neurosci. 23, 7160–7168. https://doi.org/10.1523/JNEUROSCI.23-18-07160.2003

Simpson, J.I., 1984. The Accessory Optic System. Annu. Rev. Neurosci. 7, 13–41. https://doi.org/10.1146/annurev.ne.07.030184.000305

Sivyer, B., Tomlinson, A., Taylor, W.R., 2019. Simulated Saccadic Stimuli Suppress ON-Type Direction-Selective Retinal Ganglion Cells via Glycinergic Inhibition. J. Neurosci. 39, 4312–4322. https://doi.org/10.1523/JNEUROSCI.3066-18.2019

Summers, M.T., Feller, M.B., 2022. Distinct inhibitory pathways control velocity and directional tuning in the mouse retina. Curr. Biol. https://doi.org/10.1016/j.cub.2022.03.054

Sun, L.O., Brady, C.M., Cahill, H., Al-Khindi, T., Sakuta, H., Dhande, O.S., Noda, M., Huberman, A.D., Nathans, J., Kolodkin, A.L., 2015. Functional Assembly of Accessory Optic System Circuitry Critical for Compensatory Eye Movements. Neuron 86, 971–984. https://doi.org/10.1016/j.neuron.2015.03.064

Sun, W., Deng, Q., Levick, W.R., He, S., 2006. ON direction-selective ganglion cells in the mouse retina. J. Physiol. 576, 197–202. https://doi.org/10.1113/jphysiol.2006.115857

Tsukamoto, Y., Omi, N., 2017. Classification of Mouse Retinal Bipolar Cells: Type-Specific Connectivity with Special Reference to Rod-Driven AII Amacrine Pathways. Front. Neuroanat. 11. https://doi.org/10.3389/fnana.2017.00092

Vaney, D.I., He, S., Taylor, W.R., Levick, W.R., 2001. Direction-Selective Ganglion Cells in the Retina, in: Zanker, J.M., Zeil, J. (Eds.), Motion Vision. Springer Berlin Heidelberg, Berlin, Heidelberg, pp. 14–57. https://doi.org/10.1007/978-3-642-56550-2_2

Volkov, A.G., Adesina, T., Markin, V.S., Jovanov, E., 2008. Kinetics and Mechanism of Dionaea muscipula Trap Closing. Plant Physiol. 146, 694–702. https://doi.org/10.1104/pp.107.108241

Wang, A.Y.M., Kulkarni, M.M., McLaughlin, A.J., Gayet, J., Smith, B.E., Hauptschein, M., McHugh, C.F., Yao, Y.Y., Puthussery, T., 2023. An ON-type direction-selective ganglion cell in primate retina. Nature 1–6. https://doi.org/10.1038/s41586-023-06659-4

Wei, W., 2018. Neural Mechanisms of Motion Processing in the Mammalian Retina. Annu. Rev. Vis. Sci. 4, 165–192. https://doi.org/10.1146/annurev-vision-091517-034048

Wei, W., Hamby, A.M., Zhou, K., Feller, M.B., 2011. Development of asymmetric inhibition underlying direction selectivity in the retina. Nature 469, 402–406. https://doi.org/10.1038/nature09600

Yonehara, K., Balint, K., Noda, M., Nagel, G., Bamberg, E., Roska, B., 2011. Spatially asymmetric reorganization of inhibition establishes a motion-sensitive circuit. Nature 469, 407–410. https://doi.org/10.1038/nature09711

Yonehara, K., Fiscella, M., Drinnenberg, A., Esposti, F., Trenholm, S., Krol, J., Franke, F., Scherf, B.G., Kusnyerik, A., Müller, J., Szabo, A., Jüttner, J., Cordoba, F., Reddy, A.P., Németh, J., Nagy, Z.Z., Munier, F., Hierlemann, A., Roska, B., 2016. Congenital Nystagmus Gene FRMD7 Is Necessary for Establishing a Neuronal Circuit Asymmetry for Direction Selectivity. Neuron 89, 177–193. https://doi.org/10.1016/j.neuron.2015.11.032

Yoshida, K., Watanabe, D., Ishikane, H., Tachibana, M., Pastan, I., Nakanishi, S., 2001. A Key Role of Starburst Amacrine Cells in Originating Retinal Directional Selectivity and Optokinetic Eye Movement. Neuron 30, 771–780. https://doi.org/10.1016/S0896-6273(01)00316-6

Zeil, J., Nalbach, G., Nalbach, H.-O., 1989. Spatial Vision in a Flat World: Optical and Neural Adaptations in Arthropods, in: Singh, R.N., Strausfeld, N.J. (Eds.), Neurobiology of Sensory Systems. Springer US, Boston, MA, pp. 123–137. https://doi.org/10.1007/978-1-4899-2519-0_10

CHAPTER 2. ASYMMETRIC RETINAL DIRECTION TUNING PREDICTS OPTOKINETIC EYE MOVEMENTS ACROSS STIMULUS CONDITIONS

2.1 Introduction

From humans to insects, a wide range of organisms depend on vision to navigate their environments. When these animals respond to incoming visual information by enacting motor plans, however, relative motion is created between the eye and the visual scene. Such motion, termed 'retinal slip,' has the potential to corrupt subsequent vision and threaten survival. To compensate for this possibility, the optokinetic reflex (OKR) is a highly conserved visual behavior that stabilizes retinal image motion across species (including invertebrates [Zeil et al., 1989], reptiles, amphibians, fish, birds, and all mammals, reviewed by Masseck and Hoffmann, 2009). OKR consists of visually-evoked, compensatory eye movements (or head movements in some species) that offset the slow, global image motion generated by self-movement (Simpson, 1984). In most species, OKR also changes across stimulus conditions: adjustments to stimulus contrast, color, location, velocity, or spatial frequency, for example, can elicit distinct OKR patterns (Collewijn, 1969; Donaghy, 1980; Gravot et al., 2017; Knorr et al., 2021; Leguire et al., 1991; Cahill and Nathans, 2008; Dehmelt et al., 2021; Shimizu et al., 2010). Nonetheless, neurophysiological mechanisms for such phenomena remain unknown.

The anatomical pathways that underlie OKR in mammals are well defined (reviewed by Masseck and Hoffmann, 2009, Simpson, 1984, Dhande et al., 2015, Giolli et al., 2006). Starting in the retina, a dedicated class of biological motion detectors known as ON direction-selective retinal ganglion cells (oDSGCs) encode the slow global image motion that occurs during retinal slip. Classic work identified three types of oDSGCs that

each spike maximally in response to a different cardinal direction of stimulus motion (i.e., upward/superior, downward/inferior, and nasal/anterior) (Oyster, 1968; Oyster and Barlow, 1967). A recent study also identified a fourth oDSGC type in mice that encodes temporal/posterior motion (Sabbah et al., 2017). Projections from oDSGCs avoid typical retinorecipient structures such as the superior colliculus and lateral geniculate nucleus. Instead, axons from vertically and horizontally preferring oDSGCs course along dedicated retinofugal tracts to a set of midbrain nuclei known collectively as the accessory optic system. Vertically tuned oDSGCs terminate exclusively in, and comprise the sole retinal inputs to, the medial and lateral terminal nuclei (MTN and LTN) (Dhande et al., 2015; Dhande et al., 2013; Lilley et al., 2019; Sun et al., 2015; Yonehara et al., 2008; Yonehara et al., 2009; van der Togt et al., 1993, but see Kay et al., 2011 and '2.3 Discussion') - though in mice, LTN is engulfed within MTN (Dhande et al., 2013; Yonehara et al., 2009; Osterhout et al., 2015; Pak et al., 1987). Here, their inputs are likely integrated into a single velocity signal that reflects the vertical component of retinal slip. This information is then relayed deeper into the brainstem where corresponding eye movements are enacted. Likewise, horizontally tuned oDSGCs exclusively target the nucleus of the optic tract/dorsal terminal nucleus (NOT/DTN) where their signals are similarly integrated to ultimately generate the horizontal component of OKR (Dhande et al., 2013; Osterhout et al., 2015). While correlations have been recognized between the physiological properties of oDSGCs and OKR – particularly a matched speed tuning (Oyster et al., 1972) – little is known about how signals from multiple oDSGC types are integrated to generate OKR across varying stimulus conditions (Dhande et al., 2015; Wei, 2018).

Here, we reveal a general mechanism by which OKR may be generated across a range of stimulus statistics. First, we focus on a single parameter that is known to affect OKR: motion direction. In many species, including both humans (Takahashi et al., 1978; Hainline et al., 1984; Murasugi and Howard, 1989; van den Berg and Collewijn, 1988) (but see Knapp et al., 2013) and mice (Yonehara et al., 2009), OKR is more robust in response to superior motion than inferior motion. We aim to illuminate the mechanism underlying this asymmetry in order to reveal more general processes by which oDSGC signals are centrally integrated to produce OKR. Focusing on the directional asymmetry of vertical OKR is methodologically strategic in that (1) it limits the source of possible neurophysiological mechanisms to functions of only the vertical OKR pathway, and (2) unlike horizontal OKR, which relies on interhemispheric communication and mirror-image motion signals from each eye (Masseck and Hoffmann, 2009; Dhande et al., 2013; Hoffmann and Fischer, 2001), vertical OKR can be studied unilaterally. Our results indicate that the behavioral asymmetry between superior and inferior OKR is linked to differences in the direction tuning properties of oDSGCs that prefer superior and inferior motion. These physiological differences arise from a shift in the balance of excitatory and inhibitory (E/I) synaptic inputs across cell types, along with nonlinear transformations associated with spike thresholding. More generally, we demonstrate that motion encoding in vertically tuned oDSGCs is uniquely sensitive to such changes in synaptic input weights and show how this sensitivity, along with a central subtraction of oDSGC activity, can account for changes to OKR across additional stimulus conditions in behaving mice.

2.2 Results

2.2.1 OKR is more robust in the superior than inferior direction

Across species, superior motion generates a more robust OKR than inferior motion (e.g., cat [Hoffmann and Fischer, 2001; Evinger and Fuchs, 1978; Grasse and Cynader, 1988], chicken [Wallman and Velez, 1985], monkey [Takahashi and Igarashi, 1977], human [Takahashi et al., 1978; Hainline et al., 1984; Murasugi and Howard, 1989; van den Berg and Collewijn, 1988]). In mice, this phenomenon has been reported in juvenile animals (Yonehara et al., 2009). To investigate whether an asymmetry between superior and inferior OKR exists in adult mice, we designed a behavioral rig to accurately evoke and quantify vertical OKR in head-fixed animals (**Figure 2.1A and B**, **2.2**) (Denman et al., 2017). Eye movements were measured in response to vertically drifting, full-field gratings used previously to evoke OKR (Sun et al., 2015; Yonehara et al., 2009; Osterhout et al., 2015; Yonehara et al., 2016). Across all adult mice, superior- and inferior-drifting gratings generated distinct, but reproducible eye movements: while superior gratings elicited repetitive slow, upward-drifting eye movements (‘slow nystagmus’) interleaved with frequent resetting saccades in the opposite direction (‘fast nystagmus’) (**Figure 2.1C**), inferior gratings tended to reliably drive only an initial slow nystagmus immediately following stimulus onset, after which fast nystagmuses were infrequent and eye position changed minimally (**Figure 2.1D**). To quantify these differences, we isolated periods of slow and fast nystagmus post hoc by extracting saccadic eye movements from the raw eye position trace. Superior stimuli elicited more frequent fast nystagmuses than did inferior stimuli (**Figure 2.1E**). In addition, the total distance traveled during slow

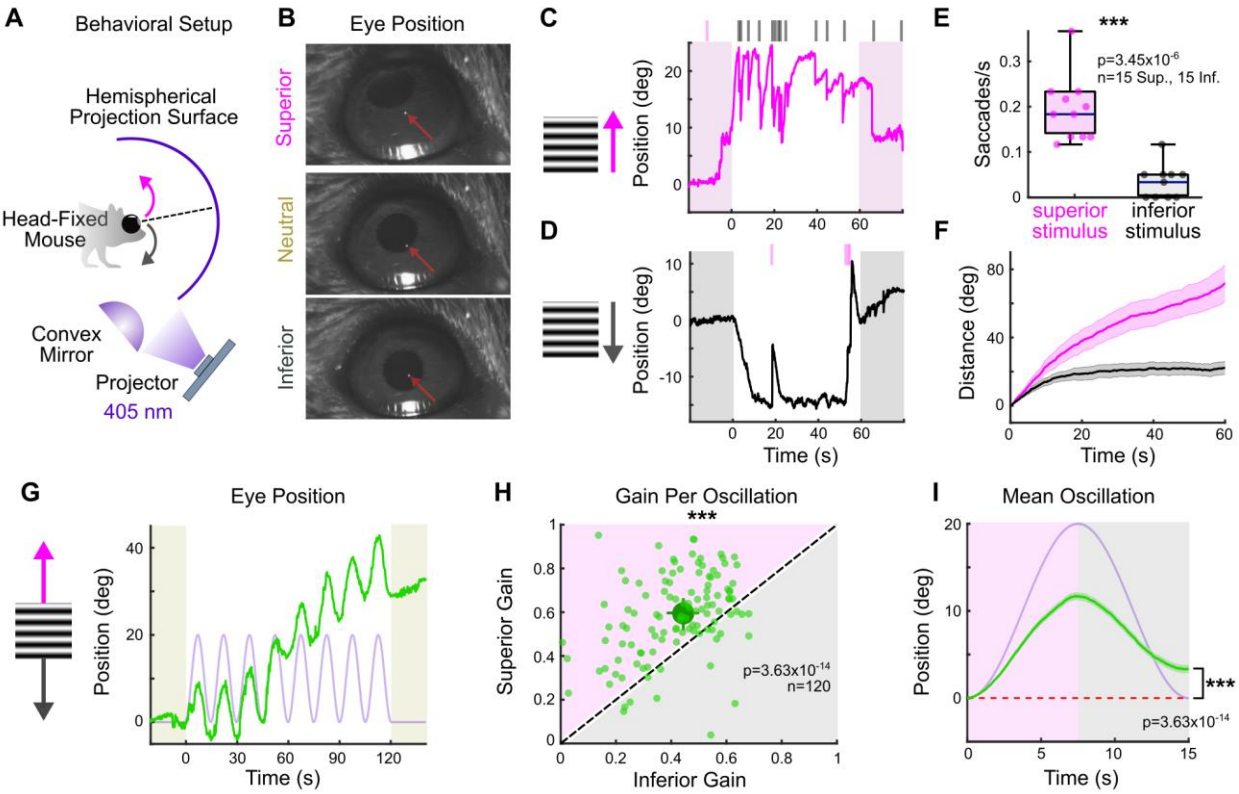

Figure 2.1 The superior and inferior optokinetic reflex (OKR) are asymmetric in adult mice

(Figure caption continued on the next page)

(Figure caption continued from the previous page)

(**A**) Schematic of the behavioral setup to elicit the vertical OKR. The mouse is situated so that one eye is centered in a hemisphere. Stimuli are projected onto the hemisphere's concave surface via a convex mirror. Eye movements are tracked using an infrared-sensitive camera and a corneal reflection. (**B**) Example video frames demonstrating that the eye traverses between superior, neutral, and inferior positions in the presence of vertically drifting sinusoidal gratings. Red arrows mark the infrared corneal reflection. (**C, D**) Example of OKR in response to full contrast (**C**) superior and (**D**) inferior unidirectional drifting gratings (10°/s). For each epoch, a continuous 60 s stimulus was flanked by 20 s of a static grating (shaded regions). Ticks above the plots mark fast nystagmus in the superior (magenta) or inferior (gray) direction. Examples from one animal. (**E**) Rate of vertical fast nystagmus for superior and inferior stimuli on each epoch for N = 5 mice. Horizontal line represents median, box boundaries are the interquartile range (IQR), whiskers represent most extreme observation within 1.5× IQR. (**F**) Cumulative vertical distance traveled during slow nystagmus in response to superior (magenta) and inferior (gray) drifting gratings (mean ± SEM). (**G**) Example of OKR in response to a vertically oscillating sinusoidal grating. The eye position in green, and the stimulus position in lavender. Fast nystagmuses have been removed to reveal the asymmetry between superior and inferior OKR. For each epoch, animals viewed eight oscillation cycles lasting a total of 120 s, flanked by 20 s of a static grating (shaded regions). (**H**) Average gain of slow nystagmus during the superior versus inferior stage of individual oscillations. Small dots are a single oscillation. The region of magenta (or gray) indicates that gain was greater for the superior (or inferior) stage. Points that fall on the line indicate equivalent gain for both stimulus directions. Large dot and whiskers represent univariate medians and 95% confidence intervals (via bootstrapping), respectively. Significance value indicates whether the points tend to fall unevenly on one side of the unity line (two-sided signed-rank). (**I**) Eye position (green) and stimulus position (lavender) averaged across all oscillations and all animals (mean ± SEM). Starting eye position is normalized to 0° at cycle onset. The average ending eye position is displaced in the superior direction (two-sided signed-rank). N = 5 mice for all experiments; n = number of trials. *p<0.05, **p<0.01, ***p<0.001.

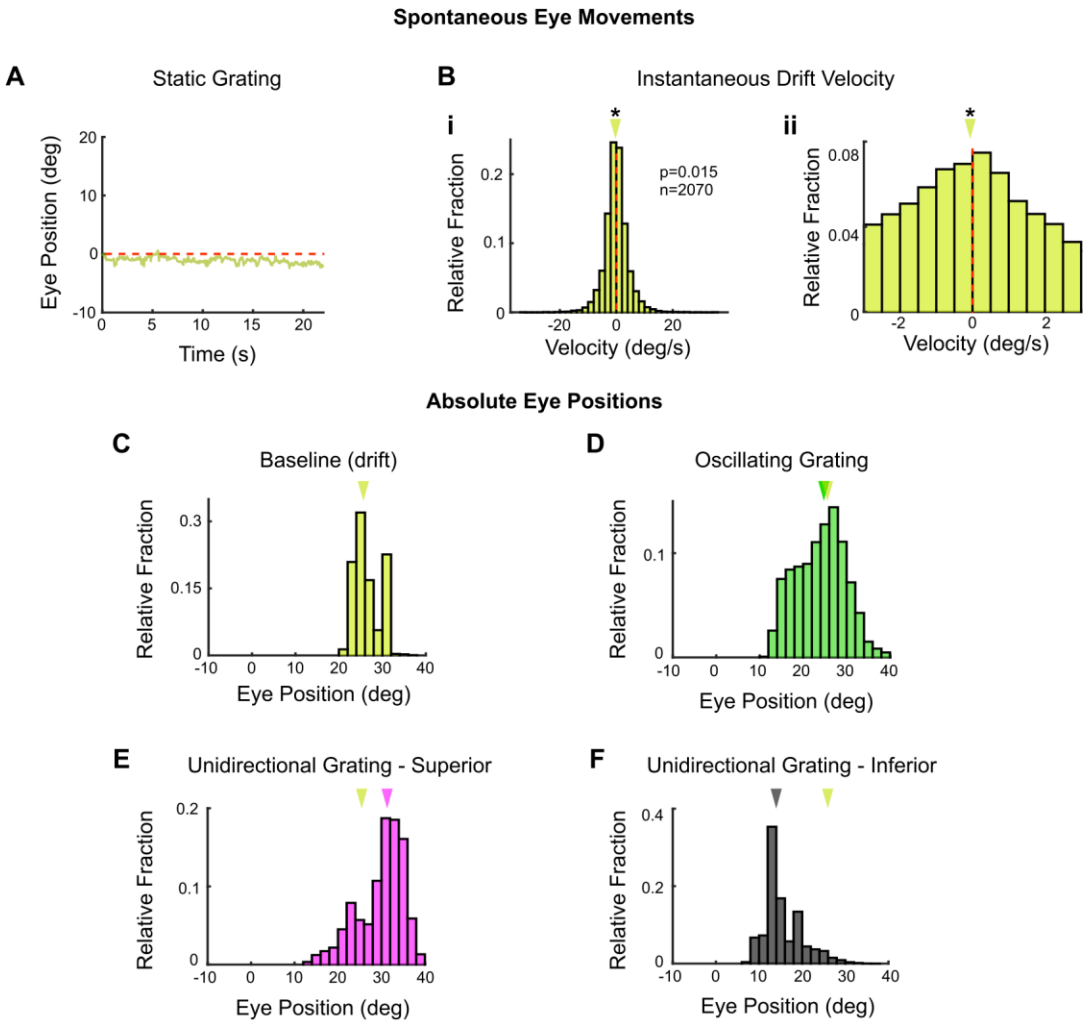

Figure 2.2 Baseline vertical eye movements in head-fixed mice.

(Figure caption continued on the next page)

(Figure caption continued from the previous page)

Vertical eye movements were measured in response to static gratings to calculate eye drifts for baseline subtraction. (**A**) Example raw eye trace over 22 s of a static grating. The calculated position of the eye drifts downward over time, which could reflect true eye movements or a calibration error in our recording configuration. These two possibilities cannot be disambiguated (see 'Materials and methods'). The magnitude of eye position drift during static gratings is approximately 18-fold less than the magnitude of the eye movements elicited by high-contrast drifting gratings. (**B**) Distribution of instantaneous eye velocity across N = 5 animals for the 20 s prior to the onset of all drifting grating stimuli (unidirectional and oscillating gratings at high [full] and low [20% relative] contrasts) used to evoke the optokinetic reflex (OKR). On average, there is a slight bias toward inferior (i.e., downward/negative) eye velocities during this baseline period, with a median velocity of –0.0787°/s. (**Bi**) Full distribution. (**Bii**) Same data, zoomed in on 0° to reveal the inferior bias. (**C–F**) Absolute vertical position of the eye without drift correction (**C**) prior to stimulus onset (when the drift was calculated as in [**B]**, includes data from high (full) and low (20% relative) contrast, oscillating and unidirectional experiments), and during (**D**) high-contrast oscillating gratings, (**E**) superior unidirectional gratings and (**F**) inferior unidirectional gratings. Absolute eye position is similar to that measured during baseline only for oscillating gratings. The eye moves to more extreme positions during unidirectional stimuli. For this reason, the baseline subtraction was only applied to eye movements measured in response to oscillating gratings. For all histograms, arrows mark the median of the distribution. Yellow arrow in (**D–F**) marks the median of the distribution shown in (**C**). See **Figure 2.27** for further data on eye drift in response to low-contrast gratings. *p<0.05, **p<0.01, ***p<0.001.

nystagmus was greater for superior stimuli (**Figure 2.1F**). These results demonstrate that vertical OKR is asymmetric in adult mice.

Despite the stark asymmetry between superior and inferior OKR in response to unidirectional drifting gratings, quantifying OKR gain (ratio of eye velocity to stimulus velocity) under these conditions presented challenges due to variability in the OKR waveform across stimulus directions (**Figure 2.1C and D**). To better quantify gain, we designed a second stimulus in which a grating oscillated sinusoidally between superior and inferior motion while retaining a constant average position. This oscillating grating evoked sequential superior and inferior slow nystagmuses that were phase-locked to the stimulus (**Figure 2.1G, 2.3**). Moreover, gain tended to be higher during the superior stage compared to the inferior stage of individual oscillations (**Figure 2.1H**). This bias was reflected by an average offset of vertical eye position in the superior direction over the course of a single stimulus oscillation (**Figure 2.1I**). Taken together, these results demonstrate that superior motion drives a more robust OKR than inferior motion.

2.2.2 Superior and Inferior oDSGCs have distinct direction tuning properties

While behavioral asymmetries between superior and inferior OKR could arise anywhere along the vertical OKR pathway, a plausible neurophysiological substrate is at the level of the retina where the pathways that encode superior and inferior motion remain distinct. Further, because the ganglion cells that encode superior motion (‘Superior oDSGCs’) and inferior motion (‘Inferior oDSGCs’) together serve as an information bottleneck for the remainder of the pathway, any physiological asymmetry between these cell types will propagate to behavior unless specifically corrected for by subsequent circuitry (see ‘2.3 Discussion’). Thus, we hypothesized that the behavioral asymmetry

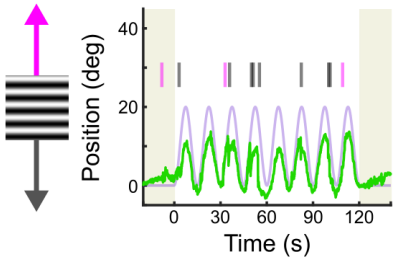

Figure 2.3 Example of sinusoidal vertical optokinetic reflex (OKR) before saccade removal.

Eye position (green) is plotted across time as a full-field grating oscillates vertically (lavender). The eye trace includes saccades (i.e., 'fast nystagmuses,' as indicated by tick marks: magenta for superior, gray for inferior). Saccades tend to occur in the opposite direction as the 'slow nystagmus' and do not facilitate image stabilization. However, saccades are necessary to keep the eye centered in its orbit. Removing these resetting saccades from the eye trace isolates the slow nystagmus component and reveals the asymmetry between superior and inferior OKR (**Figure 2.1G**).

between superior and inferior OKR may result from physiological differences between Superior and Inferior oDSGCs.

To probe oDSGCs involved in vertical OKR, we made central injections of a fluorescent retrograde tracer into their central target, MTN (**Figure 2.4A, 2.5**). This approach labeled an average of 669 ± 15 retinal ganglion cells (RGCs; N = 20 retinae) across the contralateral retina (**Figure 2.4B, 2.5**). Retrogradely labeled RGCs were then targeted in ex vivo retinae for electrophysiological investigation using epifluorescence, and we independently validated these data by using two-photon targeting in a separate set of experiments (**Figure 2.7, 2.8**; epifluorescence targeting was used for all experiments unless otherwise specified in the figure legends). To investigate the direction tuning properties of MTN-projecting RGCs, we made cell-attached recordings from labeled RGCs while presenting a drifting bar stimulus that moved slowly (10°/s) across the retina in eight directions (**Figure 2.4C**). The parameters of this stimulus matched those of the gratings used to evoke vertical OKR in behaving animals (i.e., equivalent cycle width, wavelength, and speed to the unidirectional gratings). The majority (94.76%) of retrogradely labeled RGCs were direction-selective and preferred either dorsal-to-ventral (n = 116 of 286) (i.e., Superior oDSGCs because these cells detect superior motion in visual space after accounting for inversion of the image by the eye's optics; **Figure 2.4D**) or ventral-to-dorsal (i.e., Inferior oDSGCs, n = 155 of 286) motion on the retina (**Figure 2.4E**). In agreement, mosaic analyses of soma locations indicated that retrogradely labeled cells likely consisted of two RGC types (**Figure 2.5**). Both Superior and Inferior oDSGCs invariably had baseline firing rates of approximately 0 Hz (spikes/s: Sup. 0.0134 ± 0.006; Inf. 0.0338 ± 0.016; p=0.13 Sup. vs. Inf.). Nonetheless, Superior

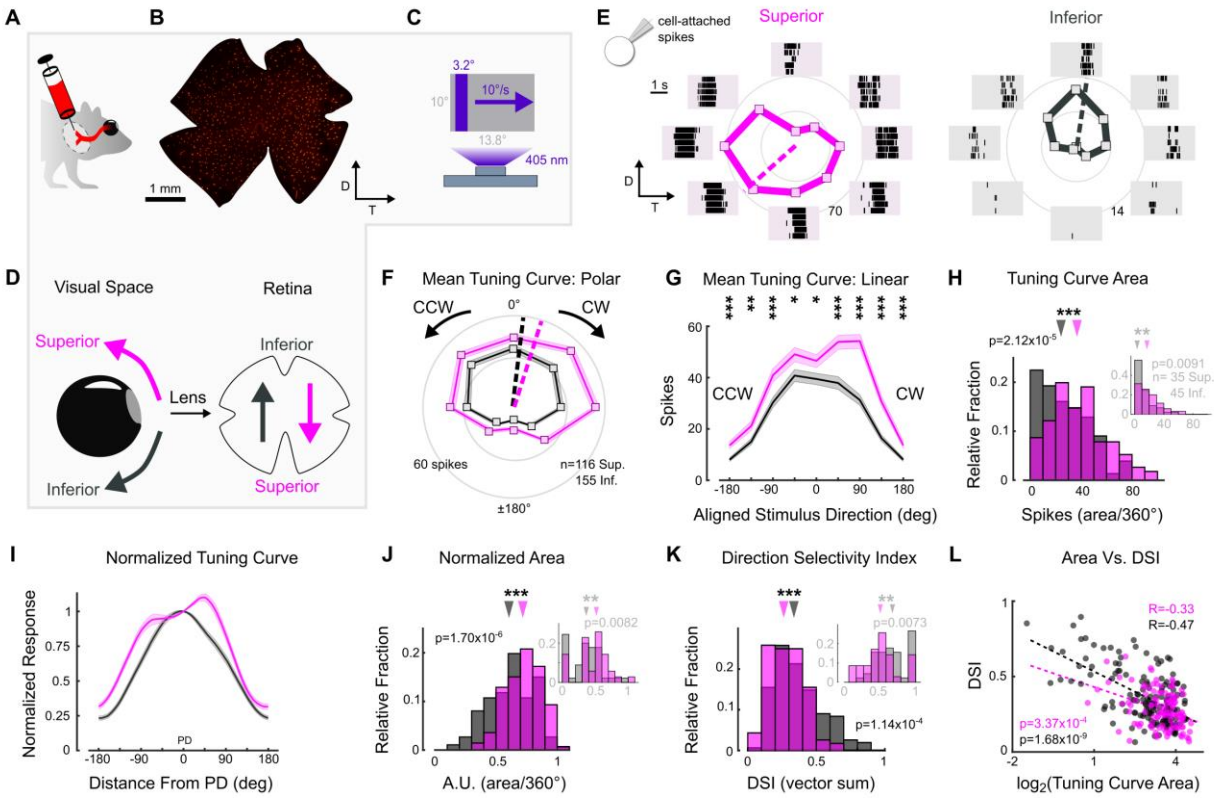

Figure 2.4 Superior and Inferior ON direction-selective retinal ganglion cells (oDSGCs) have asymmetric spike tuning curves.

(Figure caption continued on the next page)

(Figure caption continued from the previous page)

(**A**) Schematic illustrating unilateral bead injections into medial terminal nucleus (MTN) to retrogradely label ganglion cells in the contralateral retina. (**B**) Flat-mount retina with retrogradely labeled, MTN-projecting retinal ganglion cells. (**C**) Drifting bar stimulus (3.2° × limiting projector dimension, 10°/s, 2.4 × 10^4 S-cone photoisomerization/s). (**D**) Definitions of superior (magenta) and inferior (gray) motion in visual space and on the retina. Directions are inverted by the lens. (**E**) Cell-attached spikes from labeled, MTN-projecting retinal ganglion cells in a flat-mount retina in response to a bar drifting in eight directions. Spike responses and average tuning curves from example Superior (left, magenta) and Inferior (right, gray) oDSGCs. Mean spike counts are presented as the distance from the origin, marked by concentric circles. Numbers on circles indicate spike counts. Dashed lines represent the preferred direction of each cell, calculated as the direction of the vector sum of all responses. Coordinates are in retinal space. (**F, G**) Population tuning curves across all Superior and Inferior oDSGCs (mean ± SEM). (**F**) Polar plots (as in [**E**]) aligned by rotating the tuning curves of Superior cells by 180°. (**G**) Linear representation of the same data (referred to as the 'linear tuning curve'). CW: clockwise, nasal for Superior oDSGCs, temporal for Inferior oDSGCs; CCW: counterclockwise, temporal for Superior oDSGCs, nasal for Inferior oDSGCs. 0° represents directly superior/inferior motion. (**H**) Histograms of the area under the curve of the linear tuning curve of every cell. Inset shows the same metric for a stimulus at 20% relative contrast. (**I**) Population mean (± SEM) normalized tuning curves – computed by normalizing and aligning (at 0°) the response of each cell to its response in the preferred direction. (**J**) Histograms of the area under the curve of the normalized tuning curve (as in [**I**]) of every cell (referred to as 'normalized area'). A larger normalized area indicates a wider tuning curve. Inset shows the same metric for a stimulus at 20% relative contrast. (**K**) Histograms of the direction selectivity index (DSI, vector sum, see 'Materials and methods') of every cell. Inset shows the same metric for a stimulus at 20% relative contrast. (**L**) Linear tuning curve area (as in [**H**]) and direction selectivity index (as in [**K**]) were correlated on a cell-by-cell basis for both Superior and Inferior oDSGCs. Dashed lines are least squares linear regressions, R and p values are Spearman's rank correlation coefficient and associated two-sided significance value, respectively. For all histograms, medians of Superior (magenta) and Inferior (gray) oDSGC distributions are indicated by arrows. *p<0.05, **p<0.01, ***p<0.001.

oDSGCs tended to produce more total spikes than Inferior oDSGCs in response to the drifting bar stimulus (**Figure 2.4F and G**), and the total areas of their tuning curves were greater (**Figure 2.4H, 2.7A**). Similarly, we noticed topographic differences within cell types, with MTN-projecting RGCs in dorsal retina spiking more than those in ventral retina (**Figure 2.9**). However, the firing rates of Superior and Inferior oDSGCs covaried, with Superior oDSGCs spiking more than Inferior oDSGCs in every retinal quadrant (**Figure 2.8**).

We wondered whether the difference in response magnitude between Superior and Inferior oDSGCs could be explained by a simple scaling difference of their tuning curves (i.e., same shape, different size) or whether it was instead associated with an asymmetry in tuning curve shape. To answer this question, we normalized and aligned the tuning curve of each cell in our dataset to its preferred direction (vector sum) response (**Figure 2.4I**). If the tuning curves of Superior oDSGCs were scaled versions of those of Inferior oDSGCs, then this normalization and alignment procedure would eliminate any apparent differences between cell types. Instead, however, we found that the normalized tuning curves of Superior oDSGCs had greater widths at 50% response magnitude (**Figure 2.6A**) and total areas (**Figure 2.4J**, **2.7C**), indicating that their tuning curves were broader than those of Inferior oDSGCs. In agreement, circular Gaussian fits (see 'Materials and methods') of Superior oDSGC tuning curves were consistently wider than those of Inferior oDSGCs (**Figure 2.6B**). To understand how this difference in tuning curve width might affect the ability of Superior and Inferior oDSGCs to encode motion, we quantified the direction selectivity index (DSI) of each cell (magnitude of the vector sum divided by the scalar sum). In agreement, the DSIs of Superior oDSGCs were lower than

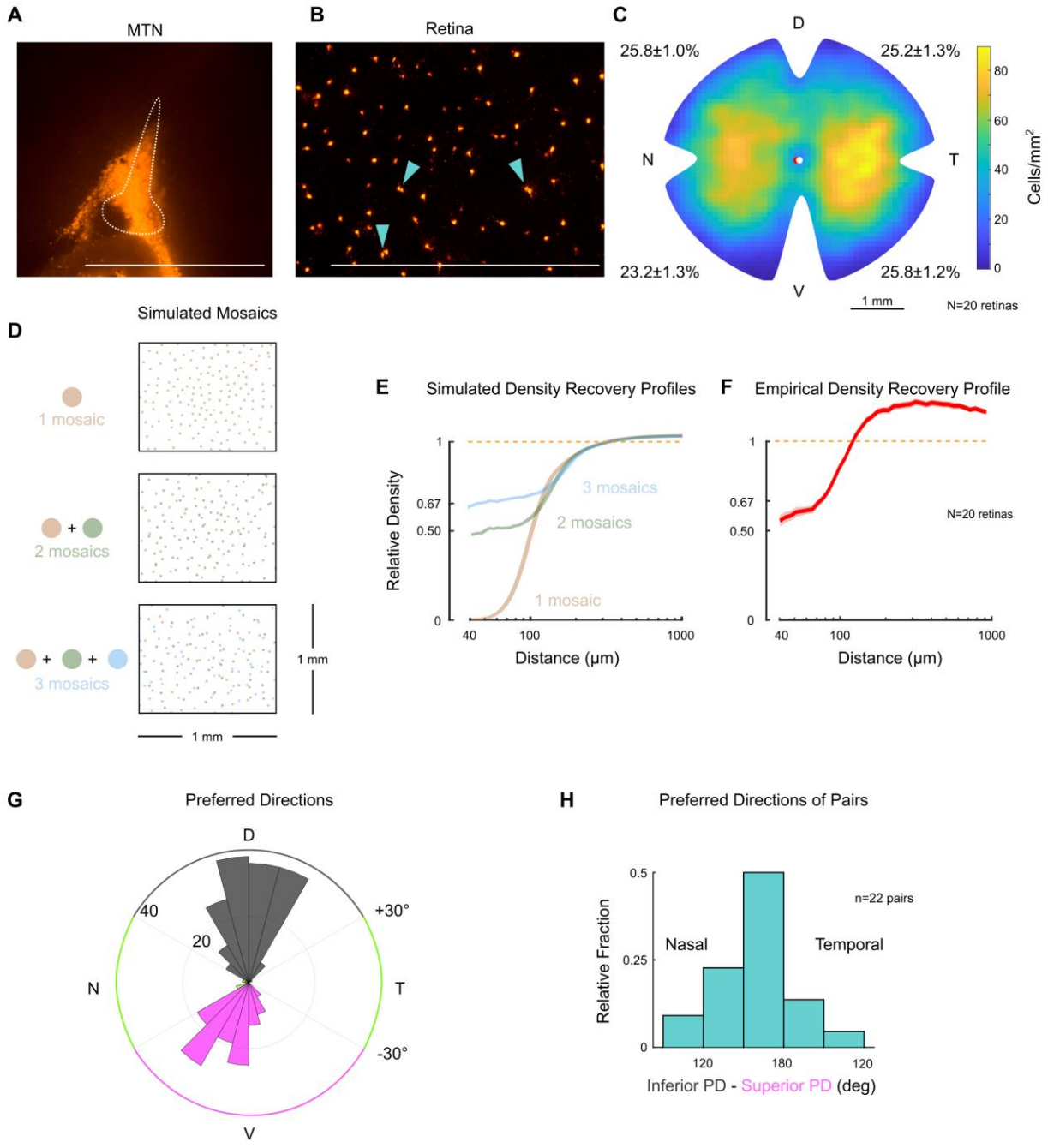

Figure 2.5 Two retinal ganglion cell types project to the medial terminal nucleus.

(Figure caption continued on the next page)

(Figure caption continued from the previous page)

(**A**) Sagittal section of medial terminal nucleus (MTN) following injection of fluorescent retrobeads (scale bar = 1mm). Dotted line outlines MTN. (**B**) Retrogradely labeled retinal ganglion cell somas in a flat-mount retina after contralateral MTN injection. Arrowheads point to examples where labeled cells form 'pairs' (i.e., are within 30 μm of each other; scale bar = 1 mm), as described previously (Yonehara et al., 2008). (**C**) Density heatmap of retrogradely labeled MTN-projecting retinal ganglion cells across the contralateral retina. Numbers around the perimeter indicate the percentage of cells found in each quadrant (mean ± SEM). D, T, V, and N denote dorsal, temporal, ventral, and nasal directions, respectively, on the retina. Pairwise comparisons of the average number of cells per quadrant did not reveal any significant differences. However, comparing across halves showed that densities were marginally greater in dorsal compared to ventral retina ($p=0.047$), and in temporal compared to nasal retina ($p=0.021$). (**D**) Simulations of retinal ganglion cell populations that consist of one (top), two (middle), and three (bottom) mosaics. Each simulation contains approximately the same number of total cells. When only one mosaic is present (top), cells obey exclusion zones and do not cluster next to each other. When more than one mosaic is present, cells do not respect the exclusion zones of other cell types and 'pairs' (middle) and 'trios' (bottom) begin to form. Retinal ganglion cells of distinct types are well known to tile the retina in separate mosaics. (**E**) Mean density recovery profiles (DRPs) for simulated retinal ganglion cell populations of one (tan), two (green), and three (blue) mosaics (n = 30 repetitions each). Only single mosaics exhibit a complete exclusion zone. The DRP of two mosaics converges to 50% of its average density (dashed line) as distance approaches 0, and the DRP of three mosaics converges to 67% of its average density. More generally, a spatial distribution of ganglion cells will converge to $n-1/n\times100\%$ of its average density, where n is the total number of mosaics (Cook and Podugolnikova, 2001). (**F**) DRP measured from retrogradely labeled MTN-projecting retinal ganglion cells (mean ± SEM). The empirical DRP lacks a full exclusion zone and converges to ~50% of its average density (1.0), indicating that there are likely two ganglion cell types, each forming an independent mosaic. Note that the DRP overshoots 1.0 within the shown domain because ON direction-selective retinal ganglion cells (oDSGCs) are not uniformly distributed across the retina (as shown in [**C**]). Normalizing to the peak density yields similar results. (**G**) Polar histogram of preferred directions measured in cell-attached mode across retrogradely labeled retinal ganglion cells identified by epifluorescence targeting. Colored segments of the outer circle indicate preferred direction thresholds for classification of Superior (magenta), Inferior (gray), and other direction-selective retinal ganglion cells (green). Coordinates are in retinal space. Concentric circles indicate the number of cells per bin. Labeled retinal ganglion cells divide into two major physiological types: superior-preferring and inferior-preferring. Only a small fraction of cells prefer horizontal directions (green). (**H**) Preferred directions of retrogradely labeled cells found in pairs (somas within 30 μm of each other). Paired cells tend to prefer opposite directions of motion (180° apart), further indicating that (1) two separate populations of ganglion cells project to MTN and (2) each population forms an independent mosaic.

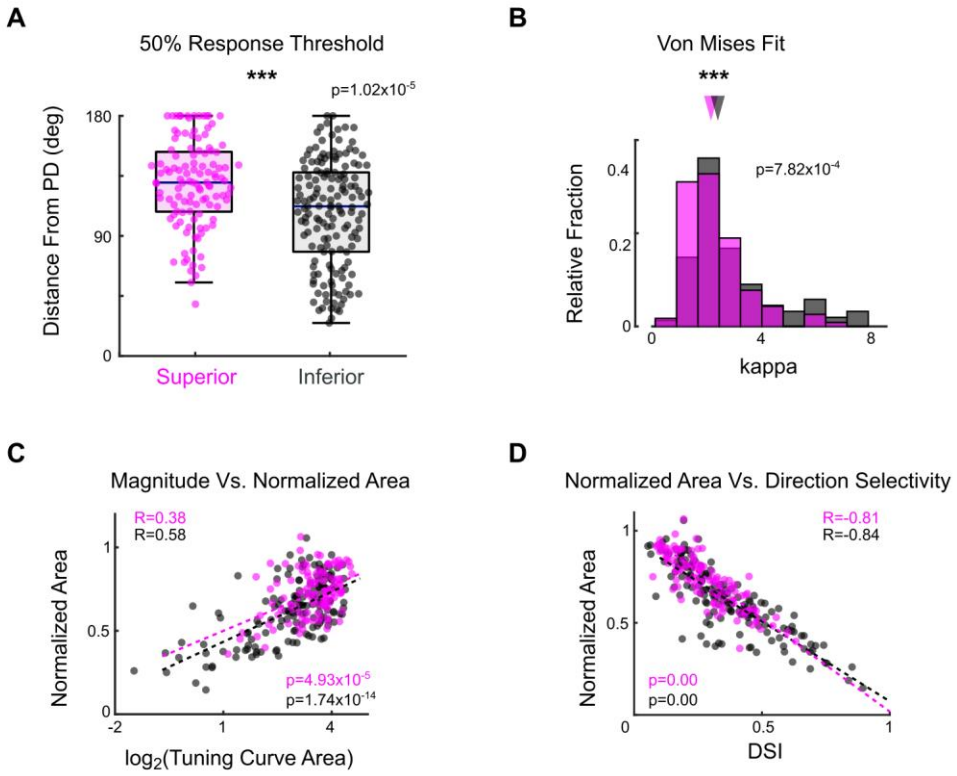

Figure 2.6 Additional metrics of ON direction-selective retinal ganglion cell (oDSGC) spike tuning curve width.

(**A**) Distributions of the distance (in degrees) from each cell's preferred direction to the point at which its response magnitude first drops below 50% of the response in the preferred direction. Larger values indicate a wider tuning curve. Horizontal line represents median, box boundaries are the IQR, and whiskers represent most extreme observation within 1.5× IQR. Points represent individual cells. (**B**) Histograms of the kappa parameter for the Von Mises fit of the tuning curve of each cell (see 'Materials and methods'). A smaller kappa value indicates a wider tuning curve. (**C**) The area of the linear tuning curve and the area of the normalized tuning curve were positively correlated on a cell-by-cell basis. (**D**) The direction selectivity index and the area of the normalized tuning curve were negatively correlated on a cell-by-cell basis. Dashed lines in (**C**) and (**D**) are least-squares linear regressions for Superior (magenta) and Inferior (gray) oDSGCs. R and p values are the Spearman's rank correlation coefficient and associated two-sided significance, respectively. *p<0.05, **p<0.01, ***p<0.001.

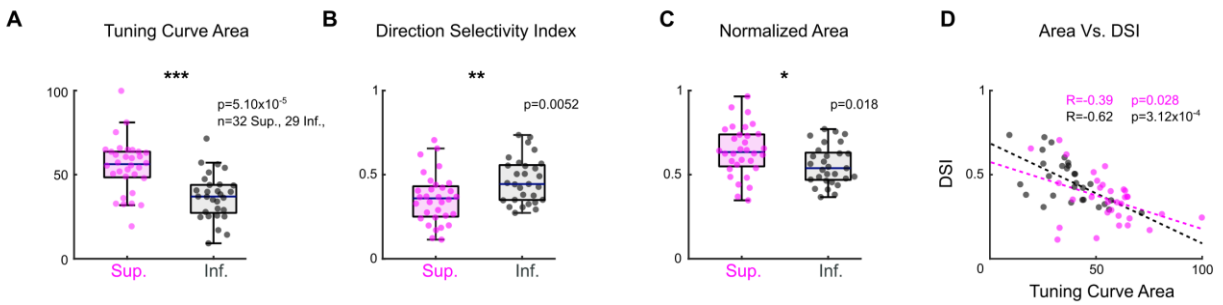

Figure 2.7 Asymmetries between Superior and Inferior ON direction-selective retinal ganglion cells (oDSGCs) persist under two-photon targeting.
Retrogradely labeled oDSGCs were targeted for cell-attached recordings using a two-photon laser (860 nm). Spikes were measured from Superior and Inferior oDSGCs in response to the drifting bar stimulus. Under two-photon conditions, Superior oDSGCs had (**A**) greater area of the linear tuning curve, (**B**) lower direction selectivity indices, and (**C**) greater area of the normalized tuning curve compared to Inferior oDSGCs. (**D**) Direction selectivity and tuning curve area were significantly correlated on a cell-by-cell basis for both Superior and Inferior oDSGCs. Dashed lines are least-squares linear regressions for Superior (magenta) and Inferior (gray) oDSGCs. R and p values are the Spearman's rank correlation coefficient and associated two-sided significance, respectively. These findings confirm the results from experiments in which ganglion cells were targeted by epifluorescence (Figure 2.4, 2.6). Cells in this two-photon dataset come from tissue that was never exposed to epifluorescence. No cell is in both the epifluorescence and two-photon datasets. *p<0.05, **p<0.01, ***p<0.001.

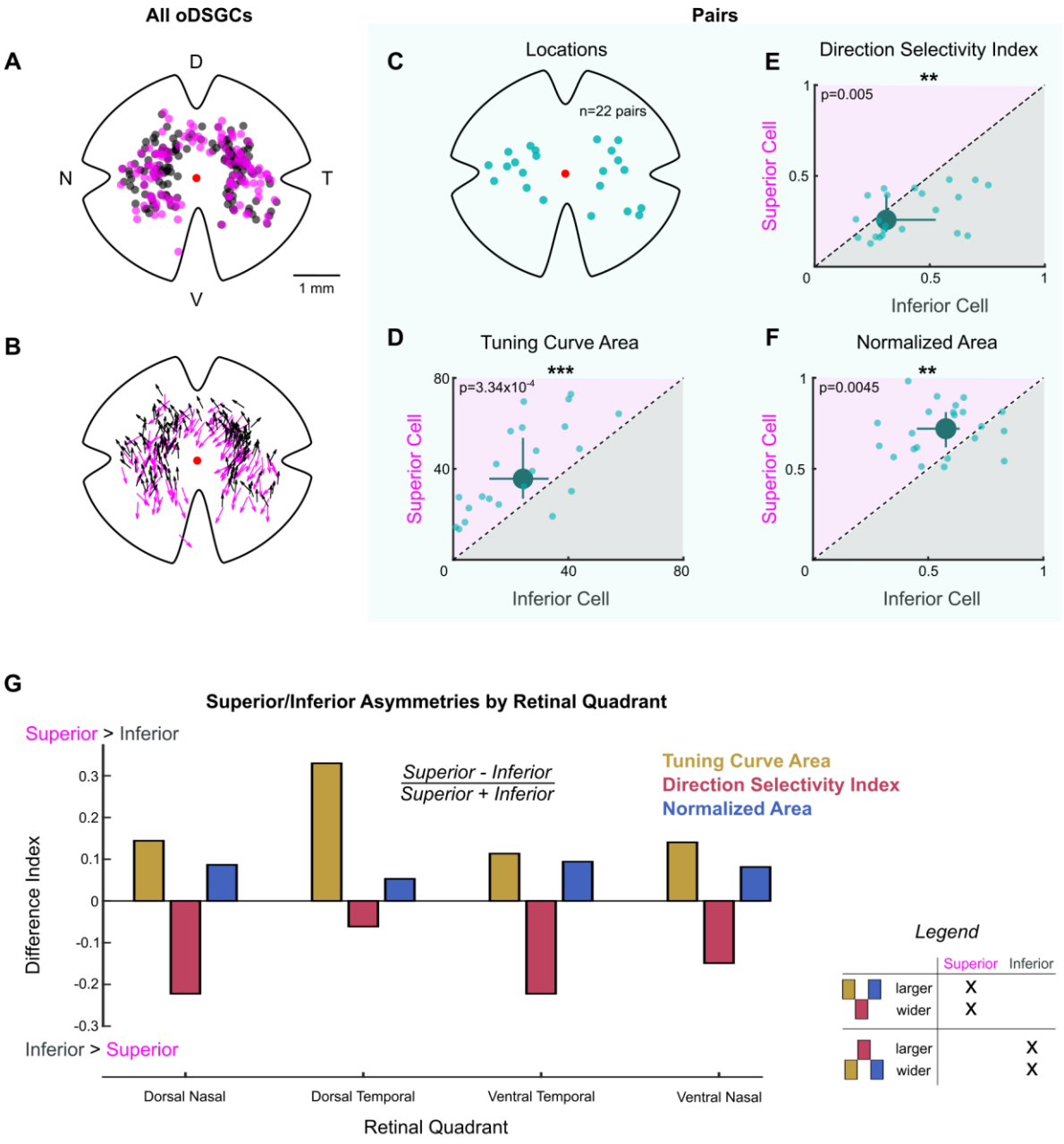

Figure 2.8 Physiological differences between Superior and Inferior ON direction-selective retinal ganglion cells (oDSGCs) are consistent across retinal topography.

(Figure caption continued on the next page)

(Figure caption continued from the previous page)

(**A**) Map of retinal locations of all medial terminal nucleus (MTN)-projecting retinal ganglion cells recorded during cell-attached experiments in which epifluorescence targeting was used. D, T, V, and N denote dorsal, temporal, ventral, and nasal directions, respectively, on the retina and apply to all maps. (**B**) Map of the preferred direction of each cell in (**A**). The arrow base marks the location of the cell soma. The arrowhead points in the preferred direction. Preferred directions varied systematically across the retina, as reported previously (Sabbah et al., 2017). (**C–F**) Data from Superior and Inferior oDSGCs that formed 'pairs' (i.e., somas within 30 μm of each other, see **Figure 2.5**). Pairwise comparisons in these cells remove potential confounds caused by differences in topographic distributions when looking for asymmetries across Superior and Inferior oDSGC populations. (**C**) Retinal location of each recorded pair. (**D–F**) Tuning curve metrics for the Superior and Inferior oDSGCs in each pair: (**D**) linear tuning curve area, (**E**) direction selectivity index, and (**F**) area of the normalized tuning curve. Dashed lines indicate unity. Large points represent the univariate medians. Whiskers are 95% confidence intervals for each median, determined via bootstrapping. Significance values indicate pairwise comparisons between Superior and Inferior oDSGCs (two-sided signed-rank). Superior oDSGCs spike more (**D**), are less direction-selective (**E**), and have wider tuning curves (**F**) when compared to the Inferior oDSGCs with which they form pairs. (**G**) Comparison of tuning curve metrics between Superior and Inferior oDSGCs found in each retinal quadrant. Bars show a difference index [(Superior - Inferior)/(Superior +Inferior)] calculated from the median linear tuning curve area (olive), direction selectivity index (red), or area of the normalized tuning curve (blue) per quadrant for each oDSGC type. Positive values indicate that the metric is greater for Superior cells in that quadrant and negative values indicate that the metric is greater for Inferior cells in that quadrant. Difference indices are bound between –1 and 1. Within each retinal quadrant, Superior oDSGCs have a larger linear tuning curve area, a lower direction selectivity index, and a larger normalized tuning curve area than Inferior oDSGCs. Data match the first possibility illustrated in the legend. *$p<0.05$, **$p<0.01$, ***$p<0.001$.

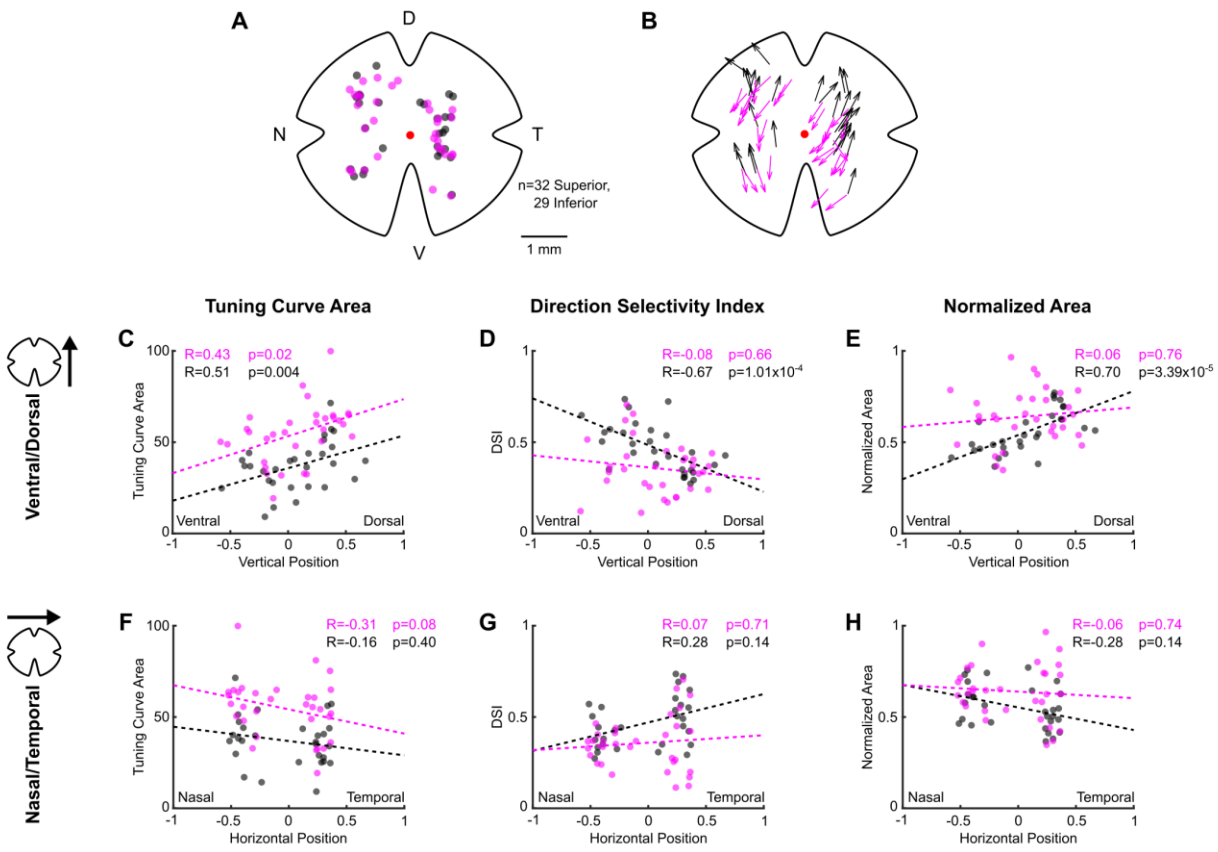

Figure 2.9 Topographic variation in direction tuning properties across the retina revealed by two-photon targeting.

(Figure caption continued on the next page)

(Figure caption continued from the previous page)

(**A**) Map of retinal locations of all medial terminal nucleus (MTN)-projecting retinal ganglion cells recorded during cell-attached experiments in which two-photon targeting was used. D, T, V, and N denote dorsal, temporal, ventral, and nasal directions, respectively, on the retina and apply to all maps. (**B**) Map of the preferred direction of each cell in (**A**). The arrow base marks the location of the cell soma. The arrowhead points in the preferred direction. Preferred directions varied systematically across the retina, as seen using epifluorescence targeting (**Figure 2.8B**) and as reported previously (Sabbah et al., 2017). (**C–H**) Scatter plots of tuning curve metrics as a function of each cell's position along either the ventral-dorsal (**C–E**) or nasal-temporal (**F–H**) axis of the retina. Coordinates are normalized to the size of the retina from which each cell was recorded (normalized coordinates range between –1 and 1, see 'Materials and methods'). Inferior ON direction-selective retinal ganglion cells (oDSGCs) change tuning curve size (**C**) and width (**D, E**) as a function of dorsal-ventral location, whereas only the tuning curve size (**C**) of Superior oDSGCs is modulated along the same axis. No metric is significantly related to position along the nasal-temporal axis for either cell type (**F–H**). Further, Superior oDSGCs tend to have larger and wider tuning curves than Inferior oDSGCs across all dimensions (separation between magenta and gray lines). For all scatter plots, dashed lines are least-squares linear regressions for Superior (magenta) and Inferior (gray) oDSGCs. R and p values are the Spearman's rank correlation coefficient and associated two-tailed significance, respectively. Two-photon targeting was used for all data in this figure so as to avoid confounds associated with epifluorescence exposure and photoreceptor absorption spectra gradients across retinal topography.

those of Inferior oDSGCs (**Figure 2.4K**, **2.7B**). Finally, we tested whether these asymmetries persisted across stimulus conditions by using a drifting bar stimulus with fivefold lower contrast. As before, Superior oDSGCs spiked more and had broader tuning curves in response to lower contrast bars (**Figure 2.4H**, **J and K insets**).

Together, these data indicate that asymmetries in vertical OKR are concomitant with prominent physiological differences between Superior and Inferior oDSGCs: Superior oDSGCs not only spike more than Inferior oDSGCs, but also have broader tuning curves. Further, tuning curve size (i.e., area of the unnormalized tuning curve) and width (i.e., direction selectivity index) were correlated on a cell-by-cell basis (**Figure 2.4L**, **2.7D**), indicating that asymmetries in these metrics could arise from a common mechanism.

2.2.3 Superior oDSGCs receive more excitatory input than Inferior oDSGCs

We sought to determine the source of tuning curve asymmetries between Superior and Inferior oDSGCs. As in the more widely studied class of direction-selective retinal ganglion cell known as the ON-OFF DSGC (ooDSGC) (Briggman et al., 2011; Fried et al., 2002; Wei et al., 2011; Ding et al., 2016), oDSGCs inherit the bulk of their direction selectivity via greater inhibition from starburst amacrine cells (SACs) in response to null direction stimuli (Amthor et al., 2002; Yonehara et al., 2011; Yoshida et al., 2001; reviewed by Wei, 2018, Mauss et al., 2017, Vaney et al., 2012). Therefore, we postulated that the difference in tuning curve width between Superior and Inferior oDSGCs may result from asymmetric inhibitory inputs between the two cell types.

To investigate this possibility, we made whole-cell voltage-clamp recordings at the reversal potential for excitation to isolate inhibitory inputs to Superior and Inferior oDSGCs

in response to the drifting bar stimulus (**Figure 2.10A and B**). Across cells, we found no significant difference in the magnitude of inhibitory postsynaptic currents (IPSCs) between Superior and Inferior oDSGCs (**Figure 2.10C**, **2.11A**). IPSCs in Superior oDSGCs, however, were slightly more direction-selective than those in Inferior oDSGCs (**Figure 2.10D**), which is unlikely to explain their broader spike tuning curves (see '2.3 Discussion'). Thus, the canonical model of retinal direction selectivity involving inhibition cannot account for the differences between Superior and Inferior oDSGC spike tuning curves.

We next asked whether excitatory inputs could better explain the asymmetries between the spike tuning curves of Superior and Inferior oDSGCs. To test this possibility, we made voltage-clamp recordings at the reversal potential for inhibition to isolate excitatory postsynaptic currents (EPSCs) during the drifting bar stimulus (**Figure 2.10E and F**). Across stimulus directions, EPSCs in Superior oDSGCs were between 1.4 and 2.3 times greater than those in Inferior oDSGCs (**Figure 2.10G, 2.11B**). EPSCs were also less direction-selective in Superior than in Inferior oDSGCs (**Figure 2.10H**). In agreement, the ratio of the peak EPSC to the peak IPSC (E/I) was greater for Superior oDSGCs than for Inferior oDSGCs (**Figure 2.10I, 2.11C**), though not different in direction selectivity (**Figure 2.10J**). We found no difference in the relative timing of peak EPSCs and peak IPSCs across cell types (not shown). Based on these results, the difference in spike tuning curve size and shape between Superior and Inferior oDSGCs may be related to a corresponding shift in the balance of E/I, associated with an asymmetry in the amount of net excitation that each cell type receives.

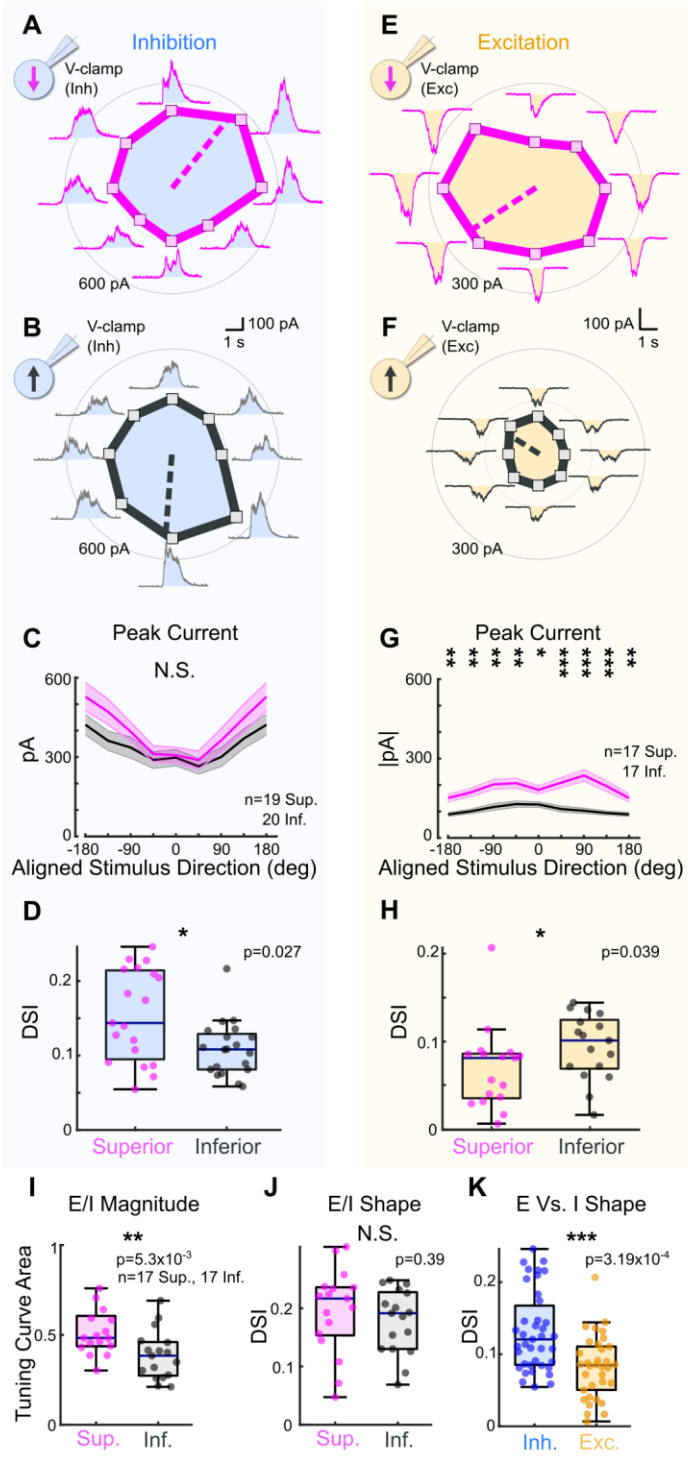

Figure 2.10 Superior ON direction-selective retinal ganglion cells (oDSGCs) receive similar inhibitory inputs but greater excitatory inputs compared to Inferior oDSGCs.

(Figure caption continued on the next page)

(Figure caption continued from the previous page)

(**A**) Inhibitory currents measured from an exemplar Superior oDSGC under voltage-clamp at +10 mV in response to a bar drifting in eight directions. Mean peak inhibitory current is presented as the distance from the origin for each stimulus direction. Dashed line indicates the preferred direction of the peak inhibitory currents. Coordinates are in retinal space. (**B**) Same as (**A**) for an exemplar Inferior oDSGC. (**C**) Population responses for peak inhibitory currents across stimulus directions for Superior (magenta) and Inferior (gray) oDSGCs (mean ± SEM). Stimulus directions are aligned across cell types, where 0° indicates directly superior (for Superior oDSGCs) or inferior (for Inferior oDSGCs) motion. Positive directions are clockwise. (**D**) Distributions of the direction selectivity index for peak inhibitory currents in individual Superior and Inferior oDSGCs. (**E**) Excitatory currents measured from an exemplar Superior oDSGC under voltage-clamp at –60 mV in response to a bar drifting in eight directions. Same cell as in (**A**). (**F**) Same as (**E**) for an exemplar Inferior oDSGC. Same cell as in (**B**). (**G**) Population responses for peak excitatory currents across stimulus directions for Superior (magenta) and Inferior (gray) oDSGCs (mean ± SEM). (**H**) Distributions of the direction selectivity index for peak excitatory currents in individual Superior and Inferior oDSGCs. (**I, J**) The ratio of the peak excitatory current to the peak inhibitory current (E/I) was calculated for each stimulus direction for cells in which both metrics were recorded. (**I**) Distributions of the linear tuning curve area of E/I. (**J**) Distributions of the direction selectivity index for E/I. (**K**) Direction selectivity index for peak inhibitory (blue) and excitatory (yellow) currents collapsed across Superior and Inferior oDSGCs. For box plots, horizontal line represents median, box boundaries are IQR, and whiskers represent the most extreme observation within 1.5× IQR. *p<0.05, **p<0.01, ***p<0.001.

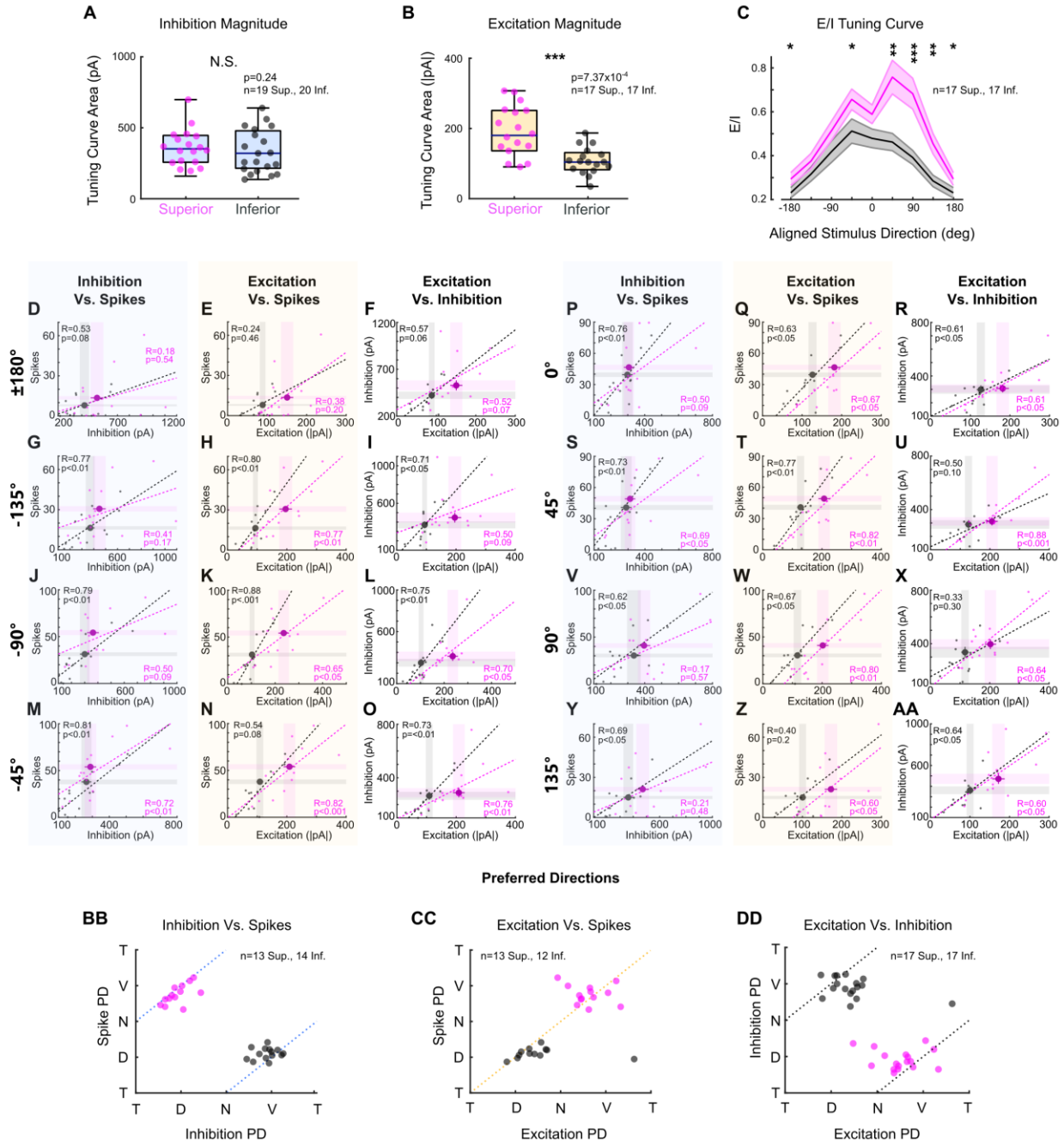

Figure 2.11 Superior ON direction-selective retinal ganglion cells (oDSGCs) receive more excitatory input, but are less intrinsically excitable, than Inferior oDSGCs.

(Figure caption continued on the next page)

(Figure caption continued from the previous page)

(**A, B**) Linear tuning curve areas of the peak (**A**) inhibitory and (**B**) excitatory current measured in voltage-clamp recordings. Horizontal line represents median, box boundaries are IQR, and whiskers represent most extreme observation within 1.5× IQR. (**C**) Ratio of peak excitatory to peak inhibitory current (E/I) for each aligned stimulus direction (mean ± SEM), for cells in which both metrics were measured. 0° is directly superior (for Superior oDSGCs) or inferior (for Inferior oDSGCs) motion. Positive directions are clockwise. Statistical significance for each stimulus direction changes depending on how the tuning curves of Superior and Inferior oDSGCs are aligned (e.g., 180° rotation vs. reflection over the x-axis of the polar tuning curve). In general, E/I of Superior oDSGCs is greater than that of Inferior oDSGCs. (**D–AA**) For each bar direction, inhibition vs. spikes, excitation vs. spikes, and excitation vs. inhibition for cells in which both metrics were recorded (excitation and inhibition are peak values from voltage-clamp recordings, spikes are counts from cell-attached recordings). Dashed lines are least-squares linear regressions for Superior (magenta) and Inferior (gray) oDSGCs. R and p values are the Spearman's rank correlation coefficient and associated two-sided significance, respectively. Large points represent univariate means ± SEM for each cell type taken from full data sets (i.e., small dots represent only a subset of cells in which both metrics were recorded, but full univariate datasets also consist of cells in which just one metric was recorded). Directions indicate aligned stimulus directions (as in [**C**]). For excitation vs. spikes, the fit line for Superior oDSGCs tends to fall below the fit line for Inferior oDSGCs, indicating lower intrinsic excitability. However, greater excitatory inputs to Superior oDSGCs outweigh the difference in intrinsic excitability, leading to more total spikes in Superior oDSGCs. Further, inhibition does not intuitively explain spike outputs since there is a positive correlation between inhibitory input and number of spikes across directions. This correlation is likely caused by an additional positive correlation between excitation and inhibition. Therefore, spikes are best explained by excitation. (**BB**) Preferred direction of inhibition vs. preferred direction of spikes recorded in the same cell. Dashed line represents the prediction for a 180° difference. (**CC**) Preferred direction of excitation vs. preferred direction of spikes recorded in the same cell. Dashed line represents prediction for 0° difference. (**DD**) Preferred direction of excitation vs. preferred direction of inhibition recorded in the same cell. Dashed line represents the prediction for 180° difference. Labels of T, D, N, and V correspond to temporal, dorsal, nasal, and ventral directions on the retina, respectively. *p<0.05, **p<0.01, ***p<0.001.

To test whether this difference in the magnitude of excitatory input to Superior and Inferior oDSGCs generalized across stimulus types, we measured the spike responses and postsynaptic currents of both cell types in response to a full-field light increment (**Figure 2.12**). As with the drifting bar, the light increment elicited more total spikes in Superior than in Inferior oDSGCs. We also observed significant correlations between the magnitude of a cell's increment response and both the area of its tuning curve (Sup: $R = 0.68$, $p=4.39 \times 10^{-17}$; Inf: $R = 0.68$, $p=1.24 \times 10^{-23}$) and its direction selectivity index (Sup: $R = -0.26$, $p=0.005$; Inf: $R = -0.38$, $p=7.10 \times 10^{-7}$). Under voltage-clamp conditions, the increment evoked greater EPSCs in Superior than Inferior oDSGCs. However, there was no difference in IPSC magnitude between cell types. Further, we found a strong correlation between the maximum firing rate of a cell to the increment and the magnitude of its peak EPSC, but not peak IPSC. These results demonstrate that Superior oDSGCs spike more than Inferior oDSGCs across multiple stimuli, and, further, that this difference in spiking is consistently associated with the amount of excitatory, but not inhibitory, input.

2.2.4 Postsynaptic differences may account for shifts in E/I

Differences in the postsynaptic currents of Superior and Inferior oDSGCs could result from asymmetries in presynaptic wiring and/or the postsynaptic properties of each oDSGC type. Serial block-face electron microscopy (Briggman et al., 2011; Mani et al., 2021; Matsumoto et al., 2019) and analysis of dendritic stratification (Yonehara et al., 2009) have not yet provided evidence of presynaptic wiring differences between oDSGCs with different preferred directions. Thus, we investigated possible postsynaptic asymmetries.

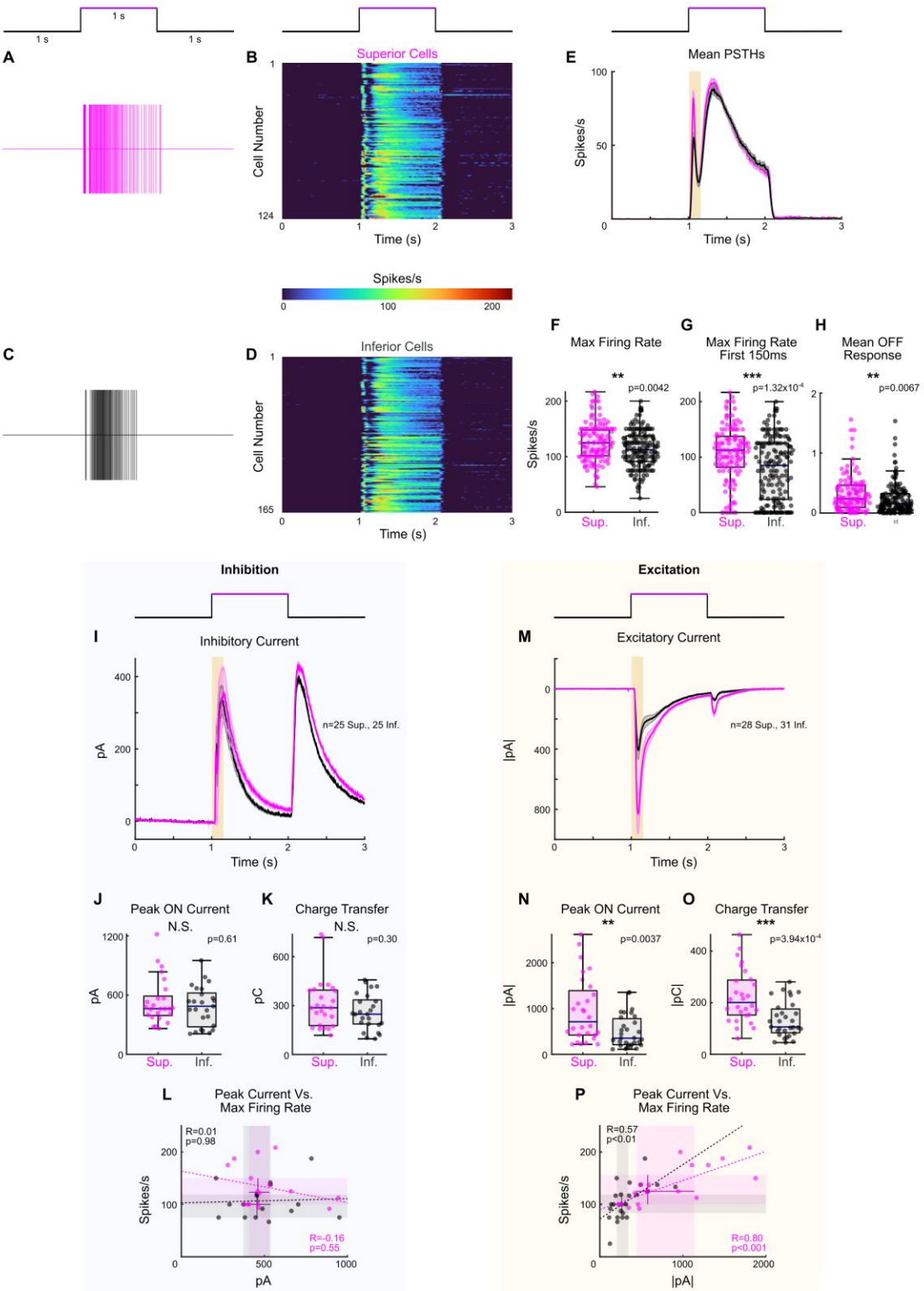

Figure 2.12 Full-field light increments elicit more spikes and excitation in Superior ON direction-selective retinal ganglion cells (oDSGCs).

(Figure caption continued on the next page)

(Figure caption continued from the previous page)

(**A, C**) Example extracellular spike rasters from (**A**) a Superior and (**C**) an Inferior oDSGC in response to a 1 s light increment (405 nm). The schematic above shows the timing of the increment relative to the data. (**B, D**) Peristimulus time histograms (PSTHs) of average cell-attached light increment responses for each of (**B**) n = 124 Superior and (**D**) n = 165 Inferior oDSGCs. (**E**) Average PSTH across all cells shown in (**B**) and (**D**) (mean ± SEM). Highlighted region shows the first 150 ms after stimulus onset. (**F**) Distributions of each cell's maximum firing rate throughout the entirety of the light increment. (**G**) Maximum firing rates during the first 150 ms after stimulus onset (i.e., highlighted region in [**E**]). (**H**) Mean firing rates ≥50 ms after stimulus offset. (**I**) Average inhibitory current in response to the 1 s light increment for Superior (magenta) and Inferior (gray) oDSGCs (mean ± SEM; voltage-clamp at +10 mV). (**J**) Peak inhibitory currents for the duration of the 1 s increment. (**K**) Total inhibitory charge transfers for the duration of the 3 s stimulus (i.e., including baseline and OFF response). (**L**) Peak inhibitory currents (as in [**J**]) versus maximum firing rate (as in [**F**]) for cells in which both metrics were recorded. (**M**) Average excitatory current in response to the 1 s light increment for Superior (magenta) and Inferior (gray) oDSGCs (mean ± SEM; voltage-clamp at –60 mV). (**N**) Peak excitatory currents for the duration of the 1 s increment. (**O**) Total excitatory charge transfers for the duration of the 3 s stimulus (i.e., including baseline and OFF response). (**P**) Peak excitatory current (as in [**N**]) versus maximum firing rate (as in [**F**]) for cells in which both metrics were recorded. The magenta line falls below the black line, indicating that Superior oDSGCs have a lower ratio of spike output to excitatory input. For scatter plots, large points and whiskers represent univariate medians and 95% confidence intervals (via bootstrapping). Dashed lines are least-squares linear regressions for Superior (magenta) and Inferior (gray) oDSGCs. R and p values are the Spearman's rank correlation coefficient and associated two-sided significance, respectively. For box plots, the horizontal line represents median, box boundaries are IQR, and whiskers represent the most extreme observation within 1.5× IQR. *p<0.05, **p<0.01, ***P<0.001.

We analyzed the morphology of Superior and Inferior oDSGCs by filling cells of both types with intracellular dye (**Figure 2.13A**). Convex hull analysis revealed that the dendritic fields of Superior oDSGCs covered a larger area than those of Inferior oDSGCs (**Figure 2.13B**). Sholl analysis, however, showed similar dendritic complexities (**Figure 2.13C**). To identify synaptic differences between cell types, we stained for the excitatory postsynaptic density scaffolding protein PSD-95 (Koulen et al., 1998; **Figure 2.13D–F**) and the inhibitory postsynaptic scaffolding protein gephyrin (Sassoè-Pognetto et al., 1995; Sassoè-Pognetto and Wässle, 1997; **Figure 2.13G–I**). These assays revealed no difference in the number of synaptic puncta between cell types. However, Superior oDSGCs had significantly larger excitatory, but not inhibitory, puncta (**Figure 2.13F, I**). This anatomy is consistent with greater amounts of excitatory synaptic input to Superior oDSGCs.

To complement these morphological observations, electrophysiological recordings revealed a number of intrinsic differences between Superior and Inferior oDSGCs. First, the membrane capacitances of Superior oDSGCs were greater than those of Inferior oDSGCs (**Figure 2.14A**). Sequentially recording both the spike output and EPSCs of individual oDSGCs to the full-field increment stimulus also revealed that Superior oDSGCs had lower spike-to-EPSC ratios (**Figure 2.12P**). This observation persisted for each direction of the drifting bar stimulus (**Figure 2.11D-AA**). In agreement, the input resistances of Superior oDSGCs were lower than those of Inferior oDSGCs (**Figure 2.14B**). These phenomena are consistent with the larger size of Superior oDSGCs relative to Inferior oDSGCs (**Figure 2.13B**). We found no significant differences in other intrinsic properties including the resting membrane potential and spike threshold

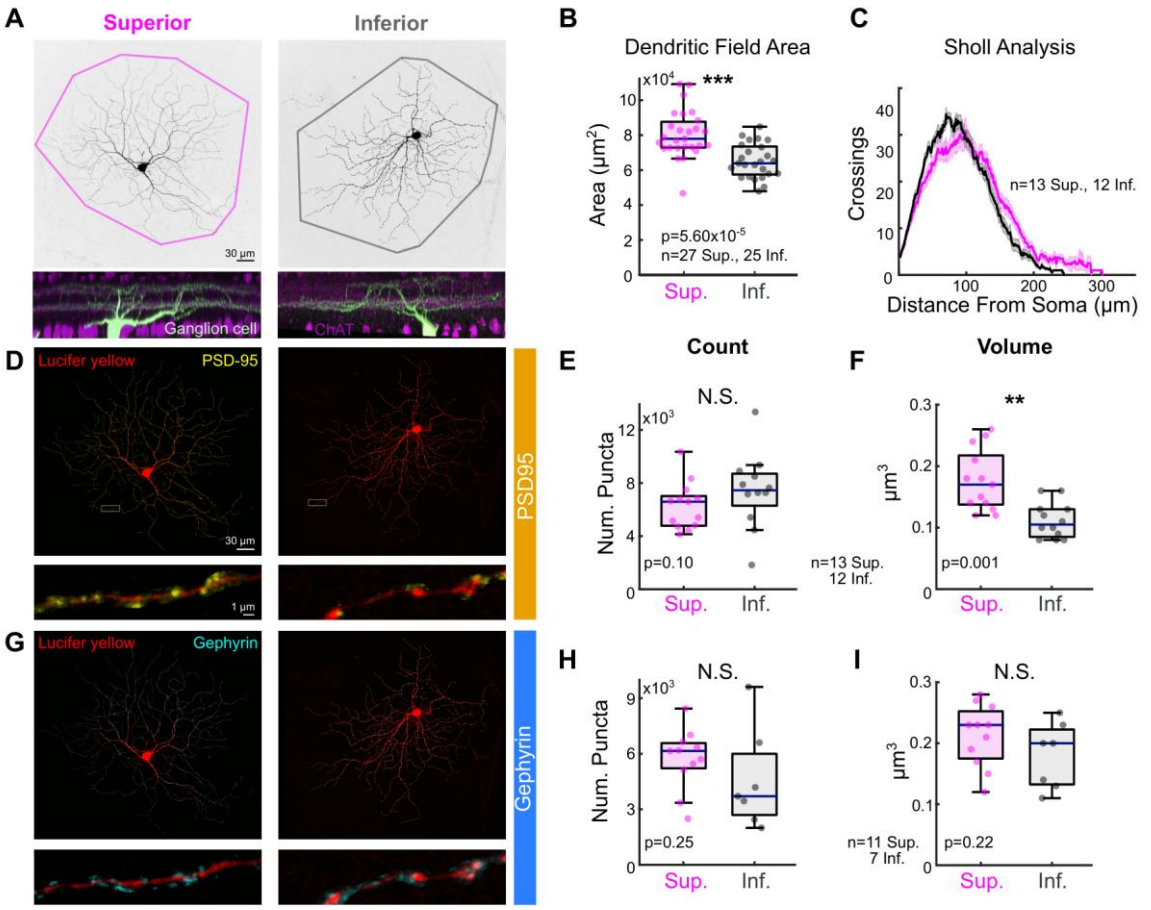

Figure 2.13 Superior ON direction-selective retinal ganglion cells (oDSGCs) have larger dendritic fields and excitatory postsynaptic sites.

(**A**) Confocal images of exemplar Superior (left) and Inferior (right) oDSGCs filled with dye. Convex polygons are drawn around the tips of their dendrites. (Bottom) Side views of different Superior and Inferior oDSGCs filled and stained for acetylcholinesterase (ChAT) bands. Both cell types have dendrites that stratify in the ON and OFF ChAT bands, with the majority of dendrites in the ON sublamina. (**B**) Convex polygon areas across all filled cells. (**C**) Sholl analysis indicating the number of dendritic crossings as a function of radial distance from the soma (mean ± SEM). (**D, G**) Ganglion cells with immunostaining for (**D**) excitatory postsynaptic scaffolding protein PSD-95 or (**G**) inhibitory postsynaptic scaffolding protein gephyrin. (Bottom) Magnification of a stretch of dendrites with labeled puncta. (**E, H**) Total number of puncta within each ganglion cell for (**E**) PSD-95 and (**H**) gephyrin. (**F, I**) Quantification of average puncta volume for (**F**) PSD-95 and (**I**) gephyrin. For box plots, horizontal line represents median, box boundaries are IQR, and whiskers represent the most extreme observation within 1.5× IQR. *p<0.05, **p<0.01, ***p<0.001.

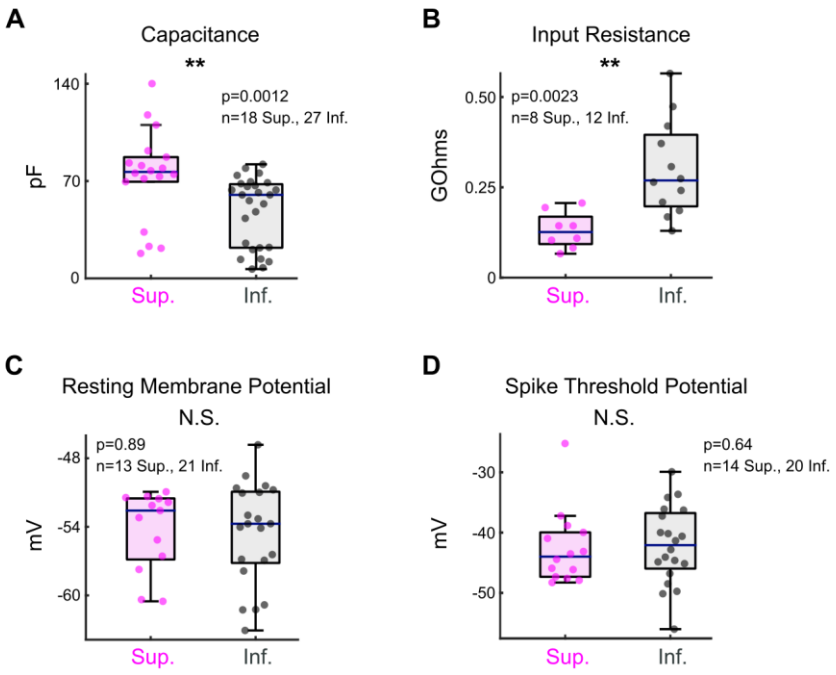

Figure 2.14 Intrinsic electrophysiological properties of ON direction-selective retinal ganglion cells (oDSGCs).
(**A**) Membrane capacitance, (**B**) input resistance, (**C**) resting membrane potential, and (**D**) spike threshold potential were measured from Superior (magenta) and Inferior (gray) oDSGCs during whole-cell patch-clamp recordings. Consistent with their larger morphological size (Figure 2.13B), Superior oDSGCs had larger capacitances and lower input resistances than Inferior oDSGCs. There was no significant difference in either resting membrane potential or spike threshold potential across cell types. For all panels, the blue line represents median, box boundaries are IQR, and whiskers represent the most extreme observation within 1.5× IQR. *p<0.05, **p<0.01, ***p<0.001.

(**Figure 2.14 C and D**). Together, these data indicate that Superior oDSGCs are less intrinsically excitable than Inferior oDSGCs, but that this asymmetry is outweighed by counteracting discrepancies in the magnitude of excitatory synaptic input to each cell type.

2.2.5 Untuned excitation broadens spike tuning curves

That Superior oDSGCs receive relatively more excitation than Inferior oDSGCs explains their greater spike output (**Figure 2.4F-H, 2.7A, 2.12A-H**). Less obvious, however, is whether this difference in excitatory input can also account for the observation that Superior oDSGCs have wider tuning curves (**Figure 2.4I–K**, **2.6, 2.7B-C**). A debate remains over whether excitatory inputs to DSGCs are directionally tuned (Vaney et al., 2012; Matsumoto et al., 2019; Matsumoto et al., 2021; Percival et al., 2019; Poleg-Polsky and Diamond, 2011; Summers and Feller, 2022; Yonehara et al., 2013; reviewed by Wei, 2018). While our results indicate that MTN-projecting RGCs might receive different amounts of excitation based on stimulus direction (Figure 3H), the majority of directionally tuned inputs were inhibitory (**Figure 2.10K**). Further, the apparent direction selectivity of EPSCs is likely partially attributable to imprecise space clamp (Vaney et al., 2012; Poleg-Polsky and Diamond, 2011; but see Percival et al., 2019). Thus, the extent to which the tuning curves of Superior and Inferior oDSGCs are shaped by direction-selective excitation is unclear, and we remain agnostic on this point. Instead, we focus on the more pronounced observation that Superior oDSGCs receive more excitatory input than Inferior oDSGCs across stimulus directions (**Figure 2.10G and I, 2.11**), regardless of the extent to which this excitation is tuned. In the following experiments, we investigate the relationship between spike tuning curve shape and the overall amount of excitation to an

oDSGC. We ask whether and how different magnitudes of excitatory input to Superior and Inferior oDSGCs can explain their difference in tuning curve width.

To test how the magnitude of excitation, even when directionally untuned, to an oDSGC changes the shape of its tuning curve, we measured the spikes of Superior and Inferior oDSGCs in the current-clamp configuration (**Figure 2.15A–B and F**) while injecting constant amounts of either positive (to add ~6 mV, 'depolarizing') or negative (to subtract ~6 mV, 'hyperpolarizing') current across stimulus directions. Importantly, the depolarizing current injections were small enough such that every cell retained a baseline firing rate of 0 Hz. This approach allowed us to investigate how providing a cell with more or less directionally untuned excitation influences the shape of its spike tuning curve, as quantified by the direction selectivity index (as in **Figure 2.4K**, a metric that decreases with greater tuning curve width) and the area of the normalized tuning curve (as in **Figure 2.4J**, referred to as 'normalized area,' a metric that increases with tuning curve width). We found that tuning curves measured under depolarizing conditions were not only larger (**Figure 2.15C–D and G**), but also wider, with lower direction selectivity indices (**Figure 2.15H**) and larger normalized areas (**Figure 2.16F**) than those measured under hyperpolarizing conditions. These findings are not attributable to the effects of current injection on intrinsic properties of oDSGCs (**Figure 2.17**). Thus, these experiments demonstrate that increasing the amount of untuned excitation to an oDSGC broadens its tuning curve.

Comparing these results to those recorded extracellularly in cell-attached recordings revealed an additional nuance: depolarizing current injections widened only the tuning curves of Inferior oDSGCs, while hyperpolarizing injections sharpened the

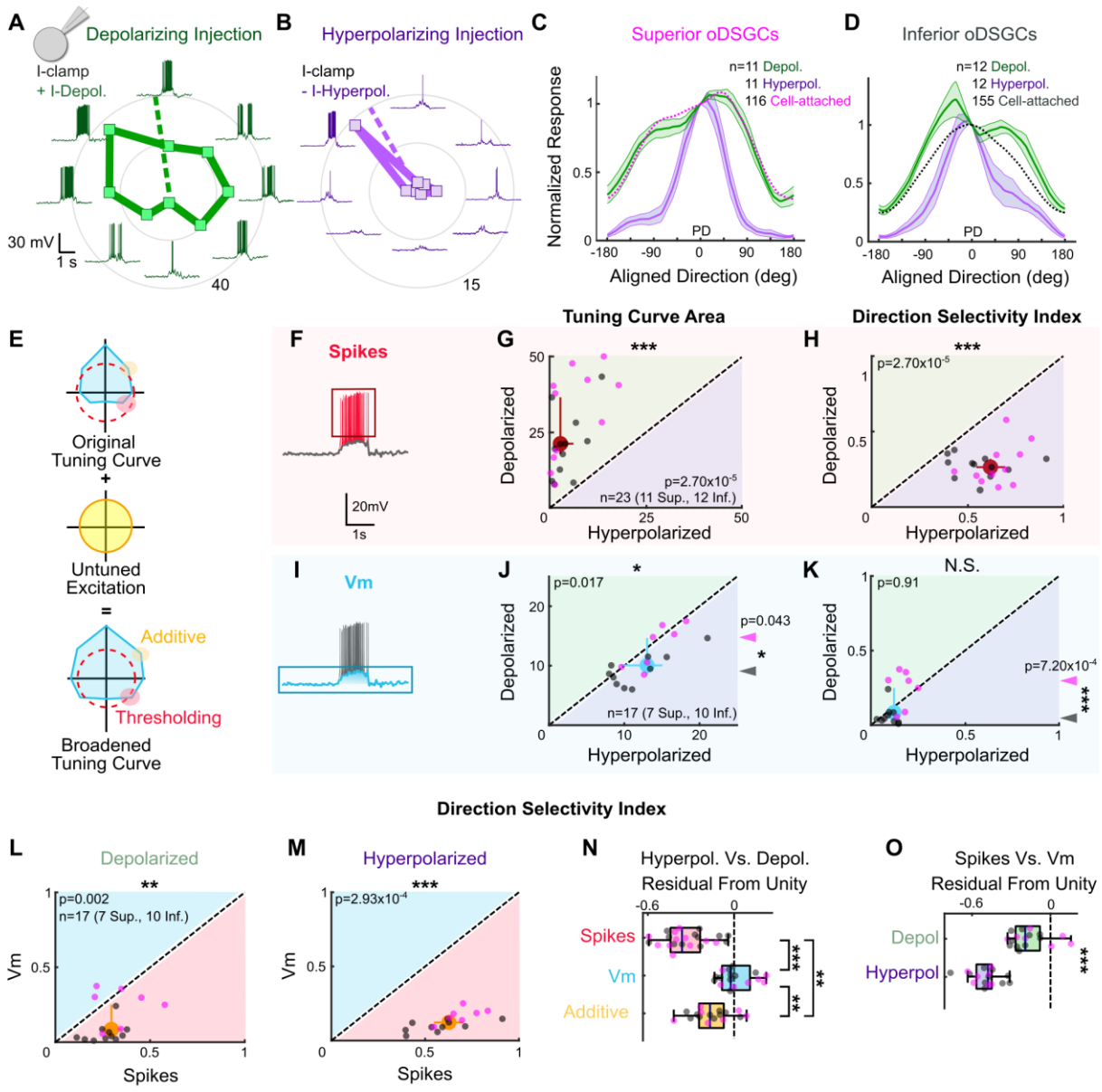

Figure 2.15 Thresholding differentiates the tuning properties of Superior and Inferior ON direction-selective retinal ganglion cells (oDSGCs).

(Figure caption continued on the next page)

(Figure caption continued from the previous page)

(**A, B**) Exemplar Inferior oDSGC in whole-cell current-clamp during (**A**) depolarizing and (**B**) hyperpolarizing current injection in response to a bar moving in eight directions. Numbers on concentric circles indicate spike counts. Dashed lines represent preferred directions. Coordinates are in retinal space. (**C, D**) Mean (± SEM) normalized tuning curves (aligned and normalized to the response of each cell in its preferred direction) for (**C**) Superior and (**D**) Inferior oDSGCs under conditions of depolarizing (green) and hyperpolarizing (purple) current injection. Dotted lines indicate the average normalized spike tuning curves of each population from cell-attached recordings (as in **Figure 2.4I**). (**E**) Illustration of the influence of untuned excitation on the tuning curve through additive (yellow) and thresholding (red) effects. The blue area indicates the membrane potential, and the dashed red line indicates the spike threshold. (**F, I**) Example whole-cell current-clamp recording in which (**F**) spikes and (**I**) subthreshold voltages (Vm) have been separated. (**G**) Linear tuning curve area and (**H**) direction selectivity index of the spike tuning curve during hyperpolarizing (abscissa) and depolarizing (ordinate) current injections. (**J**) Linear tuning curve area and (**K**) direction selectivity index of peak subthreshold membrane potential tuning curves. For (**G–H, J–K**), regions of green (or purple) indicate that the metric is greater during depolarizing (or hyperpolarizing) injections. Points that fall on the line indicate equivalent metrics under the two conditions. Individual cells are shown as dots (Superior in magenta, Inferior in gray). Large red and blue dots represent univariate medians (collapsed across cell type) and whiskers indicate 95% confidence intervals determined via bootstrapping. Significance values indicate whether the data tend to fall unevenly on one side of the unity line (two-sided signed-rank). Arrowheads in (**J, K**) represent the median of Superior (magenta) and Inferior (gray) oDSGCs along the unity line, and associated significance values indicate comparison between Superior and Inferior oDSGCs (two-sided rank-sum). (**L, M**) Direction selectivity index for spikes (abscissa) and simultaneously measured subthreshold voltages (ordinate) under (**L**) depolarizing and (**M**) hyperpolarizing conditions. Significance values indicate whether the data tend to fall unevenly on one side of the unity line (two-sided signed-rank). (**N**) Residuals from the unity line for individual cells from the plots in (**H**) and (**K**). Dashed line indicates unity (i.e., no difference across depolarizing and hyperpolarizing conditions). Pairwise comparisons are shown between spikes, Vm, and Vm with additive offset. (**O**) Residuals from the unity line for individual cells from the plots in (**L**) and (**M**). Dashed line indicates unity (i.e., no difference between spikes and subthreshold voltages). Comparisons are made between the depolarizing and hyperpolarizing conditions (two-sided rank-sum). For box plots, the blue line represents median, box boundaries are IQR, and whiskers represent the most extreme observation within 1.5× IQR. *p<0.05, **p<0.01, ***p<0.001.

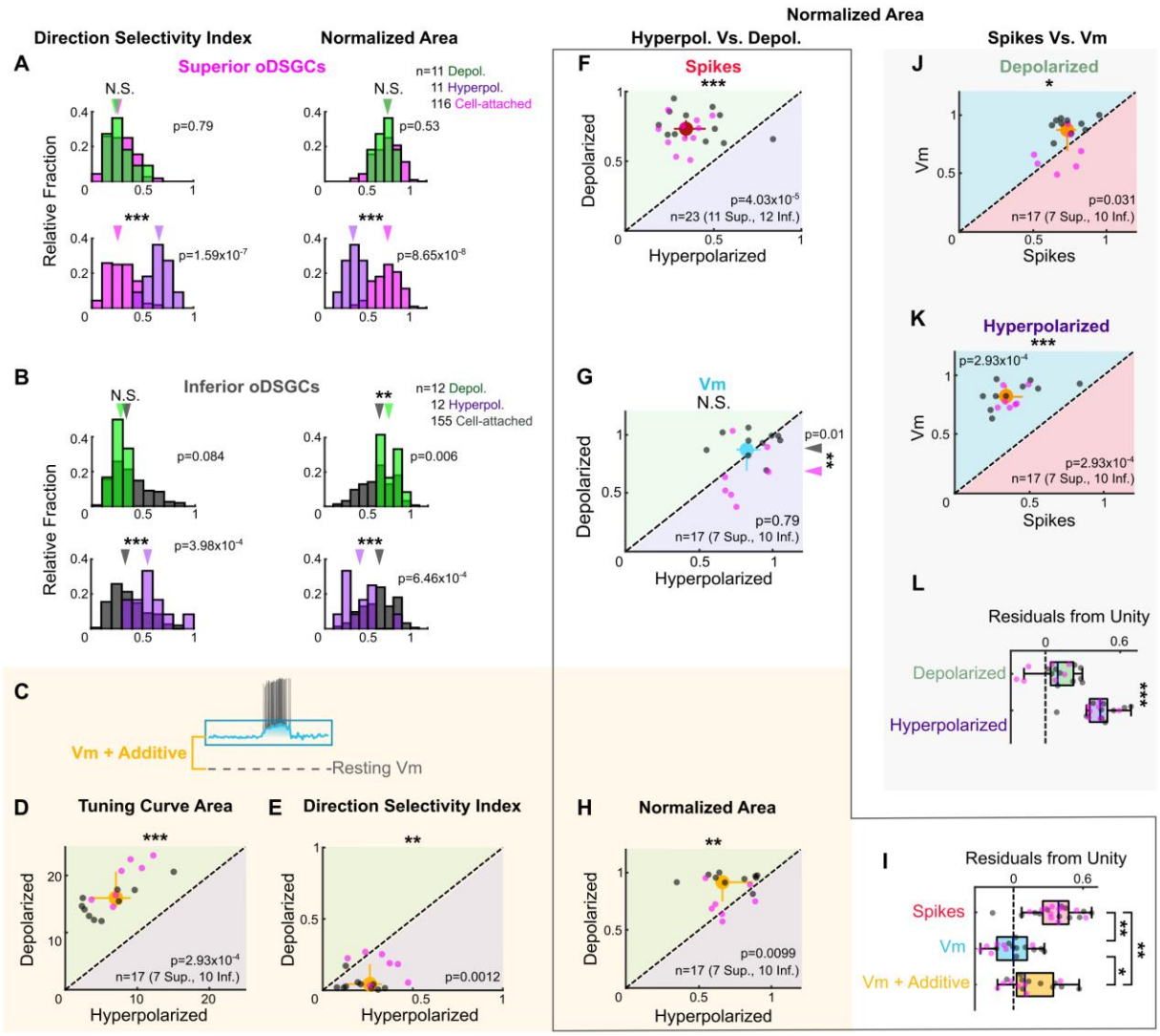

Figure 2.16 Spike and subthreshold voltage tuning curves with directionally untuned current injections.

(Figure caption continued on the next page)

(Figure caption continued from the previous page)

(**A, B**) Comparison of spike tuning curve metrics from cell-attached and current injection recordings. Histograms show the direction selectivity index (left) and area of the normalized tuning curve (right) for cell attached (magenta in [**A**] or gray in [**B**]), hyperpolarizing (green, top), and depolarizing (purple, bottom) conditions for (**A**) Superior and (**B**) Inferior ON direction-selective retinal ganglion cells (oDSGCs). Arrows indicate medians. (**C**) Illustration of the voltage offset added via current injection during the depolarizing condition. The same offset was subtracted for the hyperpolarizing condition. Diagram is not shown to scale. (**D, E, H**) Metrics of the subthreshold membrane potential tuning curve during hyperpolarizing (abscissa) and depolarizing (ordinate) current injections with the additive offset taken into account: (**D**) linear tuning curve area, (**E**) direction selectivity index, and (**H**) area of the normalized tuning curve. Additive effects cause larger and broader membrane potential tuning curves following increases in the amount of untuned excitation. (**F–H**) Area of the normalized tuning curve during hyperpolarizing (abscissa) and depolarizing (ordinate) current injections for (**F**) spikes, (**G**) subthreshold voltages, and (**H**) subthreshold voltages with the additive offset taken into account. All metrics were measured simultaneously. (**I**) Residuals from the unity line for individual cells from the plots in (**F–H**). Dashed line indicates unity (i.e., no difference across depolarizing and hyperpolarizing conditions). Pairwise comparisons are shown between spikes, Vm, and Vm with additive offset. Current injections influence spike tuning curves more than either version of the Vm tuning curve. (**J, K**) Area of the normalized tuning curve for spikes (abscissa) and simultaneously measured subthreshold voltages (ordinate) under (**J**) depolarizing and (**K**) hyperpolarizing conditions. (**L**) Residuals from the unity line for individual cells from the plots in (**J, K**). Dashed line indicates unity (i.e., no difference between spikes and subthreshold voltages). Comparisons are made between depolarizing and hyperpolarizing conditions (two-sided rank-sum). For all scatter plots, individual cells are shown as small dots (Superior in magenta, Inferior in gray). Colored regions indicate that the metric is greater for that condition (**D–H**) or for spikes or Vm (**J, K**). Points on the line indicate equivalent values under the two conditions. Large dots represent univariate medians collapsed across cell types and whiskers are 95% confidence intervals determined via bootstrapping. Significance values indicate whether the data tend to fall unevenly on one side of the unity line (two-sided signed-rank). For all box plots, the blue line represents median, box boundaries are IQR, and whiskers represent the most extreme observation within 1.5× IQR. *p<0.05, **p<0.01, ***p<0.001.

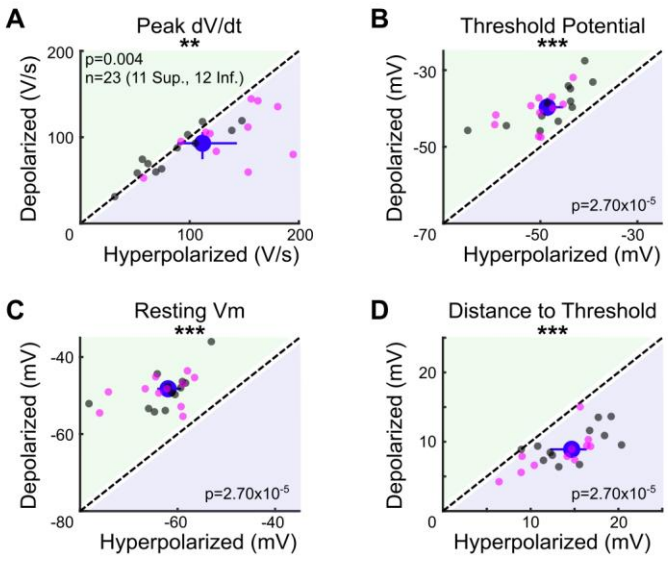

Figure 2.17 Effects of current injection on intrinsic properties of ON direction-selective retinal ganglion cells (oDSGCs).

(Figure caption continued on the next page)

(Figure caption continued from the previous page)

To measure the effects of depolarizing and hyperpolarizing current injections on the intrinsic properties of oDSGCs, the (**A**) peak rate of voltage change and (**B**) spike threshold potential were calculated for every cell under both conditions. Peak dV/dt was on average 10.9 V/s greater under hyperpolarizing relative to depolarizing conditions. The spike threshold potential was on average 9.0 mV more negative under hyperpolarizing conditions. Both of these observations are consistent with an increase in voltage-gated sodium channel availability in the hyperpolarizing condition. This intrinsic change increases the probability of spikes during hyperpolarizing relative to the depolarizing injections, and therefore cannot explain our experimental results of greater spikes and broader tuning curves under depolarizing conditions (Figure 5). The likely reason why our empirical data show increased spiking and broader tuning curves during depolarizing injections is that the relative distance between cells' resting membrane potentials and spike thresholds was greater in the hyperpolarizing condition. (**C**) The resting membrane potential was, on average, 12.6 mV more negative during hyperpolarizing injections than during depolarizing injections, whereas the spike threshold only changed by 9.0 mV (**B**). Thus, the difference between resting membrane potential and spike threshold was greater under hyperpolarizing conditions. (**D**) On average, cells' resting membrane potentials were 5.1 mV further away from the spike threshold potential under hyperpolarizing relative to depolarizing conditions. Current injections may also influence conductances of other voltage-gated ion channels, including calcium channels, though evidence that oDSGCs express such channels is limited and these effects are difficult to quantify. For all panels, regions of green (or purple) indicate that the metric is greater for depolarizing (or hyperpolarizing) current injections. Points on the line indicate equivalent values under the two conditions. Individual cells are shown as dots (Superior in magenta, Inferior in gray). Large blue dots represent univariate medians collapsed across cell types and whiskers indicate 95% confidence intervals determined via bootstrapping. Significance values indicate whether the data tend to fall unevenly on one side of the unity line (two-sided signed-rank). *$p<0.05$, **$p<0.01$, ***$p<0.001$.

tuning curves of both cell types (**Figure 2.15C and D, 2.16A and B**). One possibility is that while excitation generally broadens tuning curve width, greater excitatory input minimally affects Superior oDSGCs because these cells are already positioned closer to an upper limit on this phenomenon. Nonetheless, our results highlight a causal relationship between tuning curve width and the amount of untuned excitation that an oDSGC receives.

2.2.6 Spike threshold plays a dominant role in setting tuning curve width

Two complementary mechanisms could explain how untuned excitation widens tuning curves (**Figure 2.15E**). In the first mechanism, excitation influences the nonlinear transformation between synaptic input and spike output that is introduced by a neuron's spike threshold. More specifically, thresholding may sharpen a neuron's spike tuning curve relative to the tuning of underlying membrane fluctuations by clamping spike output at zero in response to subthreshold membrane responses that are likely to occur for null direction stimuli (Oesch et al., 2005). When the amount of untuned excitatory input increases, however, membrane fluctuations more readily surpass the spike threshold for all stimulus directions, thereby broadening the spike tuning curve. In the second mechanism, untuned excitation directly circularizes the tuning curve of underlying membrane potentials by increasing null direction responses proportionally more than preferred direction responses. This 'additive' contribution would then be inherited by the spike tuning curve (Poleg-Polsky and Diamond, 2016a).

We first tested whether thresholding contributes to the width of oDSGC tuning curves. To do so, we isolated the underlying subthreshold voltages (Vm) from our current-clamp recordings that also contained spikes (**Figure 2.15I**). Three independent

observations about these Vm tuning curves each suggests that thresholding critically influences spike tuning curve shape. First, unlike for spikes, depolarizing and hyperpolarizing current injections did not affect the direction selectivity (**Figure 2.15K and N**) or normalized area (**Figure 2.16 G and I**) of Vm tuning curves. The total areas of Vm tuning curves were, however, slightly larger under the hyperpolarizing condition, likely due to the marginally greater driving force on excitatory conductances in this setting (**Figure 2.15J**). Second, the Vm tuning curves of Superior oDSGCs were larger in magnitude than those of Inferior oDSGCs (**Figure 2.15J arrowheads**), but also more sharply tuned, with greater direction selectivity indices (**Figure 2.15K arrowheads**) and smaller normalized areas (**Figure 2.16G arrowheads**). This latter result was anticipated from our voltage-clamp recordings that indicated that inhibition is more direction-selective in Superior oDSGCs (**Figure 2.10D**). It also suggests, however, that the shape of the spike tuning curve is not directly inherited from that of the underlying membrane potential and instead reflects the interplay between Vm magnitude and spike threshold. Third, spike tuning curves were more direction-selective (**Figure 2.15L and M**) and had smaller normalized areas (**Figure 2.16J and K**) than those of simultaneously measured Vms for both depolarizing and hyperpolarizing injections. The difference between the shape of the spike and Vm tuning curves was smaller for the depolarizing condition, however, because in this setting the majority of stimulus directions elicited Vm responses that surpassed the spike threshold (**Figure 2.15O, Figure 2.16L**). Together, these three results corroborate the notion that thresholding prominently influences the width of the spike tuning curve relative to the amount of untuned excitation that an oDSGC receives.

To test the extent to which excitation broadens oDSGC tuning curves through additive effects, we recomputed Vm tuning curves after including a constant, additive offset that reflected the average current injection supplied during depolarizing and hyperpolarizing injections. These offset-corrected Vm tuning curves were significantly wider under depolarizing conditions than they were under hyperpolarizing conditions (**Figure 2.16E and H**). However, the observation that (uncorrected) Vm tuning curves — in which putative additive differences between cell types are expected to persist — were more sharply tuned for Superior than Inferior oDSGCs (**Figure 2.15K**, **2.16G arrowheads**) indicates that thresholding has a greater influence on spike tuning curves than does additive excitation. In agreement, current injections caused significantly larger changes in spike tuning curves than in offset-corrected Vm tuning curves (**Figure 2.15N, 2.16I**). These results demonstrate that while untuned excitation likely has some additive effect, complementary thresholding has greater influence over oDSGC spike tuning curves.

2.2.7 A parallel conductance model recapitulates the influence of thresholding on oDSGC direction tuning

Together, our current injection experiments suggest that (1) spike thresholding plays a prominent role in setting the width of oDSGC tuning curves, and (2) additive effects contribute minorly. To independently test these findings, we built a parallel conductance model of an oDSGC based on empirically measured parameters from a separate set of cells to those used for the current injection experiments. Among these parameters were eight inhibitory conductances (one for each stimulus direction), and a single, directionally untuned excitatory conductance (**Figure 2.18A and B**). We then

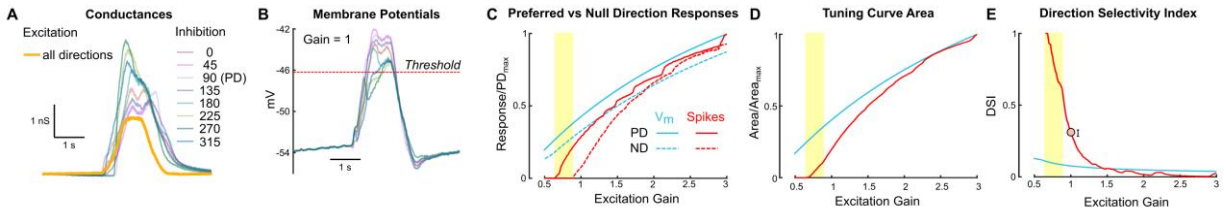

Figure 2.18 A parallel conductance model demonstrates how untuned excitation contributes to direction tuning.

An exemplar ON direction-selective retinal ganglion cell (oDSGC) was modeled using parameters recorded directly from oDSGCs, including directionally tuned inhibitory conductances for each of eight drifting bar directions, and a single, untuned excitatory conductance (see 'Materials and methods'). (**A**) Inhibitory (pastel colors) and excitatory (yellow) conductances of the model oDSGC in response to bars moving in eight directions. (**B**) The parallel conductance model uses the empirically measured parameters to model the membrane potential across bar directions, shown here for the case in which the excitatory gain (i.e., a multiplication factor applied to the excitatory conductance) is set to 1.0. The red dotted line indicates the spike threshold. (**C**) Preferred (solid lines) and null (dotted lines) direction responses of peak subthreshold voltages (blue) and spikes (red) across a range of excitatory gains. Values are normalized to the maximum preferred direction response for each metric. The yellow column indicates the regime in which a null direction stimulus evokes zero spikes but a preferred direction stimulus evokes increasingly more spikes, an example of nonlinear behavior caused by the spike threshold. (**D, E**) Directional tuning properties as a function of excitatory gain for subthreshold voltages (blue) and spikes (red): (**D**) area of the linear tuning curve (normalized to the maximum area for each metric), and (**E**) direction selectivity index. Orange dot (and error bars) in (**E**) correspond to the empirically measured median (and 95% confidence interval determined via bootstrapping) direction selectivity index from cell-attached recordings, collapsed across cell types.

tested how manipulating the gain of the excitatory conductance affected tuning curves generated from either spikes or the peak subthreshold membrane potentials (**Figure 2.18C–E, 2.19**).

Increasing the gain of untuned excitation to the model oDSGC increased the total area of both spike and Vm tuning curves (**Figure 2.18D**). However, while the spike tuning curve rapidly widened and became less direction-selective with increasing excitatory gain, the width of the Vm tuning curve was much less dependent on excitatory gain (**Figure 2.18E, 2.19**). The stark difference between the spike and Vm trajectories can only be attributed to thresholding effects. On the other hand, the shallow slope of the Vm curve in **Figure 2.18E** reflects the additive contribution of excitation. Consistent with our physiological results, thresholding played a critical role in setting the model oDSGC's tuning curve width, whereas additive effects were relatively minor. Further, the prior observation that depolarizing current injections influenced Superior oDSGCs less than Inferior oDSGCs (**Figure 2.15C and D, Figure 2.16A and B**) is supported by the diminishing marginal effect of additional excitatory gain on spike tuning curve width. We also noticed that the average empirically measured direction selectivity index (**Figure 2.18E circle**) and normalized tuning curve area (**Figure 2.19**) fell within the regime where these metrics steeply depended on excitatory gain. In this regime, thresholding effects render small changes in synaptic inputs particularly influential for oDSGC direction tuning.

2.2.8 Thresholding effects produce contrast-sensitive direction tuning in oDSGCs

The dependence of oDSGC tuning on thresholding predicts that any stimulus that influences the magnitude of synaptic inputs may also alter tuning curve shape. We tested this hypothesis by comparing the tuning curves of Superior and Inferior oDSGCs in

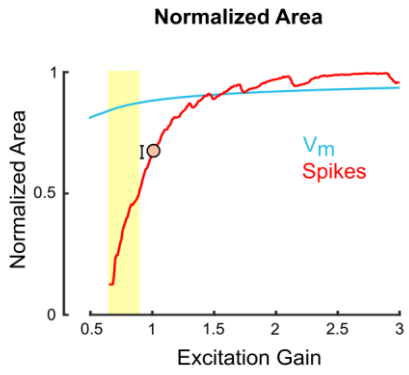

Figure 2.19 The normalized area of model spike tuning curves, but not subthreshold membrane potential tuning curves, is steeply influenced by excitation gain.

Area of the normalized tuning curve for spikes (red) and underlying subthreshold membrane potentials (blue) as a function of the gain of an untuned excitatory input to a model ON direction-selective retinal ganglion cell (oDSGC). Greater values along the vertical axis indicate a broader tuning curve. Additive excitation contributes to the slow rise of the membrane potential line, whereas thresholding effects cause the steep change in spike tuning curve width. The orange dot and error bars correspond to the empirically measured median and 95% confidence intervals (via bootstrapping), respectively, for this metric collapsed across cell types from cell-attached recordings.

response to high-contrast (stimuli used in previous figures unless specified otherwise) and fivefold lower contrast (i.e., 20% relative contrast) drifting bars. For most cells, the low-contrast bars elicited fewer spikes (**Figure 2.20A and B, Figure 2.22A**). However, as in the case of high-contrast stimuli, Superior oDSGCs tended to spike more and have wider tuning curves than Inferior oDSGCs in response to low-contrast bars (**Figure 2.4H, J, and K, insets**). Nonetheless, cells of both types had sharper spike tuning curves in response to low-contrast, compared to high-contrast, stimuli (**Figure 2.20C, 2.21A, 2.22B and C**). To test whether this contrast sensitivity could be attributed to thresholding, we measured the tuning curves of subthreshold membrane potentials. While the area of Vm tuning curves was greater under high-contrast conditions (**Figure 2.20D**), the direction selectivity (**Figure 2.20E**) and normalized area (**Figure 2.21B**) of Vm tuning curves did not change with stimulus contrast. In agreement, the fraction of cells with spike tuning curves that sharpened under low contrast was significantly different than the equivalent fraction of Vm tuning curves that followed the same trend (DSI: p=0.0046; normalized area: p=0.0019; two-sided Fisher's exact) (**Figure 2.20C and E, 2.21A and B**), and Vm tuning curves were less affected by stimulus contrast than the tuning curves of simultaneously measured spikes (**Figure 2.20F, 2.21C**). These results indicate that thresholding is critical to setting oDSGC spike tuning curve width across stimulus contrasts, just as it is across cell types.

The finding that oDSGCs are contrast-sensitive departs from previous work which has shown that direction tuning in ooDSGCs is contrast-invariant (Poleg-Polsky and Diamond, 2016b; Sethuramanujam et al., 2016; Sethuramanujam et al., 2017). Contrast invariance in ooDSGCs appears to rely on the stability of E/I across contrasts. For this

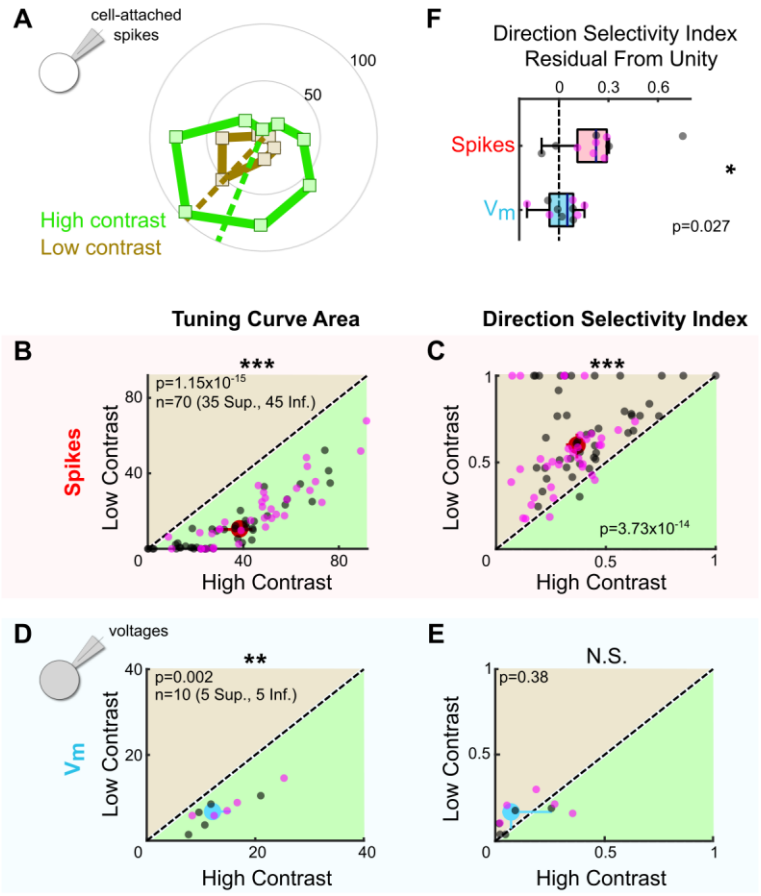

Figure 2.20 Stimulus contrast modulates the spike tuning curves of ON direction-selective retinal ganglion cells (oDSGCs).

(Figure caption continued on the next page)

(Figure caption continued from the previous page)

(**A**) Cell-attached tuning curves from an exemplar Superior oDSGC at high (green) and low (tan, 20% relative) contrasts. Numbers on concentric circles indicate spike counts. Dashed lines represent preferred directions. Coordinates are in retinal space. (**B**) Linear tuning curve area and (**C**) direction selectivity index from spike responses to high-contrast (abscissa) and low-contrast (ordinate) bars drifting in eight directions. Differences between Superior (magenta) and Inferior (gray) oDSGCs persist under low contrast (**see Figure 2.4**). (**D**) Linear tuning curve area and (**E**) direction selectivity index from peak subthreshold voltage responses to high-contrast (abscissa) and low-contrast (ordinate) bars drifting in eight directions. (**F**) Residuals from the unity line of the direction selectivity index under high- and low-contrast conditions for simultaneously measured spikes and subthreshold voltages. Comparison is made between spikes and subthreshold voltages. For all scatter plots, the region of green (or tan) indicates the metric is greater under high-contrast (or low-contrast) conditions. Points on the line indicate equivalent metrics under the two conditions. Individual cells are represented by small dots. Large dots represent univariate medians (collapsed across cell type). Whiskers indicate 95% confidence intervals determined via bootstrapping. Significance values indicate whether the data tend to fall unevenly on one side of the unity line (two-sided signed-rank). *$p<0.05$, **$p<0.01$, ***$p<0.001$.

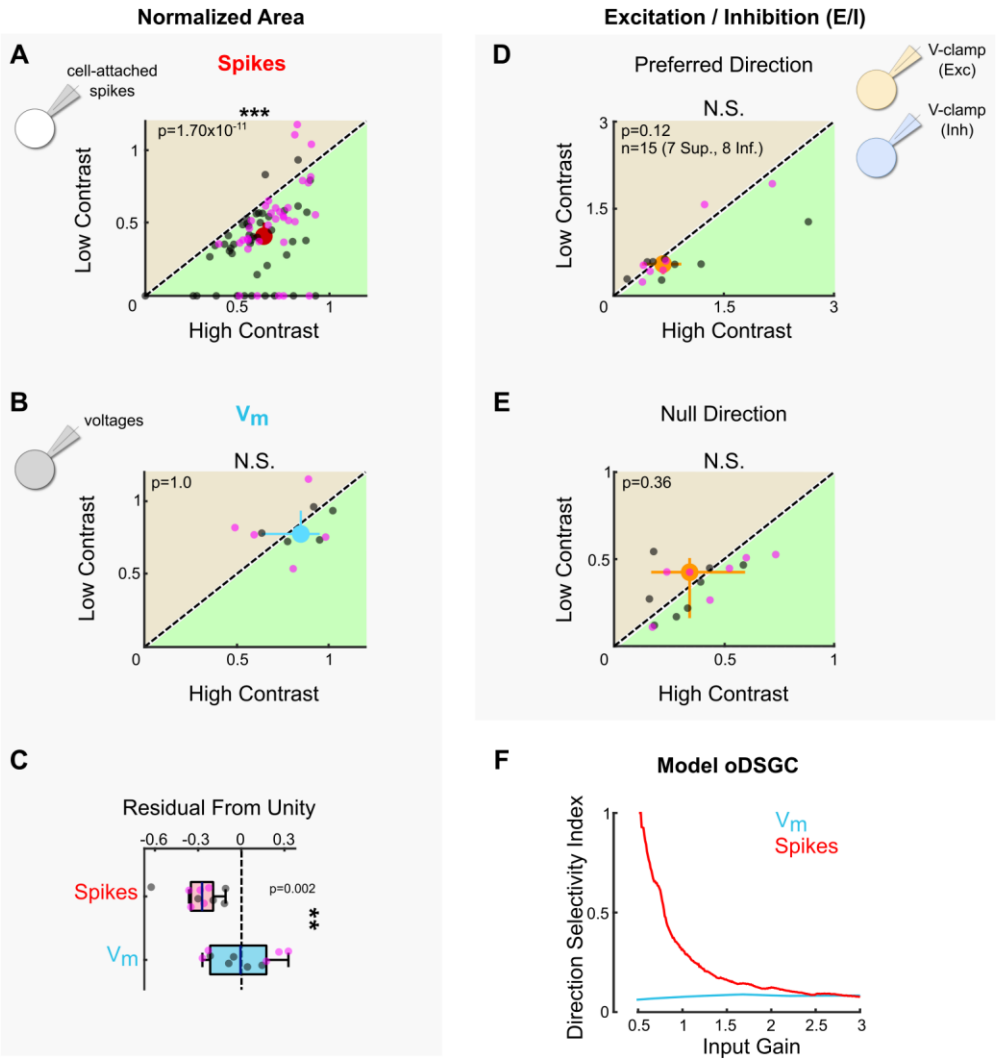

Figure 2.21 Stimulus contrast modulates spike tuning curve width but not the ratio of excitation to inhibition.

(Figure caption continued on the next page)

(Figure caption continued from the previous page)

(**A**) Area of the normalized tuning curve from spike responses to high-contrast (abscissa) and low-contrast (ordinate) bars drifting in eight directions. Differences between Superior (magenta) and Inferior (gray) ON direction-selective retinal ganglion cells (oDSGCs) persist under low contrast (see Figure 2). (**B**) Area of the normalized tuning curve from subthreshold voltages in response to high-contrast (abscissa) and low-contrast (ordinate) bars drifting in eight directions. (**C**) Residuals from the unity line for simultaneously measured spikes (as in [**A**]) and subthreshold voltages (as in [**B**]). The dashed line indicates unity (i.e., no difference between high and low contrast). Comparison is made between spikes and subthreshold voltages. (**D, E**) Excitation-to-inhibition (E/I) ratios for high- and low-contrast bars drifting in (**D**) the preferred and (**E**) the null direction of each cell. (**F**) Direction selectivity index generated from a parallel conductance model of an oDSGC under different scale factors applied jointly to excitatory and inhibitory inputs (constant E/I). For all scatter plots, the region of green (or tan) indicates the metric is greater under high-contrast (or low-contrast) conditions. Points on the line indicate equivalent metrics under the two conditions. Individual cells are represented by small dots. Large dots represent univariate medians (collapsed across cell type). Whiskers indicate 95% confidence intervals determined via bootstrapping. Significance values indicate whether the data tend to fall unevenly on one side of the unity line (two-sided signed-rank). All data acquired following epifluorescence targeting. *$p<0.05$, **$p<0.01$, ***$p<0.001$.

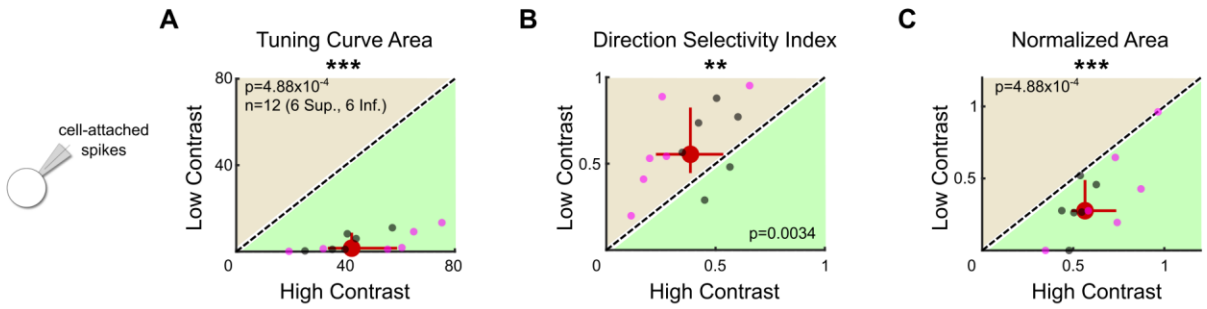

Figure 2.22 Two-photon targeting confirms that ON direction-selective retinal ganglion cells (oDSGCs) are contrast sensitive.

(**A**) Tuning curve area, (**B**) direction selectivity index, and (**C**) normalized area of the spike tuning curve were measured in the cell-attached configuration in response to high- and low-contrast drifting bars following two-photon targeting of oDSGCs. As occurred following epifluorescence targeting (**Figure 2.20, 2.21**), two-photon targeting revealed that the spike tuning curves of oDSGCs were smaller (**A**) and narrower (**B, C**) in response to low-contrast stimuli. For all plots, regions of green (or tan) indicate that the metric is greater for high-contrast (or low-contrast) stimuli. Points on the line indicate equivalent metrics under the two conditions. Individual cells are shown as small dots (Superior in magenta, Inferior in gray). Large red dots represent univariate medians collapsed across cell types. Whiskers indicate 95% confidence intervals determined via bootstrapping. Significance values indicate whether the data tend to fall unevenly on one side of the unity line (two-sided signed-rank). *p<0.05, **p<0.01, ***p<0.001.

reason, we tested whether the contrast sensitivity of oDSGCs was associated with a mutable E/I by sequentially measuring excitatory and inhibitory synaptic currents for preferred and null direction stimuli across contrasts. Our data show that E/I in neither the preferred nor null direction changed systematically with contrast (**Figure 2.21D and E**). Further, the fraction of cells with spike tuning curves that sharpened under low-contrast conditions was significantly greater than the fraction of E/I ratios that were lower under low-contrast conditions (DSI: PD p=0.0044, ND p=0.0044; normalized area: PD p=0.0132, ND p=0.0132; two-sided Fisher's exact) (**Figure 2.20C, 2.21A, D, and E**). These results suggest that as in ooDSGCs, E/I in oDSGCs is relatively stable across contrasts. However, the spike tuning curves of oDSGCs are nonetheless contrast-sensitive. Thus, stable E/I alone is insufficient to maintain the contrast invariance of spikes. In the case of oDSGCs, changes to the absolute magnitude of synaptic inputs across contrasts, along with thresholding effects, appear to trump the contrast invariance of E/I.

To further test the extent to which the magnitude of synaptic inputs can affect oDSGC tuning curves even with stable E/I, we revisited our parallel conductance model of an exemplary oDSGC. We modeled oDSGC responses while changing the gain of excitatory and inhibitory conductances together, thereby keeping E/I constant while nevertheless adjusting the total magnitude of E and I. As in our empirical data, lowering the gain of E and I together to simulate responses to low-contrast stimuli resulted in sharper spike tuning curves. The width of Vm tuning curves, however, remained relatively contrast invariant (**Figure 2.21F**). These results recapitulate our empirical findings and indicate that the spike threshold nonlinearity influences spike tuning curve width across

contrasts. Other stimulus parameters that affect the magnitude of excitation, inhibition, or both are also likely to modulate the direction tuning properties of oDSGCs.

2.2.9 A subtraction algorithm predicts vertical OKR from oDSGC activity

Having established the tuning properties of Superior and Inferior oDSGCs, we asked whether the asymmetries between these cell types, along with their contrast-sensitivities, could explain how vertical OKR changes across stimulus conditions. Cross-species work has established that Superior and Inferior oDSGCs are likely centrally integrated by a subtraction algorithm (Simpson, 1984; van der Togt et al., 1993; Soodak and Simpson, 1988). In this model, OKR is predicted on the basis of the difference in spike rate between Superior and Inferior oDSGCs rather than by the absolute spike rate of either cell type. A number of observations support this model: (1) stimuli that activate both Superior and Inferior oDSGCs (e.g., a full-field increment of light) do not elicit OKR, (2) stimuli that differentially activate Superior and Inferior oDSGCs (e.g., drifting gratings) maximally drive OKR (**Figures 2.1 and 2.4**), (3) Superior and Inferior oDSGCs project to separate MTN subnuclei (Yonehara et al., 2009; van der Togt et al., 1993) that are mutually connected by inhibitory interneurons (i.e., a simple differentiating circuit) (van der Togt et al., 1993; Giolli et al., 1985), (4) MTN neurons prefer either superior or inferior motion (Yonehara et al., 2009; van der Togt et al., 1993; Soodak and Simpson, 1988; Grasse and Cynader, 1982; Natal and Britto, 1988; Simpson et al., 1979), but their preferred and null directions are not 180° apart; instead, they correspond to the preferred directions of opposing oDSGC types (Soodak and Simpson, 1988; Natal and Britto, 1988; Simpson et al., 1979), which may differ by less than 180° (Oyster and Barlow, 1967; but see Sabbah et al., 2017), and (5) MTN neurons maintain moderate baseline spike

rates that are both augmented by preferred direction stimuli and diminished by null direction stimuli (Soodak and Simpson, 1988; Grasse and Cynader, 1982; Natal and Britto, 1988; Simpson et al., 1979). Together, along with the simplicity of the vertical OKR pathway and its isolation from other visual circuits, these lines of evidence all point to a circuit motif in which MTN neurons encode the difference in spike rate between Superior and Inferior oDSGCs. Thus, superior OKR likely occurs when Superior oDSGCs spike sufficiently more than Inferior oDSGCs, and vice versa. The robustness of OKR is putatively related to the magnitude of the spike rate difference (**Figure 2.23A**).

We used our empirically recorded electrophysiology data from Superior and Inferior oDSGCs to generate hypotheses for how OKR gain would change across

responses of Superior oDSGCs and the null direction responses of Inferior oDSGCs to high-contrast bars. Importantly, such inferences constitute linear predictions of gain. Allowing for the possibility that downstream circuitry incorporates additional monotonic nonlinearities, a linear prediction is consistent with behavior so long as it predicts gain changes in the correct direction (but not magnitude) across stimulus conditions.

The asymmetries in the tuning curves of Superior and Inferior oDSGCs resulted in the following key predictions for how OKR gain would change across stimulus directions and contrasts: (1) gain would decrease with stimulus contrast, (2) OKR would be asymmetric, with superior stimuli eliciting greater gain than inferior stimuli, and (3) this asymmetry between responses to superior and inferior stimuli would decrease with stimulus contrast (**Figure 2.23C, 2.24**). Next, we tested these predictions in behaving mice. OKR in the superior and inferior directions was measured in response to high-contrast (full) and low-contrast (20% relative) oscillating gratings. All of the linear predictions were consistent

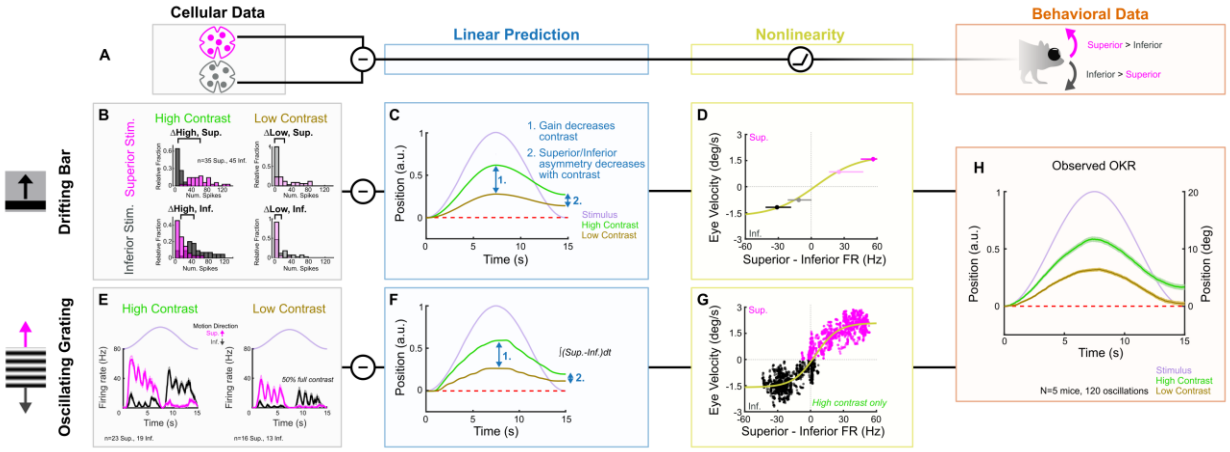

Figure 2.23 ON direction-selective retinal ganglion cell (oDSGC) responses predict the optokinetic reflex (OKR) across stimulus types, directions, and contrasts.

(Figure caption continued on the next page)

(Figure caption continued from the previous page)

(**A**) Schematic of the putative computation between oDSGCs and OKR, consisting of a subtraction between Superior and Inferior oDSGC spikes and a nonlinearity. (**B–H**) Two separate implementations of the subtraction model described in (**A**). (**B–D**) Prediction of OKR behavior from oDSGC spike responses to the drifting bar stimulus. (**B**) Distributions of Superior (magenta) and Inferior (gray) oDSGC spike responses across high-contrast (left) and low-contrast (right, 20% relative) superior (top) and inferior (bottom) drifting bars. The brackets denote the difference between the medians of the Superior and Inferior oDSGC response distributions in each condition. (**C**) Linear predictions of OKR are made for the average eye velocity over the course of each half oscillation cycle based on the difference in firing rate between Superior and Inferior oDSGCs (i.e. brackets in [**B**]) to high- and low-contrast bars drifting in the corresponding stimulus direction. The shape of the curves as sinusoids is inferred from the stimulus position over time (lavender). (**D**) The empirically computed nonlinearity shows the relationship between linear behavioral predictions (as in [**C**]) from the drifting bar stimulus and the corresponding average eye velocities measured during behavioral OKR experiments for superior (magenta points) and inferior (gray points) stimuli at high (dark points) and low (light points) contrast. The points indicate univariate medians for each condition and whiskers are 95% confidence intervals computed via bootstrapping (vertical error bars are too small to see). The solid line is a fitted sigmoid function. (**E–G**) Prediction of OKR behavior from oDSGC responses to an oscillating sinusoidal grating. (**E**) Median responses of Superior (magenta) and Inferior (gray) oDSGCs across a single cycle of the oscillating grating for high-contrast (left) and low-contrast (right, 50% relative) stimuli. Lavender traces represent the relative position of the stimulus across time. Directions of superior/inferior motion are in visual space and indicated by arrows. These recordings were made using two-photon targeting. (**F**) Linear predictions of OKR across time made by subtracting the instantaneous firing rates of Superior and Inferior oDSGCs to generate predictions for instantaneous eye velocity, and integrating to predict eye position. (**G**) The empirically computed nonlinearity shows the difference between Superior and Inferior oDSGC firing rates plotted against the time-matched average eye velocity of behaving animals. Each small point represents the average firing rate difference and eye velocity at a single time point over the course of one stimulus oscillation cycle. Magenta points represent superior eye velocities (i.e., above 0 on the ordinate), and gray points represent inferior eye velocities (i.e., below 0 on the ordinate). The solid line is a fitted sigmoid function. Only data for the high-contrast condition were used. (**H**) Mean eye position of behaving mice in response to a single oscillation of a high-contrast (green, as in **Figure 2.1I**) or low-contrast (tan, 20% relative) gratings. Compare to linear predictions in (**C**) and (**F**).

with behavior (**Figure 2.23H, 2.24, 2.26**). Most notably, gain decreased with stimulus contrast (**Figure 2.23H, 2.24H, I, and P, 2.26, 2.27**), and the asymmetry between superior and inferior OKR that we originally noticed under high- contrast conditions diminished in response to low-contrast stimuli (**Figure 2.23H, Figure 2.24 1L, M, and Q, 2.26**). While these results may be related, they do not necessitate each other, and instead rely on further subtleties in the relationship between Superior and Inferior oDSGC responses at both contrasts. Indeed, permuting the behavioral predictions by scrambling which cellular responses were assigned to superior/inferior motion and high/low contrast revealed that only five permutations (out of 256 possibilities, 1.95%) accurately matched our behavioral results. Consistent with these findings, the relationship between our linear predictions and behavioral results was fit well by a monotonic function that was near linear within the measured regime (**Figure 2.23D**).

Finally, we tested whether instantaneous subtraction of Superior and Inferior oDSGC firing rates on millisecond timescales could also predict vertical OKR behavior. We directly recorded the spikes of Superior and Inferior oDSGCs in response to oscillating gratings with the same parameters as those used to induce behavioral OKR. This stimulus evoked more spikes in Superior oDSGCs as gratings drifted dorsal to ventral on the retina (superior motion), and more spikes in Inferior oDSGCs as gratings drifted ventral to dorsal on the retina (inferior motion) (**Figure 2.23E, 2.25C and D**). To make behavioral predictions, the average population instantaneous firing rates of Superior and Inferior oDSGCs were subtracted every 5 ms over the course of an oscillation cycle (**2.25E and F**). Such values constituted linear predictions of instantaneous eye velocity for each time point, and their cumulative integrals yielded predictions of eye position (**Figure**

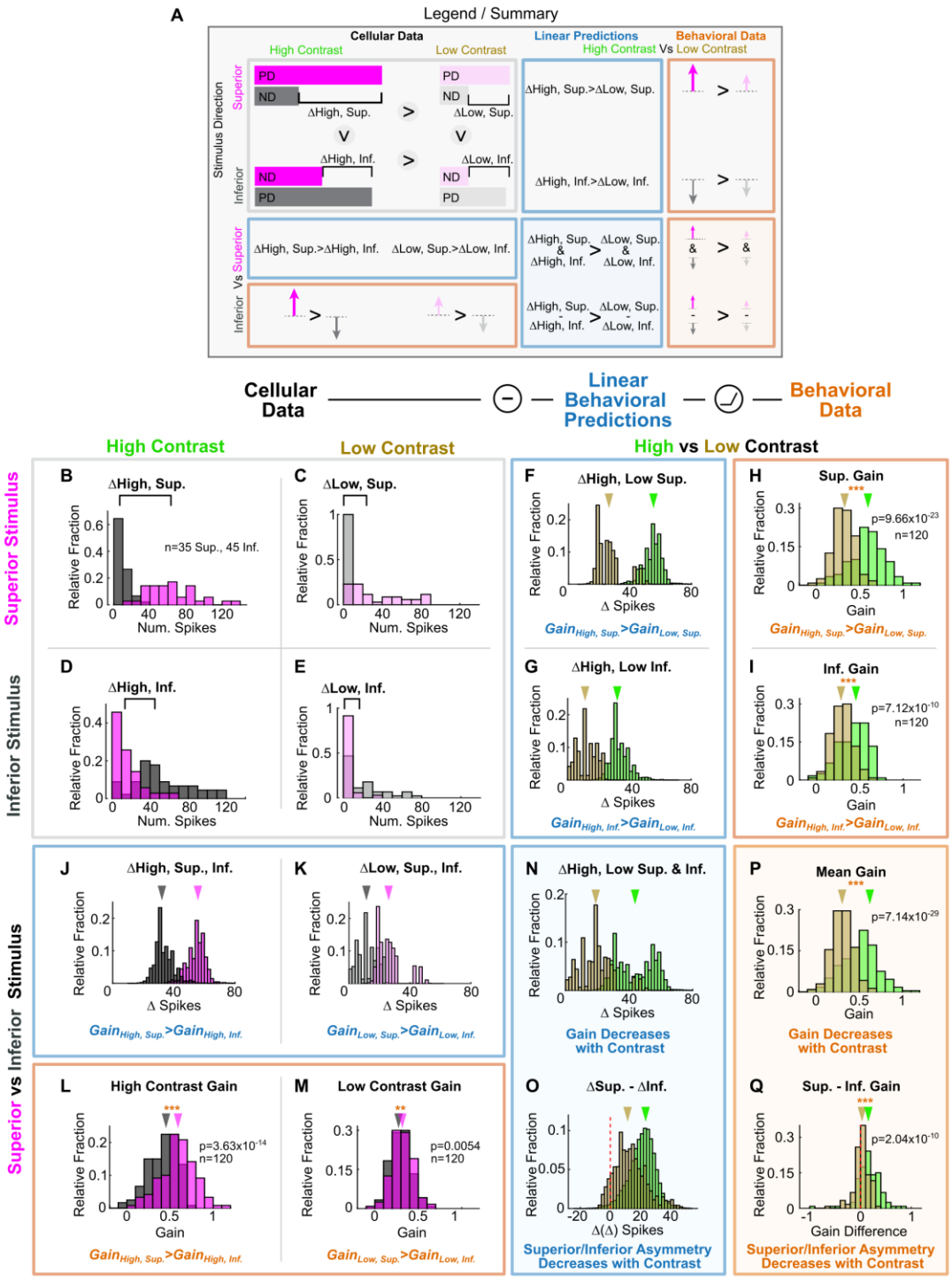

Figure 2.24 Behavioral prediction for the optokinetic reflex (OKR) from spike responses to the drifting bar stimulus.

(Figure caption continued on the next page)

(Figure caption continued from the previous page)

Spikes of Superior and Inferior ON direction-selective retinal ganglion cells (oDSGCs) in response to the drifting bar stimulus were used to predict the magnitude of OKR gain in behaving animals. (**A**) Legend and summary for panels (**B–Q**). Cellular data (gray box): the responses of Superior (magenta) and Inferior (gray) oDSGCs to preferred (PD) and null (ND) direction drifting bars at high (left column) and low (20% relative, right column) contrasts. Linear predictions (blue boxes): the differences between responses in the preferred and null directions across cell types, represented by Δ, provide predictions of the relative OKR gain across stimulus directions and contrasts. Behavioral results (orange boxes): arrows represent the magnitude of OKR gain measured in behaving mice across stimulus directions and contrasts. Dark arrows represent high-contrast stimuli, and light arrows represent low-contrast stimuli. (**B–E**) Cellular data: distributions of superior (magenta) and Inferior (gray) oDSGC spike responses to superior (top row) and inferior (bottom row) stimuli at high (left column) and low (right column) contrast. Brackets above show the difference between the medians of the two distributions. Same data plotted in **Figure 2.23B**. (**F–G, J–K, N–O**) Linear predictions from data in (**B–E**) for how behavioral OKR gain changes across stimulus directions and contrasts. The asymmetries in the tuning curves of Superior and Inferior oDSGCs resulted in four first-order linear predictions for how OKR gain changes across stimulus conditions: (1) for superior stimuli, gain is greater in response to high-contrast stimuli than to low-contrast stimuli (**F**), (2) for inferior stimuli, gain is greater in response to high-contrast stimuli than to low-contrast stimuli (**G**), (3) at high-contrast, gain is greater in response to superior stimuli than to inferior stimuli (**J**), and (4) at low-contrast, gain is greater in response to superior stimuli than to inferior stimuli (**K**). Two additional second-order hypotheses were made that rely on an approximately linear relationship between differences in oDSGC output and gain in the tested regime: (5) gain is greater under high-contrast, regardless of stimulus direction (**N**), and (6) behavioral asymmetries in response to superior and inferior stimuli diminish with decreasing contrast (**O**). (**H–I, L–M, P–Q**) The six linear predictions were tested by measuring OKR in behaving mice in response to superior and inferior oscillating gratings at high- and low-contrast. All six linear predictions accurately matched behavior. Distributions in these panels are made up of the average OKR gain over the course of individual half oscillation cycles, arrows indicate medians (two-sided signed-rank). *p<0.05, **p<0.01, ***p<0.001.

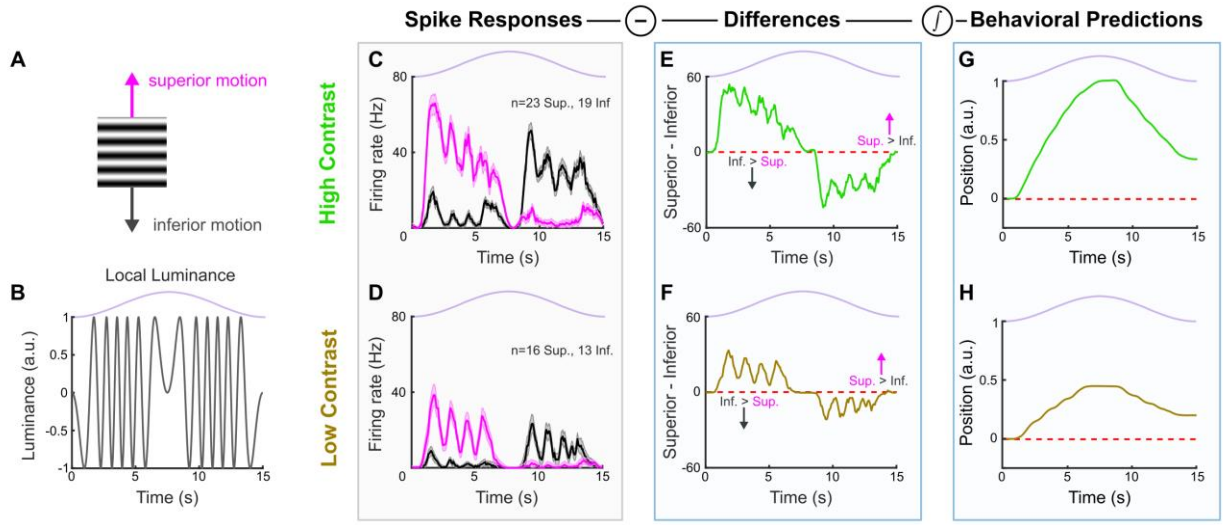

Figure 2.25 ON direction-selective retinal ganglion cell (oDSGC) responses to oscillating gratings.

(**A**) Oscillating sinusoidal gratings used in oDSGC electrophysiology were equivalent to those used in behavioral experiments. Motion directions apply to all panels. (**B**) Luminance of a single point in space as the sinusoidal grating completes one oscillation cycle. A value of 1.0 along the ordinate indicates full luminance and –1.0 indicates minimal luminance. This luminance function is determined by both the spatial frequency of the grating and the velocity of the sinusoidal oscillation. The light available to a single oDSGC follows such luminance fluctuations over the course of a single stimulus oscillation cycle, but the position of the oDSGC relative to the phase of the grating will cause a corresponding phase shift in its luminance function. These luminance oscillations therefore likely account for the high-frequency oscillations seen in (**C–F**). Stimulus position (in the oscillation cycle) is shown above in lavender. (**C**) Median spike responses of Superior (magenta) and Inferior (gray) oDSGCs over the course of a single high-contrast oscillation cycle. Two-photon targeting was used during all recordings in this data set. Error bars represent standard error of the mean. (**D**) Same as (**C**), but for a low-contrast stimulus, which, for this experiment, was defined as 50% contrast relative to the high-contrast stimulus (see 'Materials and methods'). (**E, F**) Moment-by-moment subtraction of the median Inferior oDSGC firing rate from the median Superior oDSGC firing rate for (**E**) high- and (**F**) low-contrast gratings. Values fall above unity (dashed red line) when Superior oDSGCs spike more than Inferior oDSGCs, and below unity when Inferior oDSGCs spike more than Superior oDSGCs. This subtraction constitutes a linear prediction of eye velocity for each point in time. (**G, H**) Linear predictions of eye position across time for a single (**G**) high- and (**H**) low-contrast oscillation cycle. These predictions are the cumulative integral of the firing rate differences shown in (**E**) for high-contrast and (**F**) for low-contrast. For all plots, the lavender trace indicates the position of the grating stimulus in its oscillation cycle across time. Two-photon targeting was used during all recordings in this data set.

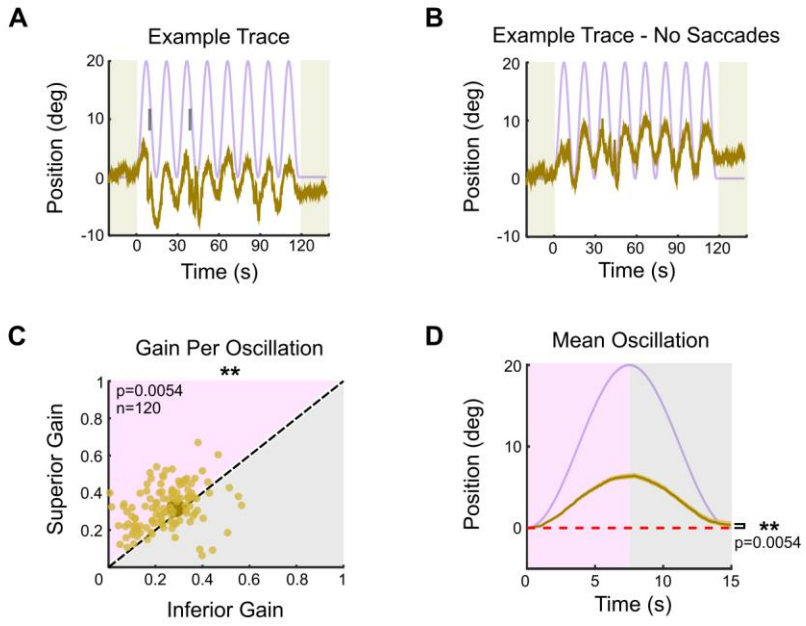

Figure 2.26 The optokinetic reflex (OKR) at low contrast.

Eye movements were measured from head-fixed mice in response to an oscillating sinusoidal grating. All parameters of the grating were the same as under high-contrast conditions (Figure 2.1), except for the grating contrast, which was five times lower (i.e., 20% relative contrast). (**A**) Example of OKR in response to the vertically oscillating low-contrast grating. The eye position is shown in tan, and the stimulus position is shown in lavender. Saccades are indicated by tick marks. (**B**) Same as (**A**), but with saccades ('fast nystagmuses') removed to reveal the asymmetry between superior and inferior OKR. For each epoch, animals viewed eight oscillation cycles lasting a total of 120 s, flanked by 20 s of a static grating (shaded regions). (**C**) Average gain of slow nystagmus during the superior versus inferior stage of individual oscillations. Each small dot is a single oscillation. The region of magenta (or gray) indicates that gain was greater for the superior (or inferior) stage of the oscillation. Points that fall on the line indicate equivalent gain for both stimulus directions. Large point and whiskers represent univariate medians and 95% confidence intervals (via bootstrapping), respectively. Significance value indicates whether the points tend to fall unevenly on one side of the unity line (two-sided signed-rank). (**D**) Eye position (tan) and stimulus position (lavender) averaged across all oscillations and all animals (mean ± SEM). Starting eye position is normalized to 0° at cycle onset. The average ending eye position is displaced in the superior direction (two-sided signed-rank). N = 5 mice for all experiments; n = number of trials.

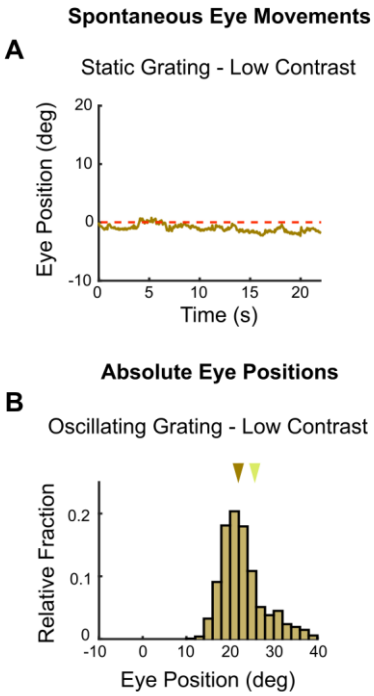

Figure 2.27 Baseline vertical eye movements to low-contrast stimuli (see also Figure 2.2).

Vertical eye movements were measured in response to static, low-contrast (20% relative) gratings to calculate eye drifts for baseline subtraction. (**A**) Example raw eye trace over 22 s of a static low-contrast grating. The calculated position of the eye drifts downward over time. This may reflect true eye movements or a calibration error in our recording configuration, but these two possibilities cannot be disambiguated (see 2.4 Materials and methods). The magnitude of eye position drift during static gratings is approximately 11-fold less than the magnitude of the eye movements elicited by low-contrast moving gratings (**see Figure 2.2A** for comparison to high-contrast grating). (**B**) Absolute vertical position of the eye without drift correction during low-contrast gratings. Brown arrow marks the median of the distribution. Yellow arrow indicates median position of the eye prior to stimulus onset (as in **Figure 2.2C**). Spontaneous drift velocity was baseline subtracted from eye positions in response to low-contrast oscillating gratings since median eye position was similar to that measured in response to static gratings.

2.23F, 2.25G and H). Recordings were initially made in response to both high (full) and 20% relative contrast gratings; however, the low-contrast condition failed to evoke consistent spiking in oDSGCs. Thus, we instead used high (full) and 50% relative contrast gratings to predict how responses would change across contrasts. Moment-by-moment subtraction of oDSGC firing rates indicated that (1) eye movements would track the sinusoidal pattern of stimulus motion, (2) gain would decrease with decreasing stimulus contrast, (3) OKR would be asymmetric with greater gain in response to superior motion than inferior motion, and (4) asymmetries between Superior and Inferior OKR would decrease with decreasing stimulus contrast. Not only do these predictions match those generated from the drifting bar stimulus, but they also accurately predict OKR in behaving mice (**Figure 2.23H**). The moment-by-moment difference between Superior and Inferior oDSGC firing rates was also generally linearly related to the time-matched eye velocity of behaving animals, with nonlinear regimes occurring only at extreme firing rate differences (**Figure 2.23G**). Together, these results provide a neurophysiological explanation for how vertical OKR changes across multiple stimulus conditions and reveal that the circuit and cellular properties that shape oDSGC motion encoding have direct and predictable consequences for behavior.

2.3 Discussion

Our results depict a neurophysiological mechanism by which vertical OKR changes across stimulus conditions. We demonstrate that superior and inferior OKR are asymmetric in adult mice, and show how this behavioral phenomenon can be traced to novel asymmetries in the direction tuning properties of Superior and Inferior oDSGCs. Mechanistically, a shift in the balance of excitatory and inhibitory inputs across cell types

influences direction tuning, primarily through an effect associated with spike thresholding. Similar thresholding effects also confer contrast-sensitivity of the spike tuning curve, even when E/I is contrast-invariant. Together, these cellular properties accurately predict how vertical OKR changes with stimulus direction and contrast.

Directional asymmetries in OKR are common across species. Besides the vertical asymmetries investigated here, horizontal OKR is asymmetric in many organisms (Masseck and Hoffmann, 2009; Mowrer, 1936). This asymmetry manifests nearly universally as higher OKR gain in response to temporal-to-nasal (anterior) motion than to nasal-to-temporal (posterior) motion, and often only when stimuli are viewed monocularly. Such horizontal asymmetries may similarly be linked to direction tuning in the retina: while anterior-preferring oDSGCs are critical to horizontal OKR (Dhande et al., 2015; Osterhout et al., 2015; Yonehara et al., 2016), posterior-preferring oDSGCs were only recently identified in rodents and display distinct direction tuning properties compared to their anterior-preferring counterparts (Sabbah et al., 2017). Further, a subtraction mechanism between horizontally tuned oDSGCs may also underlie horizontal OKR (Hoffmann and Fischer, 2001). However, at least two confounds obscure a connection between the tuning properties of anterior and posterior oDSGCs and asymmetries in horizontal OKR. First, oDSGCs in the left and right eyes, and their contralateral central targets (NOT/DTN), encode different absolute directions of stimulus motion (reflection occurs over the sagittal body axis). To compensate, signals are compared across eyes/hemispheres prior to behavior (Hoffmann and Fischer, 2001), and, in some species, NOT/DTN receives descending, often binocular, inputs from visual cortex (Masseck and Hoffmann, 2009; Giolli et al., 2006; Liu et al., 2016; Wood et al., 1973). Second, recent studies have

suggested that ooDSGCs could be involved in horizontal OKR (Dhande et al., 2013; Kay et al., 2011). Asymmetries in the horizontal version of the behavior may thus depend on more complex considerations.

Analogous confounds are less concerning when considering the mechanisms that could account for asymmetries in vertical OKR. For one, stimuli that induce vertical OKR, such as the gratings used here, are perceived identically by both eyes. Interhemispheric communication is unlikely to influence behavior under such conditions. Though signals are probably also exchanged between the horizontal and vertical OKR pathways (Simpson, 1984; Giolli et al., 2006; Lilley et al., 2019), these channels may play a minimal role in shaping OKR to purely vertical stimuli. Finally, while it has been suggested that a vertically tuned ooDSGC may also project to MTN (Kay et al., 2011), this cell type was not clearly revealed by either anatomical or electrophysiological analyses during our retrograde labeling experiments (**Figure 2.5, 2.12**). Instead, we find that two populations of ganglion cells project to MTN, and that these cells can be classified as Superior and Inferior oDSGCs. These results are consistent with characterizations of MTN-projecting RGCs across many species (Yonehara et al., 2008; Yonehara et al., 2009; Cook and Podugolnikova, 2001; Dann and Buhl, 1987; Ruff et al., 2021). Thus, unlike for horizontal OKR, asymmetries in vertical OKR can be explained more simply by the physiology of oDSGCs.

Despite the possibility that asymmetries in vertical and horizontal OKR are influenced by separate mechanisms, the two phenomena could share a common ethological function. Optic flow associated with forward locomotion typically includes a large posterior component. Thus, it has been suggested that posterior OKR is less reliable

than anterior OKR in order to mitigate lateral eye movements that might otherwise occur when an animal walks forward (Tauber and Atkin, 1968). Similar reasoning may explain the asymmetry between superior and inferior OKR (Takahashi et al., 1978; Grasse and Cynader, 1988; Takahashi and Igarashi, 1977). Indeed, recent work in freely moving mice demonstrated that optic flow has a stronger inferior than superior component (Holmgren et al., 2021). Thus, the cellular and behavioral asymmetries identified in this study may provide an ethological advantage by mitigating aberrant eye movements during forward locomotion. Future work should address this possibility by mapping OKR gain as a function of the extent to which various stimuli reflect locomotion-associated optic flow.

From a physiological perspective, our results provide the first evidence that Superior and Inferior oDSGCs encode motion asymmetrically. Superior oDSGCs produce more spikes and have broader tuning curves than Inferior oDSGCs (**Figure 2.4**). These findings coincide with previous work demonstrating genetic (Al-Khindi et al., 2022) and anatomical differences between oDSGC types. Multiple transgenic lines are known to label either Superior or Inferior oDSGCs, but not both (Lilley et al., 2019; Yonehara et al., 2008; Yonehara et al., 2009; Ruff et al., 2021). The axons of Superior and Inferior oDSGCs take separate retinofugal tracts and project to different MTN subnuclei in mice (Yonehara et al., 2009). Additional differences exist between vertically and horizontally tuned oDSGCs (Dhande et al., 2015; Osterhout et al., 2015). The competitive advantage of mitigating OKR during forward locomotion may have thereby shaped the development of many differences between oDSGC types.

The asymmetric spike tuning of Superior and Inferior oDSGCs is associated with differences in the magnitude of excitatory synaptic input to each cell type (**Figure 2.10**).

Three synaptic partners are primary candidates for the source of this asymmetry: (1) glutamatergic input from bipolar cells (types 5 and 7), (2) cholinergic input from SACs, and (3) glutamatergic input from VGluT3 amacrine cells (Amthor et al., 2002; Yonehara et al., 2011; Yoshida et al., 2001; Mani et al., 2021; Matsumoto et al., 2019; Yonehara et al., 2013; Lee et al., 2014; Sivyer et al., 2019). Glutamatergic conductances in oDSGCs rely on AMPARs and NMDARs, whereas cholinergic conductances rely on nicotinic AChRs (Kittila and Massey, 1997). These conductances have been studied primarily in ooDSGCs and deserve further characterization in oDSGCs. Interestingly, VGluT3 amacrine cells also corelease glycine, which cancels oDSGC spiking in response to high-velocity stimuli (Mani et al., 2021; Summers and Feller, 2022; Lee et al., 2014; Sivyer et al., 2019). Asymmetries at the VGluT3-oDSGC synapse could coincide with differences in the speed tuning properties of Superior and Inferior oDSGCs. A combination of genetic, optical, and pharmacological manipulations could distinguish among these possible sources of asymmetric tuning.

In addition to the gain of excitatory inputs, other mechanisms could contribute to tuning curve differences between Superior and Inferior oDSGCs. Debate remains over the extent to which excitatory inputs to DSGCs are directionally tuned (Vaney et al., 2012; Matsumoto et al., 2019; Matsumoto et al., 2021; Percival et al., 2019; Poleg-Polsky and Diamond, 2011; Summers and Feller, 2022; Yonehara et al., 2013). Our data indicate that excitation may be less direction-selective in Superior than in Inferior oDSGCs (**Figure 2.10H**), which could contribute to their broader spike tuning curves. Qualitatively, excitation also showed a bimodal average tuning curve in Superior oDSGCs (**Figure 2.10G**) that matched their average spike tuning curve (**Figure 2.4G**). However, bimodal

spike tuning curves also resulted from directionally untuned depolarizing current injections in both cell types (**Figure 2.15C and D**), so the influence of excitatory tuning remains unclear. In addition, previous studies with simultaneous somatic and dendritic recordings have revealed that dendritic spikes in rabbit oDSGCs contribute to directional tuning (Sivyer and Williams, 2013). Different spatial distributions of voltage-gated sodium channels along dendrites could also contribute to asymmetric direction tuning between oDSGC types. Indeed, we show that Superior and Inferior oDSGCs have distinct morphologies (**Figure 2.13**). Thus, while a single-compartment conductance model captured the empirical data in this study (**Figure 2.18**), development of multicompartment models could elucidate potential contributions of dendritic spikes to asymmetric tuning between oDSGC types. Intriguingly, however, among mechanisms that are unlikely to explain differences between Superior and Inferior oDSGC tuning curves is that of direction-selective inhibition. We find that inhibition is more sharply tuned in Superior oDSGCs (**Figure 2.10C and D**), and that this is associated with sharper Vm tuning curves (**Figure 2.15K, arrowheads**). In agreement, analyses leveraging our parallel conductance model also demonstrated that, all else equal, sharper inhibitory tuning contributes to sharper Vm and spike tuning in oDSGCs (not shown). Nonetheless, empirically measured spike tuning curves are broader in Superior oDSGCs than in Inferior oDSGCs (**Figure 2.4J and K**). Thus, while the relationship between inhibitory tuning curve shape and spike tuning curve shape is nuanced and requires further investigation, the difference in spike tuning curve shape between Superior and Inferior oDSGCs is unlikely to be explained by inhibitory tuning. Evidently, other mechanisms, including differences in excitatory gain (**Figure 2.10G**), counteract and outweigh the influence of

differences in inhibition. Consequently, a comprehensive understanding of direction selectivity will require mapping the contributions of mechanisms that have been less well-studied than directionally tuned inhibition.

Further insight into how oDSGCs encode motion can be gained by comparing their tuning properties to those of the more comprehensively studied ooDSGCs. While prior work has focused on speed tuning as the primary difference between oDSGCs and ooDSGCs (Oyster, 1968; Oyster et al., 1972; Mani et al., 2021; Summers and Feller, 2022; Sivyer et al., 2019), our results reveal an additional difference between these two classes of DSGCs that has been previously overlooked: oDSGCs are contrast sensitive (**Figure 2.20**), whereas ooDSGCs are not (Sethuramanujam et al., 2016). In ooDSGCs, preservation of E/I across contrasts is apparently critical for retaining contrast-invariant direction tuning (Poleg-Polsky and Diamond, 2016b; Sethuramanujam et al., 2017). Counterintuitively, we find that E/I in oDSGCs is also relatively stable across contrasts (**2.21 D and E**). Therefore, stability of E/I is not alone sufficient for contrast-invariant spike tuning; independence from thresholding effects is also required. Indeed, thresholding modulates oDSGC direction tuning following changes to either E/I (**Figure 2.15, 2.18**) or the absolute magnitude of E and I (**Figure 2.21 1F**). Evidently, the influence of thresholding constitutes a major difference in the mechanisms that govern how oDSGCs and ooDSGCs encode motion.

That E/I is contrast-invariant in both oDSGCs and ooDSGCs also indicates some extent of shared circuitry between these cell types. Contrast invariance of E/I in ooDSGCs relies on postsynaptic NMDA conductances and constrains possible presynaptic wiring motifs (Poleg-Polsky and Diamond, 2016b; Sethuramanujam et al., 2017). oDSGCs likely

share many of these features. Indeed, serial block-face electron microscopy has confirmed that oDSGCs and ooDSGCs share many of their presynaptic partners (Briggman et al., 2011; Ding et al., 2016; Mani et al., 2021; Matsumoto et al., 2019; Matsumoto et al., 2021). Nonetheless, differences in the intrinsic properties between and within DSGC classes, including dependence on thresholding, could magnify the impact of subtle circuit differences on spike output.

Finally, our results show that vertical OKR is predicted by a simple subtraction between the outputs of Superior and Inferior oDSGCs (**Figure 2.23**). It is interesting that asymmetries in oDSGCs are not apparently corrected by downstream circuitry, considering that normalization operations pervade the nervous system (Carandini and Heeger, 2011). One explanation is that there is no simple compensatory solution to normalize the responses of Superior and Inferior oDSGCs because multiple stimulus parameters (e.g., stimulus direction and contrast) simultaneously affect the asymmetry magnitude. On the other hand, the ethological advantage of asymmetric OKR (i.e., mitigating aberrant eye movements during forward locomotion) may have provided sufficient evolutionary pressure to allow asymmetries between Superior and Inferior oDSGCs to propagate to behavior when they might otherwise have been compensated. Regardless, a linear subtraction of oDSGC outputs offers an accurate and parsimonious explanation of vertical OKR. Moreover, this algorithm fits well with both the anatomy and physiology of MTN and the isolation of the vertical OKR pathway from other visual circuits (Giolli et al., 2006; Yonehara et al., 2009; van der Togt et al., 1993; Soodak and Simpson, 1988; Giolli et al., 1985; Grasse and Cynader, 1982; Natal and Britto, 1988; Simpson et al., 1979).

Similar subtraction algorithms are prevalent across the animal kingdom. In the mammalian retina, such computations confer both the spatial center-surround (Barlow, 1953; Hartline et al., 1952; Kuffler, 1953) and chromatic dichotomy (Dacey et al., 2014; De Monasterio and Gouras, 1975; Field et al., 2009) of receptive fields. In Drosophila, spatially offset antennae allow accurate estimation of wind velocity by differentiation of signals across two input sites (Suver et al., 2019). Similar mechanisms likely underlie tropotaxic orienting behaviors that also rely on spatially offset receptors, including arthropod antennae (Martin, 1965), reptile forked tongues (Schwenk, 1994), and mammalian ears (Middlebrooks and Green, 1991). The ubiquity of this circuit motif may reflect an efficient solution for integrating complementary information streams. Our results highlight how such circuits can be influenced by subtle asymmetries across input channels. Further investigation will determine whether diverse sensory systems rely on asymmetric inputs to adaptively change behavior across stimulus conditions.

2.4 Materials and Methods

2.4.1 Animals subjects

Adult wild type C57BL/6 mice between the ages of postnatal day P60 and P100 of both sexes were used for all experiments. Animals were kept on a 12 hr dark–12 hr light cycle with continuous access to food and water. All experiments were performed in accordance with protocols approved by the University of California, San Francisco Institutional Animal Care and Use Program.

2.4.2 Behavior rig

To accurately evoke and measure OKR, we custom-designed a behavior rig that was capable of presenting full-field, binocular stimuli to behaving mice. The design of the

rig was based on Denman et al., 2017. Briefly, an acrylic hemisphere (diameter = 24 inches, California Quality Plastics) was covered with a custom paint that had 50% diffuse reflectivity between 350 and 750 nm (Twilight Labs) in order to limit reflections within the hemisphere. Stimuli were emitted from a DLP projector with peak emission at 405 nm (LightCrafter through EKB Technologies) and were reflected onto the hemisphere via a silver-coated brass hemisphere ('convex mirror,' diameter = 6 inches, Wagner). Stimuli were built using Psychopy (Peirce, 2007) (https://www.psychopy.org) and a custom wrapper to manage their sequential presentation and alignment with eye-tracking videos. The wrapper and stimuli are both available at https://github.com/ScottHarris17/Bassoon; Aberrations in the projection were corrected by applying a manually fit spherical morph to all stimuli (Meshmapper, https://www.paulbourke.net). Blackout curtains surrounded the rig to minimize light contamination.

2.4.3 Unidirectional OKR stimuli

Unidirectional sinusoidal gratings were presented in groups of six consecutive epochs. Each epoch consisted of 20 s of a static grating, followed by 60 s of a grating drifting either directly upward or directly downward, and an additional 20 s of a static grating. The six total epochs consisted of three upward and three downward epochs that were randomly interleaved. All gratings moved at 10°/s and had a spatial frequency of 0.15 cycles/°. The brightest part of the grating evoked 1.38 × 103 S-cone photoisomerizations/s and the darkest part of the grating evoked 25.9 S-cone photoisomerizations/s. M-cone photoisomerizations were 60% those of S-cone.

2.4.4 Oscillating OKR stimuli

Oscillating sinusoidal gratings were presented in groups of three consecutive epochs. Each epoch consisted of 20 s of a static grating, followed by 120 s of oscillation, and an additional 20 s of a static grating. During the oscillation, the grating velocity was modulated sinusoidally up and down. The oscillation had an amplitude of 20°, a period of 15 s, and a phase shift of 0°. Eight oscillations were completed over the course of one epoch. All gratings had a spatial frequency of 0.15 cycles/°. The intensities of high-contrast oscillating gratings were equivalent to those used for unidirectional OKR stimuli and had fivefold greater Michelson contrast than low-contrast oscillating gratings (i.e., low-contrast gratings were ‘20% relative contrast’). High- and low-contrast gratings had the same mean luminance.

2.4.5 Eye tracking

Prior to eye-tracking experiments, animals underwent stereotaxic surgery for implantation of a custom head-fixing apparatus. After surgery, animals were given 7 days to recover. Animals were then gradually habituated to the behavior rig by spending increasing amounts of time head-fixed on the rig for five consecutive days prior to the beginning of experiments.

Eye-tracking experiments were run over the course of up to 3 days per animal. Each animal spent no more than 30 min per day on the rig. During experiments, mice were head-fixed in the center of the hemisphere, which filled the entirety of their visual field. Eye movements were recorded using a GigE camera (Photonfocus), an infrared filter, and a hot mirror (Edmund Optics) that allowed the camera to be positioned outside of the animal’s field of view. Infrared LEDs (880 nm) were mounted on the top and side

of the camera to generate corneal reflections that marked the meridian and equator of the eye, respectively. StreamPix software (NorPix) was used to capture video of the eye and align it to stimuli via TTL signals.

After completion of the experiments, Deeplabcut (https://www.deeplabcut.org) was used to train a neural network to locate the pupil and corneal reflection on each video frame. The two-dimensional pupil location was then translated to angular eye position for every recording frame using the methods described by Stahl et al., 2000; Stahl, 2004 and Zoccolan et al., 2010. In short, prior to experiments, we calibrated the eye tracking system for each animal by repeatedly swinging the camera ±6° in the horizontal plane and measuring the relative position of the pupil and corneal reflection. This process was repeated across five different luminances to fit a linear regression between pupil size and angular eye position. The meridian and equator of the eye were measured by turning on the top- and side-aligned infrared LEDs in sequence. During experiments, only the top LED was on. Angular eye position was then calculated as

(1) $\phi = arcsin\left(\frac{\Delta x}{\sqrt{R_{p0}^2 - \Delta y^2}}\right)$

and

(2) $\theta = arcsin\left(\frac{\Delta y}{R_{p0}}\right)$

where ϕ is the horizontal eye position, θ is the vertical eye position, Δx is the horizontal distance measured between the eye center and the pupil, Δy is the vertical distance measured between the eye center and the pupil, and R_{p0} is the radius of rotation between the pupil and the eye's center, which was computed empirically for each pupil diameter

for each animal. For all stimuli, fast and slow nystagmus were separated on the basis of eye velocity and acceleration using custom MATLAB scripts. For all analyses in this report, we consider only θ, the vertical eye position, and $\Delta\theta/\Delta t$, the vertical component of eye velocity.

By measuring the vertical eye velocity ($\theta/\Delta t$) in response to the static gratings (multiple contrasts) that occurred before the onset of all stimuli, we also computed a baseline median eye drift of 0.0787°/s (IQR: 4.1792°/s; p=0.015) in the ventral direction across animals. This drift may reflect either the error associated with the estimation of the eye's center during our calibration process or a natural biological eye drift associated with our rig. It is not possible to disambiguate between these possibilities. Since the eye position was near neutral for the time in which this drift was calculated, we baseline subtracted it from the eye position traces for all oscillating grating stimuli (for which the average eye position was also approximately neutral). For unidirectional gratings, we were unable to calculate an appropriate drift for baseline subtraction since the eye position was not often near neutral during these stimuli (**Figure 2.2, 2.27**).

For oscillating OKR stimuli, saccades were removed from the eye trace post hoc. This was achieved by setting $\Delta\theta/\Delta t$ during saccades to its value immediately prior to the saccade onset, and then reintegrating $\Delta\theta/\Delta t$ to compute the position of the eye across time.

2.4.6 *Retrograde labeling*

MTN-projecting retinal ganglion cells were labeled via stereotaxic injection of red fluorescent retrobeads (Lumafluor) into MTN. Prior to surgery, mice were anesthetized by IP injection of ketamine/xylazine and 5% isoflurane inhalation. Once fully anesthetized,

as assessed by absence of the pedal reflex, animals were transferred to a sterile-heated surface and the eyes were covered with a lubricating ointment. Then, 2% isoflurane was administered continuously to maintain anesthesia. Fur was removed prior to incision and lidocaine (<7 mg/kg) was injected locally under the scalp. After incision, animals' heads were leveled by aligning bregma and lambda in the horizontal plane. A burr hole was drilled at A/P: 0.00 mm, M/L: 0.85 mm from bregma. All injections were performed into the right MTN. A glass needle filled with retrobeads (diluted 1:3 in distilled water) and connected to a Hamilton syringe was lowered into the burr hole at an angle of 30° A/P to a depth of 5.36 mm below the surface of the brain. After 10 min, an injection of 400 nL was made at a rate of 5 nL/s. After injection, the needle was left in place for an additional 10 minutes before removal. The scalp was sutured and animals recovered in a heated cage. Analgesics (buprenorphine [0.05–0.1 mg/kg] and NSAIDs [5–10 mg/kg]) were delivered via subcutaneous injection immediately after animals awoke from anesthesia, again 12 hours later, and a third time the following morning. Animal health was monitored for 3 days after surgery and additional analgesics were administered as required. Labeling of retinal ganglion cells in the contralateral eye was typically observed as soon as 48 hours following surgery and did not increase or decrease with time.

2.4.7 Empirical mosaic analysis

All mosaic analyses occurred ≥2 days after injection of the retrograde tracer into MTN. Retinas were dissected, fixed in 4% PFA for 20 min, and flat-mounted onto a microscope slide with a spacer. One widefield fluorescent image was taken of each retina. The location of each labeled cell in the image was determined using custom MATLAB scripts. Only retinas with near complete labeling (determined as greater than 500

identified RGCs) were included in analyses. The retina perimeter, optic nerve head, and dorsal-ventral axis were manually measured. These points were used to define a normalized polar coordinate system that allowed for the comparison of cell locations and densities across multiple retinas. Density recovery profiles were calculated using the methods described by Rodieck, 1991.

2.4.8 Mosaic models

To model spatial distributions of single and multiple mosaics, we randomly generated mosaics in a model circular retina that had an equivalent radius to that of the average whole-mount retina used for empirical density recovery profile estimation. 'Cell bodies' were modeled as circles with radius 15 μm and scattered randomly across the model retina so long as the following conditions were met: (1) no two cell bodies can overlap in space (i.e., cells must form a 'monolayer'), and (2) adjacent cells that are members of the same mosaic must obey a (noisy) exclusion zone that is set by the mosaic coverage factor (number of cells/retina area). Coverage factors were changed systematically such that the total number of cells across all mosaics – regardless of the number of mosaics being modeled – always approximated the number of retrogradely labeled cells per retina in our empirical data set. Density recovery profiles were computed as described for empirical data.

2.4.9 Electrophysiology tissue preparation

All electrophysiology experiments occurred ≥2 days after injection of the retrograde tracer into MTN. Prior to electrophysiology experiments, mice were dark-adapted for ≥12 hr. Mice were then euthanized by cervical dislocation and the left eye was enucleated (contralateral to the right MTN injection). Retina dissections occurred in the dark using

infrared converters and warmed bicarbonate-based Ames solution, equilibrated with 95% O_2/5% CO_2. Brains were simultaneously harvested and fixed in 4% PFA for imaging and to confirm that the retrograde tracer was properly injected into MTN. Retinas were whole-mounted, keeping track of orientation, and continuously perfused at 10 mL/min with freshly equilibrated Ames heated to 35°C throughout the course of experiments.

2.4.10 Retinal location of recorded cells

At the beginning of electrophysiology experiments, the center and radius of the retina were measured: two-dimensional coordinates of eight standardized points around the perimeter of the retina were noted. The center of the retina was estimated by computing the median of the circumcenters of all unique triangles that could be formed from these eight points. The radius of the retina was estimated by finding the median radius of the circles that circumscribed these same triangles. In all cases, the convex hull of the whole-mount retina was well approximated by a circle and the retina center estimation was near the optic nerve head. The coordinates of each recorded cell were computed in reference to the retina center. Cell locations were combined across retinas by normalizing to the estimated radius in a polar coordinate system.

2.4.11 Identification of MTN-projecting RGCs

An NIR light source (950 nm, Sutter) was used to visualize the tissue for the majority of the experiment. To identify retrogradely labeled ganglion cells, a green epifluorescent light was turned on briefly (~1–3 s) prior to recording from each cell. This light evoked a moderate number of spikes in oDSGCs. At least 1 min of darkness was provided between the offset of the epifluorescent light and the beginning of subsequent experiments. The epifluorescence exposure likely contributed variance to our dataset by

differentially modulating adaptation states along the dorsal/ventral retinal axis as the absorption spectra of cone photoreceptors change. However, for all electrophysiology experiments, care was taken to record from comparable spatial distributions of Superior and Inferior oDSGCs such that reported asymmetries between cell types cannot be attributed to uneven proportions of Superior and Inferior oDSGCs recorded from dorsal and ventral retina. Further, repeated exposures to epifluorescence throughout an experiment had no effect on oDSGC responsivity. Moreover, asymmetries between Superior and Inferior oDSGC tuning curves were observed within each retinal quadrant and between pairs of Superior and Inferior oDSGCs (within 30 μm of each other) across the retina (**Figure 2.8**).

For a subset of cell-attached experiments, two-photon targeting was employed to validate and replicate our central findings. In these experiments, retrogradely labeled retinal ganglion cells were targeted on a two-photon microscope with peak emission at 860 nm and laser power of approximately 17–40 mW. Two-photon and epifluorescence targeting were never performed on the same retina. Data collected during two-photon targeting are presented *only* in **Figures 2.7, 2.9**, **2.22**, **2.23E–G, 2.25**. The figure legends also clearly indicate experiments in which two-photon targeting was used. Unless otherwise stated, electrophysiology data came from experiments in which epifluorescence was used.

2.4.12 Electrophysiology

Patch electrodes were pulled from borosilicate glass (Sutter) to 3–5 MOhm resistance using a Narishige puller. A MultiClamp 700B Amplifier (Axon Instruments) with

acquisition rate of 10 kHz was used for all recordings. Cell-attached experiments were performed using electrodes filled with HEPES buffered Ames. Voltage-clamp experiments were performed using fresh electrodes filled with cesium methanesulfonate (Care et al., 2019). Current-clamp experiments were performed using fresh electrodes filled with potassium aspartate (Care et al., 2020). A subset of cells were recorded in both cell-attached and whole-cell configurations. In these cases, cell-attached recordings were performed first. Voltage-clamp and current-clamp recordings were never made from the same cell. Electrophysiology experiments were conducted using Symphony DAS (https://symphony-das.github.io/), and light stimuli were constructed and presented using Stage (https://stage-vss.github.io/).

2.4.13 Light increment stimulus

Light increments were the first stimulus to be presented to each cell and were often additionally interleaved between other stimuli. Light increments were delivered for 1 s from darkness using an LED with peak emission at 405 nm. The increments had an intensity of 8.6×10^4 S-cone photoisomerizations/s. M-cone photoisomerizations were 79% of those of S-cone. The LED spot had diameter 500 μm or 300 μm (no significant difference was observed in the responses to either spot size), was centered on the cell body of each recorded cell, and was focused on the photoreceptor layer of the retina.

2.4.14 Drifting bar stimulus

Drifting bars were presented from a DLP projector with peak emission at 405 nm (LightCrafter through EKB Technologies, same model as used for behavioral experiments). The native optics of the projector were replaced with neutral density filters and optics to focus stimuli on the photoreceptor layer of the retina via a condenser. The

projector covered a rectangular area of 427 × 311 μm that was centered on the soma of each recorded cell. Drifting bars had a width of 3.2° and moved at 10°/s using a conversion factor of 31 μm/° (Remtulla and Hallett, 1985). Bar height was limited only by the area covered by the projector. High-contrast bars measured 2.4×10^4 S-cone photoisomerizations/s and were presented on top of a background of 124 S-cone photoisomerizations/s (for drifting bar experiments utilizing two-photon targeting [**Figures 2.7, 2.9, 2.22**] the background was 1.9×10^3 S-cone photoisomerizations/s). M-cone photoisomerizations were 74% of those of S-cone. See below for the specifications of low-contrast bars. For tuning curve estimation, bars moved in eight directions separated by 45°. The presented sequence of stimulus directions was randomized for each recording. Tuning curves were estimated by mean measurements taken over five repetitions per stimulus direction.

2.4.15 Retinal ganglion cell classification

Retrogradely labeled retinal ganglion cells were classified as either Superior or Inferior oDSGCs if they had a direction selectivity index of greater than 0.05 and a preferred direction more than 30° away from the temporal-nasal axis, as calculated by spike outputs measured in the cell-attached configuration. The vast majority of recorded cells met these criteria, but those that did not were excluded from further analyses (**Figure 2.5**). All recorded cells in our data set were dominated by ON responses to a light increment (**Figure 2.12**).

2.4.16 Current injections

Depolarizing or hyperpolarizing currents were continuously injected while measuring voltages across stimulus directions in the current-clamp configuration. The

magnitude of current injections changed subtly from cell to cell depending on resting membrane potential, input resistance, and spike threshold. On average, depolarizing current injections increased the membrane potential by ~6 mV (to ~–48 mV), whereas hyperpolarizing current injections decreased the membrane potential by ~6 mV (to ~–60 mV). Depolarizing injections were always small enough such that the new resting membrane potential remained below spike threshold and each cell's baseline firing rate was 0 Hz. The order of depolarizing and hyperpolarizing injections was randomized across cells.

2.4.17 Isolation of spikes and subthreshold voltages

From current-clamp recordings, the onset and offset of each action potential were determined using the first and second derivatives of the voltage trace and a fixed minimum refractory period. The subthreshold voltage was then linearly interpolated between action potential onsets and offsets.

2.4.18 Subthreshold voltage tuning curves

The maximum voltage deflection from baseline was used to determine subthreshold membrane potential tuning curves. Values were averaged over five repetitions for each stimulus direction. Tuning curve metrics were calculated as for spikes.

2.4.19 Electrophysiology at low contrast

For experiments using epifluorescence targeting (i.e., all data in **Figures 2.4, 2.20, and 2.21**), low-contrast drifting bars had an intensity of 0.5×10^4 S-cone photoisomerizations/s (approximately fivefold dimmer than high-contrast bars, or '20% relative contrast') from the same background of 124 S-cone photoisomerizations/s. For experiments using two-photon targeting (i.e., **Figure 2.22**), low-contrast bars had an

intensity of 2.4 × 10^4 S-cone photoisomerizations/s and were presented on top of a background of 1.3 × 10^4 S-cone photoisomerizations/s. For both epifluorescence and two-photon targeting experiments, all other stimulus parameters were equivalent to what they were under high-contrast conditions. In a subset of cells, low-contrast bars failed to elicit spikes for every stimulus direction. In such cases, the cell's spike tuning curve area was set to 0, the area of its normalized tuning curve was set to 0, and its direction selectivity index was set to 1. We chose this convention because of the observation that, across cells, as the total number of spikes approached 0, the direction selectivity index approached 1 and the area of the normalized tuning curve approached 0. This pattern also fits the prediction made by our parallel conductance model. Cells with no responses under low contrast were classified as Superior or Inferior on the basis of their responses to high-contrast stimuli.

2.4.20 Immunohistochemistry

Individual ganglion cells were filled with either Lucifer yellow or biocytin during electrophysiology experiments. Retinas were subsequently fixed in 2% paraformaldehyde for 20 min at room temperature. The following protocol was used to enhance for the cell fills (anti-Lucifer yellow [Life Technologies A5750] and/or streptavidin-488 [Thermo Fisher S11223]), label synaptic puncta (anti-postsynaptic density [PSD-95, UC Davis NeuroMab 75-028], anti-Gephyrin [Synaptic Systems 147 111]), and stain for cholinergic starburst amacrine cells (anti-choline acetyltransferase [ChAT, Millipore AB144P]): blocking serum (1 day), primary antibody incubation (5 days), rinse 3× in PBS, secondary antibody (Jackson ImmunoResearch) incubation (1 day), rinse 3× in PBS. Retinas were mounted with a spacer in VECTASHIELD (Vector labs) and under a coverslip.

2.4.21 Imaging

Individual oDSGCs with known direction selectivity and their associated synaptic puncta were imaged on a confocal microscope (Leica SP8) using a ×40 objective (numerical aperture 1.3) at a resolution of 0.102 × 0.102 × 0.3 µm.

2.4.22 Image analysis

Confocal images were first median filtered in three dimensions (Fiji). Ganglion cell dendrites were reconstructed using the filament function in Imaris (Oxford Instruments). Convex polygons, dendritic branch numbers, and total dendritic length were obtained from the filaments. Excitatory PSD-95 and inhibitory gephyrin puncta were identified and quantified within the filament mask of the ganglion cell dendrites (ObjectFinder, https://lucadellasantina.github.io/ObjectFinder/; Della Santina et al., 2013).

2.4.23 Electrical properties of oDSGCs

The resting membrane potential, spike threshold, and input resistance of oDSGCs were all measured during whole-cell current-clamp recordings. Resting membrane potential was taken as the initial membrane voltage immediately after establishing intracellular access. Spike threshold and input resistance were both calculated by injecting a slow ramp of current. Spike threshold was the average voltage at which a cell initiated its first action potential in response to the ramp. Input resistance was calculated from the average slope of the I-V response below spike threshold. Both metrics were averaged over at least five repetitions of the ramp stimulus per cell. The membrane capacitance was measured during voltage-clamp recordings using the built-in capacitance calculator from the MultiClamp 700B Amplifier (Axon Instruments).

2.4.24 Parallel conductance model

We implemented a parallel conductance model in MATLAB to build the model oDSGC (adapted from Antoine et al., 2019). Excitatory (Gex) and inhibitory (Gin) conductances were calculated at each time point for each direction of stimulus motion using Ohm's law:

(3) $G = I/(Vhold - Erev)$

where I is the mean current trace recorded in voltage-clamp across both Superior and Inferior cells, $Vhold$ is the holding potential, and $Erev$ is the reversal potential for either excitation or inhibition. A liquid junction potential of 5 mV was subtracted from $Vhold$ and $Erev$. Because our model called for directionally untuned excitation, but the recorded excitatory conductances were slightly different for each direction of stimulus motion (likely due in part to space-clamp error), we used an identical excitatory conductance for all directions of stimulus motion that was equal to the maximum conductance at each time point across all recorded directions (space-clamp errors reduce empirically recorded excitatory currents in voltage-clamp mode). The excitatory conductance was then multiplied by a gain value to achieve a final time series for Gex.

Next, we used the equation

(4) $C\frac{dV}{dt} = Gex(Eex - Vm) + Gin(Ein - Vm) + Grest(Erest - Vm)$

to determine the membrane potential at each time point. C is the median capacitance of Superior and Inferior oDSGCs as measured during whole-cell recordings. $Grest$ is the reciprocal of the median input resistance, which we calculated by injecting a slow ramp of current in a subset of recorded cells and determining the average slope of the I-V response below spike threshold. $Erest$ is the median resting membrane potential. Vm is

calculated at each point in time by initializing it at $Erest$, and then determining each subsequent value using Euler's method and an integration time step of 1 ms. The peak change in this Vm value above $Erest$ was used to construct the Vm tuning curves in the version of the model without a spiking component.

In the version of the model with a spiking component, we again solved for Vm at every time point using Euler's method. In this case, however, whenever Vm surpassed the threshold potential, a 'spike' was counted and a 3 ms pause corresponding to the spike time and refractory period was initiated, after which Vm was reset to $Erest$ and the process continued. The threshold value was fixed such that the normalized area and direction selectivity index of the model oDSGC's spike tuning curve matched the median empirical values for these metrics (taken from cell-attached recordings) when the excitatory gain was set to 1.0. This resulted in a threshold value of –46.2 mV, which was 2.9 mV more negative than the median empirically recorded spike threshold.

Because resetting Vm to $Erest$ after each spike also changed the driving forces for excitation and inhibition – and therefore possibly the shape of resulting spike tuning curves – we also simulated spike responses by assuming that the number of spikes produced to a given stimulus was linearly proportional to the amount of time that Vm (calculated without a spiking mechanism in place) spent above spike threshold (data not shown). Results from this model were not substantively different than those from the model in which a refractory period was included and Vm was reset to $Erest$ after each spike.

This same model was used to test the contrast dependence of spike and Vm tuning curves. In this case, both the excitatory and each of the eight inhibitory conductance time series were multiplied by the gain value to calculate Gex and Gin, respectively.

2.4.25 Behavioral predictions from drifting bar stimulus

Predictions for OKR gain were calculated on the basis of the difference in median firing rates between Superior and Inferior oDSGC populations to the drifting bar stimulus. The preferred and null directions of each cell in our dataset were computed in response to high-contrast drifting bars. Gain predictions were made for high- and low-contrast (20% relative) stimuli moving in the superior and inferior directions (i.e., four total conditions) by (1) resampling from distributions of oDSGC responses for that condition 10,000 times, (2) computing the difference (i.e., 'delta') between the median preferred and null direction responses on each iteration for the appropriate cell types, and (3) using the median of these bootstrapped distributions of delta as an estimate of relative gain (**Figure 2.24**). The amplitudes of the predicted eye movements shown in **Figure 2.23C** reflect these predictions, while the sinusoidal trajectories are inferred from the stimulus motion.

Computing the preferred and null direction of each cell has the advantage of controlling for the fact that the observed preferred direction of individual oDSGCs can change based on retinotopic location when the retina is flat mounted. Assigning the preferred direction to a constant stimulus direction across cells (e.g., dorsal-to-ventral motion on the retina for Superior oDSGCs) did not change the behavioral predictions (data not shown).

2.2.26 Behavioral predictions from oscillating grating stimulus

oDSGC responses were measured in the cell-attached configuration in response to the same oscillating grating stimulus used in behavioral experiments. Two-photon targeting was used for all oscillating grating electrophysiology experiments. Stimulus oscillations were sinusoidal and had a period of 15 s and an amplitude of 20°. The intensity of the grating was also sinusoidal across space, and had a spatial frequency of 0.15 cycles/°. For the high-contrast stimulus, the mean light intensity of the grating evoked 3.8×10^3 S-cone photoisomerizations/s, the peak intensity evoked 7.6×10^3 S-cone photoisomerizations/s, and the trough intensity evoked 124 S-cone photoisomerizations/s. For the low-contrast stimulus, the 20% relative (Michelson) contrast stimulus used in behavior experiments failed to evoke consistent spiking in oDSGCs. That 20% relative contrast gratings evoked OKR behavior but not oDSGC spikes can likely be explained by the fact that absolute contrasts and adaptation states were not matched between behavior and electrophysiology. However, assuming monotonic nonlinearities, it is only necessary to match the *direction* (e.g., higher to lower) of contrast change to predict the corresponding *direction* of behavioral change across contrasts. Thus, in electrophysiology experiments, we used a version of the low-contrast oscillating grating stimulus that was 50% relative contrast compared to the high-contrast stimulus described above. The mean light intensity of this stimulus evoked 3.8×10^3 S-cone photoisomerizations/s, the peak intensity evoked 5.7×10^3 S-cone photoisomerizations/s, and the trough intensity evoked 1.9×10^3 S-cone photoisomerizations/s. For all stimuli, M-cone photoisomerizations were 74% those of S-cones. The initial positional phase of the grating was randomized between cells.

Linear behavioral predictions were made from the spike responses of Superior and Inferior oDSGCs to these oscillating stimuli (**Figure 2.25**). The following procedure was repeated separately for responses to high- and low-contrast gratings: first, the median spike rate of Superior and Inferior oDSGCs was computed every 5 ms over the course of a single 15 s oscillation cycle (**Figure 2.25 C and D**). A point-by-point subtraction was then performed (**Figure 2.25 E and F**). The difference between the median spike rates of Superior and Inferior oDSGCs served as a linear prediction of eye velocity at each point in time. Therefore, predictions of eye position were computed across time by integrating these differences:

(5) $p(t) = \int (Sup. - Inf.)dt$

where $p(t)$ is the vertical position of the eye at time t. The starting position of the eye was set to 0° (**Figure 2.25 G and H**).

2.2.27 Empirical nonlinearity

The relationship between linear predictions of OKR and measured eye velocities was estimated by finding the least-squares fit of a sigmoid function of the form

(6) $v(r) = v_{min} + \frac{v_{max} - v_{min}}{1 + 10^{(r_{50} - r)m}}$

where v_{min} is the minimum eye velocity, v_{max} is the maximum eye velocity, r_{50} is the difference in firing rate along the abscissa that corresponds to the inflection point, m controls the slope, and $v(r)$ is the expected eye velocity for a given firing rate difference, r. For the drifting bar stimulus (**Figure 2.23D**), the linear predictions and behavioral eye velocities for superior and inferior stimuli at high- and low-contrast, along with a fifth point at the origin (0, 0), were used to fit the curve. For the oscillating grating

stimulus (**Figure 2.23G**), the high-contrast instantaneous linear predictions and the time-matched average eye velocities during high-contrast stimuli were used to fit the curve.

2.2.28 Statistics

All metrics reported in the text refer to population mean ± SEM unless otherwise specified. Nonparametric hypothesis tests were used to compute significance values wherever possible. Mann–Whitney U tests were used for instances in which the test type is not specified. Wilcoxon signed-rank and Fisher's exact tests were used where specified in the text and/or figure legends. All tests were two-sided. R values are Spearman's rank correlation coefficients. Lines of best fits are least-squares linear regressions. Significance markings are as follows: not significant (N.S.) for $p \geq 0.05$, *$p < 0.05$, **$p < 0.01$, ***$p < 0.001$. All values can be found in the figures, figure legends, and 'Results' section. All statistical analyses were performed in MATLAB.

2.2.29 Tuning curve area

Tuning curve area was calculated by dividing the area under the curve of the linear tuning curve by 360°. For clarity, this metric is also referred to as the 'linear tuning curve area'.

2.2.30 Preferred direction

The preferred direction was calculated as the direction of the vector sum of spike responses to all eight stimulus directions of the drifting bar. Thus, the preferred direction was not necessarily equivalent to the single stimulus direction that evoked the largest response. The null direction was defined as 180° away from the preferred direction.

2.2.31 Normalized tuning curves

Normalized tuning curves were calculated by first determining the cell's preferred direction (see above), and then dividing the response in all eight stimulus directions to the response in that preferred direction. For cases in which the preferred direction did not match a stimulus direction that was specifically probed, the preferred direction response was estimated by a linear interpolation of the two neighboring probed directions. The area of the normalized tuning curve (abbreviated as the 'normalized area') was calculated by dividing the area under the curve of the linear normalized tuning curve by 360°. The area of the normalized tuning curve is always greater than 0, but has no upper bound – though it tended to fall below 1. Larger values indicate a wider tuning curve. Perfectly circular tuning curves take a value of 1.

2.2.32 Direction selectivity index

The direction selectivity index (DSI) was calculated as the magnitude of the vector sum divided by the scalar sum of responses to all eight stimulus directions. The direction selectivity index ranges between 0 and 1, with larger values indicating sharper tuning curves.

2.2.33 Von Mises fit

Tuning curves were fit to the Von Mises function by minimizing the sum of squared residuals. The Von Mises function is a circular analog of the Gaussian curve defined as

$$(7)\ f(x) = \frac{e^{\kappa \cos(x-\mu)}}{2\pi I_0(\kappa)}$$

where μ is the center of the curve, $1/\kappa$ controls the width of the curve, and I_0 is the modified Bessel function of the first kind, of order 0. A larger κ value indicates a sharper fit.

2.5 References

Al-Khindi T, Sherman MB, Kodama T, Gopal P, Pan Z, Kiraly JK, Zhang H, Goff LA, du Lac S, Kolodkin AL. 2022. The transcription factor Tbx5 regulates direction-selective retinal ganglion cell development and image stabilization. Current Biology 32:4286–4298.. DOI: https://doi.org/10.1016/j.cub.2022.07.064, PMID: 35998637

Amthor FR, Keyser KT, Dmitrieva NA. 2002. Effects of the destruction of starburst-cholinergic amacrine cells by the toxin AF64A on rabbit retinal directional selectivity. Visual Neuroscience 19:495–509. DOI: https://doi.org/10.1017/s0952523802194119, PMID: 12511082

Antoine MW, Langberg T, Schnepel P, Feldman DE. 2019. Increased excitation-inhibition ratio stabilizes synapse and circuit excitability in four autism mouse models. Neuron 101:648–661.. DOI: https://doi.org/10.1016/j.neuron.2018.12.026, PMID: 30679017

Barlow HB. 1953. Summation and inhibition in the frog's retina. The Journal of Physiology 119:69–88. DOI: https://doi.org/10.1113/jphysiol.1953.sp004829, PMID: 13035718

Briggman KL, Helmstaedter M, Denk W. 2011. Wiring specificity in the direction-selectivity circuit of the retina. Nature 471:183–188. DOI: https://doi.org/10.1038/nature09818, PMID: 21390125

Cahill H, Nathans J. 2008. The optokinetic reflex as a tool for quantitative analyses of nervous system function in mice: application to genetic and drug-induced variation.

PLOS ONE 3:e2055. DOI: https://doi.org/10.1371/journal.pone.0002055, PMID: 18446207

Carandini M, Heeger DJ. 2011. Normalization as a canonical neural computation. Nature Reviews. Neuroscience 13:51–62. DOI: https://doi.org/10.1038/nrn3136, PMID: 22108672

Care RA, Kastner DB, De la Huerta I, Pan S, Khoche A, Della Santina L, Gamlin C, Santo Tomas C, Ngo J, Chen A, Kuo Y-M, Ou Y, Dunn FA. 2019. Partial cone loss triggers synapse-specific remodeling and spatial receptive field rearrangements in a mature retinal circuit. Cell Reports 27:2171–2183. DOI: https://doi.org/10.1016/j.celrep.2019.04.065, PMID: 31091454

Care RA, Anastassov IA, Kastner DB, Kuo YM, Della Santina L, Dunn FA. 2020. Mature retina compensates functionally for partial loss of rod photoreceptors. Cell Reports 31:107730. DOI: https://doi.org/10.1016/j.celrep.2020.107730, PMID: 32521255

Collewijn H. 1969. Optokinetic eye movements in the rabbit: input-output relations. Vision Research 9:117–132. DOI: https://doi.org/10.1016/0042-6989(69)90035-2, PMID: 5778032

Cook JE, Podugolnikova TA. 2001. Evidence for spatial regularity among retinal ganglion cells that project to the accessory optic system in a frog, a reptile, a bird, and a mammal. Visual Neuroscience 18:289–297. DOI:https://doi.org/10.1017/s0952523801182131, PMID: 11417803

Dacey DM, Crook JD, Packer OS. 2014. Distinct synaptic mechanisms create parallel S-ON and S-OFF color opponent pathways in the primate retina. Visual

Neuroscience 31:139–151. DOI: https://doi.org/10.1017/S0952523813000230, PMID: 23895762

Dann JF, Buhl EH. 1987. Retinal ganglion cells projecting to the accessory optic system in the rat. The Journal of Comparative Neurology 262:141–158. DOI: https://doi.org/10.1002/cne.902620111, PMID: 3624547

Della Santina L, Yu AK, Harris SC, Soliño M, Garcia Ruiz T, Most J, Kuo YM, Dunn FA, Ou Y. 2021. Disassembly and rewiring of a mature converging excitatory circuit following injury. Cell Reports 36:109463. DOI: https://doi.org/10.1016/j.celrep.2021.109463, PMID: 34348156

De Monasterio FM, Gouras P. 1975. Functional properties of ganglion cells of the rhesus monkey retina. The Journal of Physiology 251:167–195. DOI: https://doi.org/10.1113/jphysiol.1975.sp011086, PMID: 810576

Dehmelt FA, Meier R, Hinz J, Yoshimatsu T, Simacek CA, Huang R, Wang K, Baden T, Arrenberg AB. 2021. Spherical arena reveals optokinetic response tuning to stimulus location, size, and frequency across entire visual field of larval zebrafish. eLife 10:e63355. DOI: https://doi.org/10.7554/eLife.63355, PMID: 34100720

Della Santina L, Inman DM, Lupien CB, Horner PJ, Wong ROL. 2013. Differential progression of structural and functional alterations in distinct retinal ganglion cell types in a mouse model of glaucoma. The Journal of Neuroscience 33:17444–17457. DOI: https://doi.org/10.1523/JNEUROSCI.5461-12.2013, PMID: 24174678

Denman DJ, Siegle JH, Koch C, Reid RC, Blanche TJ. 2017. Spatial organization of chromatic pathways in the mouse dorsal lateral geniculate nucleus. The Journal of

Neuroscience 37:1102–1116. DOI: https://doi.org/10.1523/JNEUROSCI.1742-16.2016, PMID: 27986926

Dhande OS, Estevez ME, Quattrochi LE, El-Danaf RN, Nguyen PL, Berson DM, Huberman AD. 2013. Genetic dissection of retinal inputs to brainstem nuclei controlling image stabilization. The Journal of Neuroscience 33:17797–17813. DOI: https://doi.org/10.1523/JNEUROSCI.2778-13.2013, PMID: 24198370

Dhande OS, Stafford BK, Lim JHA, Huberman AD. 2015. Contributions of retinal ganglion cells to subcortical visual processing and behaviors. Annual Review of Vision Science 1:291–328. DOI: https://doi.org/10.1146/annurev-vision-082114-035502, PMID: 28532372

Ding H, Smith RG, Poleg-Polsky A, Diamond JS, Briggman KL. 2016. Species-specific wiring for direction selectivity in the mammalian retina. Nature 535:105–110. DOI: https://doi.org/10.1038/nature18609, PMID:27350241

Donaghy M. 1980. The contrast sensitivity, spatial resolution and velocity tuning of the cat's optokinetic reflex. The Journal of Physiology 300:353–365. DOI: https://doi.org/10.1113/jphysiol.1980.sp013166, PMID: 7381791

Evinger C, Fuchs AF. 1978. Saccadic, smooth pursuit, and optokinetic eye movements of the trained cat. The Journal of Physiology 285:209–229. DOI: https://doi.org/10.1113/jphysiol.1978.sp012568, PMID: 745071

Field GD, Greschner M, Gauthier JL, Rangel C, Shlens J, Sher A, Marshak DW, Litke AM, Chichilnisky EJ. 2009. High-Sensitivity rod photoreceptor input to the blue-yellow

color opponent pathway in macaque retina. Nature Neuroscience 12:1159–1164. DOI: https://doi.org/10.1038/nn.2353, PMID: 19668201

Fried SI, Münch TA, Werblin FS. 2002. Mechanisms and circuitry underlying directional selectivity in the retina. Nature 420:411–414. DOI: https://doi.org/10.1038/nature01179, PMID: 12459782

Giolli RA, Peterson GM, Ribak CE, McDonald HM, Blanks RH, Fallon JH. 1985. GABAergic neurons comprise a major cell type in rodent visual relay nuclei: an immunocytochemical study of pretectal and accessory optic nuclei. Experimental Brain Research 61:194–203. DOI: https://doi.org/10.1007/BF00235635, PMID: 3002835

Giolli RA, Blanks RHI, Lui F. 2006. The accessory optic system: basic organization with an update on connectivity, neurochemistry, and function. Progress in Brain Research 151:407–440. DOI: https://doi.org/10.1016/S0079-6123(05)51013-6, PMID: 16221596

Grasse KL, Cynader MS. 1982. Electrophysiology of medial terminal nucleus of accessory optic system in the cat. Journal of Neurophysiology 48:490–504. DOI: https://doi.org/10.1152/jn.1982.48.2.490, PMID: 7119859

Grasse KL, Cynader MS. 1988. The effect of visual cortex lesions on vertical optokinetic nystagmus in the cat. Brain Research 455:385–389. DOI: https://doi.org/10.1016/0006-8993(88)90100-x, PMID: 3401789

Gravot CM, Knorr AG, Glasauer S, Straka H. 2017. It's not all black and white: visual scene parameters influence optokinetic reflex performance in Xenopus laevis

tadpoles. The Journal of Experimental Biology 220:4213–4224. DOI: https://doi.org/10.1242/jeb.167700, PMID: 29141881

Hainline L, Lemerise E, Abramov I, Turkel J. 1984. Orientational asymmetries in small-field optokinetic nystagmus in human infants. Behavioural Brain Research 13:217–230. DOI: https://doi.org/10.1016/0166-4328(84)90164-5, PMID: 6508900

Hartline HK, Wagner HG, Macnichol EF. 1952. The peripheral origin of nervous activity in the visual system. Cold Spring Harbor Symposia on Quantitative Biology 17:125–141. DOI: https://doi.org/10.1101/sqb.1952.017.01.013, PMID: 13049160

Hoffmann KP, Fischer WH. 2001. Directional effect of inactivation of the nucleus of the optic tract on optokinetic nystagmus in the cat. Vision Research 41:3389–3398. DOI: https://doi.org/10.1016/s0042-6989(01)00184-5,PMID: 11718781

Holmgren CD, Stahr P, Wallace DJ, Voit KM, Matheson EJ, Sawinski J, Bassetto G, Kerr JN. 2021. Visual pursuit behavior in mice maintains the pursued prey on the retinal region with least optic flow. eLife 10:e70838. DOI:https://doi.org/10.7554/eLife.70838, PMID: 34698633

Kay JN, De la Huerta I, Kim I-J, Zhang Y, Yamagata M, Chu MW, Meister M, Sanes JR. 2011. Retinal ganglion cells with distinct directional preferences differ in molecular identity, structure, and central projections. The Journal of Neuroscience 31:7753–7762. DOI: https://doi.org/10.1523/JNEUROSCI.0907-11.2011, PMID:21613488

Kittila CA, Massey SC. 1997. Pharmacology of directionally selective ganglion cells in the rabbit retina. Journal of Neurophysiology 77:675–689. DOI: https://doi.org/10.1152/jn.1997.77.2.675, PMID: 9065840

Knapp CM, Proudlock FA, Gottlob I. 2013. OKN asymmetry in human subjects: A literature review. Strabismus 21:37–49. DOI: https://doi.org/10.3109/09273972.2012.762532, PMID: 23477776

Knorr AG, Gravot CM, Glasauer S, Straka H. 2021. Image motion with color contrast suffices to elicit an optokinetic reflex in Xenopus laevis tadpoles. Scientific Reports 11:8445. DOI: https://doi.org/10.1038/s41598-021-87835-2, PMID: 33875722

Koulen P, Fletcher EL, Craven SE, Bredt DS, Wässle H. 1998. Immunocytochemical localization of the postsynaptic density protein PSD-95 in the mammalian retina. The Journal of Neuroscience 18:10136–10149. DOI: https://doi.org/10.1523/JNEUROSCI.18-23-10136.1998, PMID: 9822767

Kuffler SW. 1953. Discharge patterns and functional organization of mammalian retina. Journal of Neurophysiology 16:37–68. DOI: https://doi.org/10.1152/jn.1953.16.1.37, PMID: 13035466

Lee S, Chen L, Chen M, Ye M, Seal RP, Zhou ZJ. 2014. An unconventional glutamatergic circuit in the retina formed by vglut3 amacrine cells. Neuron 84:708–715. DOI: https://doi.org/10.1016/j.neuron.2014.10.021, PMID: 25456497

Leguire LE, Zaff BS, Freeman S, Rogers GL, Bremer DL, Wali N. 1991. Contrast sensitivity of optokinetic nystagmus. Vision Research 31:89–97. DOI: https://doi.org/10.1016/0042-6989(91)90076-h, PMID: 2006557

Lilley BN, Sabbah S, Hunyara JL, Gribble KD, Al-Khindi T, Xiong J, Wu Z, Berson DM, Kolodkin AL. 2019. Genetic access to neurons in the accessory optic system reveals a role for sema6a in midbrain circuitry mediating motion perception. The

Journal of Comparative Neurology 527:282–296. DOI: https://doi.org/10.1002/cne.24507, PMID: 30076594

Liu B-H, Huberman AD, Scanziani M. 2016. Cortico-fugal output from visual cortex promotes plasticity of innate motor behaviour. Nature 538:383–387. DOI: https://doi.org/10.1038/nature19818, PMID: 27732573

Mani A, Yang X, Zhao T, Leyrer ML, Schreck D, Berson DM. 2021. A Retinal Circuit That Vetoes Optokinetic Responses to Fast Visual Motion. bioRxiv. DOI: https://doi.org/10.1101/2021.10.31.466688

Martin H. 1965. Osmotropotaxis in the honey-bee. Nature 208:59–63. DOI: https://doi.org/10.1038/208059a0

Masseck OA, Hoffmann KP. 2009. Comparative neurobiology of the optokinetic reflex. Annals of the New York Academy of Sciences 1164:430–439. DOI: https://doi.org/10.1111/j.1749-6632.2009.03854.x, PMID: 19645943

Matsumoto A, Briggman KL, Yonehara K. 2019. Spatiotemporally asymmetric excitation supports mammalian retinal motion sensitivity. Current Biology 29:3277–3288.. DOI: https://doi.org/10.1016/j.cub.2019.08.048, PMID: 31564498

Matsumoto A, Agbariah W, Nolte SS, Andrawos R, Levi H, Sabbah S, Yonehara K. 2021. Direction selectivity in retinal bipolar cell axon terminals. Neuron 109:2928–2942.. DOI: https://doi.org/10.1016/j.neuron.2021.07.008, PMID: 34390651

Mauss AS, Vlasits A, Borst A, Feller M. 2017. Visual circuits for direction selectivity. Annual Review of Neuroscience 40:211–230. DOI: https://doi.org/10.1146/annurev-neuro-072116-031335, PMID: 28418757

Middlebrooks JC, Green DM. 1991. Sound localization by human listeners. Annual Review of Psychology 42:135–159. DOI: https://doi.org/10.1146/annurev.ps.42.020191.001031, PMID: 2018391

Mowrer OH. 1936. A comparison of the reaction mechanisms mediating optokinetic nystagmus in human beings and in pigeons. Psychological Monographs 47:294–305. DOI: https://doi.org/10.1037/h0093419

Murasugi CM, Howard IP. 1989. Up-down asymmetry in human vertical optokinetic nystagmus and afternystagmus: contributions of the central and peripheral retinae. Experimental Brain Research 77:183–192.DOI: https://doi.org/10.1007/BF00250580, PMID: 2792261

Natal CL, Britto LRG. 1988. The rat accessory optic system: effects of cortical lesions on the directional selectivity of units within the medial terminal nucleus. Neuroscience Letters 91:154–159. DOI: https://doi.org/10.1016/0304-3940(88)90760-4, PMID: 3185957

Oesch N, Euler T, Taylor WR. 2005. Direction-selective dendritic action potentials in rabbit retina. Neuron 47:739–750. DOI: https://doi.org/10.1016/j.neuron.2005.06.036, PMID: 16129402

Osterhout JA, Stafford BK, Nguyen PL, Yoshihara Y, Huberman AD. 2015. Contactin-4 mediates axon-target specificity and functional development of the accessory optic

system. Neuron 86:985–999. DOI: https://doi.org/10.1016/j.neuron.2015.04.005, PMID: 25959733

Oyster CW, Barlow HB. 1967. Direction-selective units in rabbit retina: distribution of preferred directions. Science 155:841–842. DOI: https://doi.org/10.1126/science.155.3764.841, PMID: 6019094

Oyster CW. 1968. The analysis of image motion by the rabbit retina. The Journal of Physiology 199:613–635. DOI: https://doi.org/10.1113/jphysiol.1968.sp008671, PMID: 5710424

Oyster CW, Takahashi E, Collewijn H. 1972. Direction-selective retinal ganglion cells and control of optokinetic nystagmus in the rabbit. Vision Research 12:183–193. DOI: https://doi.org/10.1016/0042-6989(72)90110-1, PMID: 5033683

Pak MW, Giolli RA, Pinto LH, Mangini NJ, Gregory KM, Vanable JW. 1987. Retinopretectal and accessory optic projections of normal mice and the OKN-defective mutant mice beige, beige-J, and pearl. The Journal of Comparative Neurology 258:435–446. DOI: https://doi.org/10.1002/cne.902580311, PMID: 3584547

Peirce JW. 2007. PsychoPy -- psychophysics software in python. Journal of Neuroscience Methods 162:8–13. DOI: https://doi.org/10.1016/j.jneumeth.2006.11.017, PMID: 17254636

Percival KA, Venkataramani S, Smith RG, Taylor WR. 2019. Directional excitatory input to direction-selective ganglion cells in the rabbit retina. The Journal of Comparative

Neurology 527:270–281. DOI: https://doi.org/10.1002/cne.24207, PMID: 28295340

Poleg-Polsky A, Diamond JS. 2011. Imperfect space clamp permits electrotonic interactions between inhibitory and excitatory synaptic conductances, distorting voltage clamp recordings. PLOS ONE 6:e19463. DOI: https://doi.org/10.1371/journal.pone.0019463, PMID: 21559357

Poleg-Polsky A, Diamond JS. 2016a. Nmda receptors multiplicatively scale visual signals and enhance directional motion discrimination in retinal ganglion cells. Neuron 89:1277–1290. DOI: https://doi.org/10.1016/j.neuron.2016.02.013, PMID: 26948896

Poleg-Polsky A, Diamond JS. 2016b. Retinal circuitry balances contrast tuning of excitation and inhibition to enable reliable computation of direction selectivity. The Journal of Neuroscience 36:5861–5876. DOI: https://doi.org/10.1523/JNEUROSCI.4013-15.2016, PMID: 27225774

Remtulla S, Hallett PE. 1985. A schematic eye for the mouse, and comparisons with the rat. Vision Research 25:21–31. DOI: https://doi.org/10.1016/0042-6989(85)90076-8, PMID: 3984214

Rodieck RW. 1991. The density recovery profile: a method for the analysis of points in the plane applicable to retinal studies. Visual Neuroscience 6:95–111. DOI: https://doi.org/10.1017/s095252380001049x, PMID:2049333

Ruff T, Peters C, Matsumoto A, Ihle SJ, Morales PA, Gaitanos L, Yonehara K, Del Toro D, Klein R. 2021. FLRT3 marks direction-selective retinal ganglion cells that project

to the medial terminal nucleus. Frontiers in Molecular Neuroscience 14:790466. DOI: https://doi.org/10.3389/fnmol.2021.790466, PMID: 34955746

Sabbah S, Gemmer JA, Bhatia-Lin A, Manoff G, Castro G, Siegel JK, Jeffery N, Berson DM. 2017. A retinal code for motion along the gravitational and body axes. Nature 546:492–497. DOI: https://doi.org/10.1038/nature22818, PMID: 28607486

Sassoè-Pognetto M, Kirsch J, Grünert U, Greferath U, Fritschy JM, Möhler H, Betz H, Wässle H. 1995. Colocalization of gephyrin and GABAA-receptor subunits in the rat retina. The Journal of Comparative Neurology 357:1–14. DOI: https://doi.org/10.1002/cne.903570102, PMID: 7673460

Sassoè-Pognetto M, Wässle H. 1997. Synaptogenesis in the rat retina: subcellular localization of glycine receptors, GABA (a) receptors, and the anchoring protein gephyrin. The Journal of Comparative Neurology 381:158–174. DOI: https://doi.org/10.1002/(sici)1096-9861(19970505)381:2<158::aid-cne4>3.0.co;2-2, PMID: 9130666

Schwenk K. 1994. Why snakes have forked tongues. Science 263:1573–1577. DOI: https://doi.org/10.1126/science.263.5153.1573, PMID: 17744784

Sethuramanujam S, McLaughlin AJ, deRosenroll G, Hoggarth A, Schwab DJ, Awatramani GB. 2016. A central role for mixed acetylcholine/GABA transmission in direction coding in the retina. Neuron 90:1243–1256. DOI: https://doi.org/10.1016/j.neuron.2016.04.041, PMID: 27238865

Sethuramanujam S, Yao X, deRosenroll G, Briggman KL, Field GD, Awatramani GB. 2017. “Silent” NMDA synapses enhance motion sensitivity in a mature retinal

circuit. Neuron 96:1099–1111. DOI: https://doi.org/10.1016/j.neuron.2017.09.058, PMID: 29107522

Shimizu N, Tabata H, Wada Y, Sugita Y, Yamanaka T, Hosoi H, Kawano K. 2010. Distribution of optokinetic sensitivity across the retina of mice in relation to eye orientation. Neuroscience 168:200–208. DOI: https://doi.org/10.1016/j.neuroscience.2010.03.025, PMID: 20303393

Simpson JI, Soodak RE, Hess R. 1979. The accessory optic system and its relation to the vestibulocerebellum. Progress in Brain Research 50:715–724. DOI: https://doi.org/10.1016/S0079-6123(08)60868-7, PMID: 551466

Simpson JI. 1984. The accessory optic system. Annual Review of Neuroscience 7:13–41. DOI: https://doi.org/10.1146/annurev.ne.07.030184.000305, PMID: 6370078

Sivyer B, Williams SR. 2013. Direction selectivity is computed by active dendritic integration in retinal ganglion cells. Nature Neuroscience 16:1848–1856. DOI: https://doi.org/10.1038/nn.3565, PMID: 24162650

Sivyer B, Tomlinson A, Taylor WR. 2019. Simulated saccadic stimuli suppress ON-type direction-selective retinal ganglion cells via glycinergic inhibition. The Journal of Neuroscience 39:4312–4322. DOI: https://doi.org/10.1523/JNEUROSCI.3066-18.2019, PMID: 30926751

Soodak RE, Simpson JI. 1988. The accessory optic system of rabbit. I. basic visual response properties. Journal of Neurophysiology 60:2037–2054. DOI: https://doi.org/10.1152/jn.1988.60.6.2037, PMID: 3236060

Stahl JS, van Alphen AM, De Zeeuw CI. 2000. A comparison of video and magnetic search coil recordings of mouse eye movements. Journal of Neuroscience Methods 99:101–110. DOI: https://doi.org/10.1016/s0165-0270(00)00218-1, PMID: 10936649

Stahl JS. 2004. Eye movements of the murine P/Q calcium channel mutant rocker, and the impact of aging. Journal of Neurophysiology 91:2066–2078. DOI: https://doi.org/10.1152/jn.01068.2003, PMID: 14724264

Summers MT, Feller MB. 2022. Distinct inhibitory pathways control velocity and directional tuning in the mouse retina. Current Biology 32:2130–2143.. DOI: https://doi.org/10.1016/j.cub.2022.03.054, PMID: 35395192

Sun LO, Brady CM, Cahill H, Al-Khindi T, Sakuta H, Dhande OS, Noda M, Huberman AD, Nathans J, Kolodkin AL. 2015. Functional assembly of accessory optic system circuitry critical for compensatory eye movements. Neuron 86:971–984. DOI: https://doi.org/10.1016/j.neuron.2015.03.064, PMID: 25959730

Suver MP, Matheson AMM, Sarkar S, Damiata M, Schoppik D, Nagel KI. 2019. Encoding of wind direction by central neurons in Drosophila. Neuron 102:828–842.. DOI: https://doi.org/10.1016/j.neuron.2019.03.012, PMID: 30948249

Takahashi M, Igarashi M. 1977. Comparison of vertical and horizontal optokinetic nystagmus in the squirrel monkey. ORL; Journal for Oto-Rhino-Laryngology and Its Related Specialties 39:321–329. DOI: https://doi.org/10.1159/000275374, PMID: 97609

Takahashi M, Sakurai S, Kanzaki J. 1978. Horizontal and vertical optokinetic nystagmus in man. ORL; Journal for Oto-Rhino-Laryngology and Its Related Specialties 40:43–52. DOI: https://doi.org/10.1159/000275385, PMID: 567774

Tauber ES, Atkin A. 1968. Optomotor responses to monocular stimulation: relation to visual system organization. Science 160:1365–1367. DOI: https://doi.org/10.1126/science.160.3834.1365, PMID: 5651899

van den Berg AV, Collewijn H. 1988. Directional asymmetries of human optokinetic nystagmus. Experimental Brain Research 70:597–604. DOI: https://doi.org/10.1007/BF00247608, PMID: 3384058

van der Togt C, van der Want J, Schmidt M. 1993. Segregation of direction selective neurons and synaptic organization of inhibitory intranuclear connections in the medial terminal nucleus of the rat: an electrophysiological and immunoelectron microscopical study. The Journal of Comparative Neurology 338:175–192. DOI: https://doi.org/10.1002/cne.903380204, PMID: 8308166

Vaney DI, Sivyer B, Taylor WR. 2012. Direction selectivity in the retina: symmetry and asymmetry in structure and function. Nature Reviews. Neuroscience 13:194–208. DOI: https://doi.org/10.1038/nrn3165, PMID: 22314444

Wallman J, Velez J. 1985. Directional asymmetries of optokinetic nystagmus: developmental changes and relation to the accessory optic system and to the vestibular system. The Journal of Neuroscience 5:317–329. DOI: https://doi.org/10.1523/JNEUROSCI.05-02-00317.1985, PMID: 3871841

Wei W, Hamby AM, Zhou K, Feller MB. 2011. Development of asymmetric inhibition underlying direction selectivity in the retina. Nature 469:402–406. DOI: https://doi.org/10.1038/nature09600, PMID: 21131947

Wei W. 2018. Neural mechanisms of motion processing in the mammalian retina. Annual Review of Vision Science 4:165–192. DOI: https://doi.org/10.1146/annurev-vision-091517-034048, PMID: 30095374

Wood CC, Spear PD, Braun JJ. 1973. Direction-Specific deficits in horizontal optokinetic nystagmus following removal of visual cortex in the cat. Brain Research 60:231–237. DOI: https://doi.org/10.1016/0006-8993(73) 90862-7, PMID: 4744764

Yonehara K, Shintani T, Suzuki R, Sakuta H, Takeuchi Y, Nakamura-Yonehara K, Noda M. 2008. Expression of SPIG1 reveals development of a retinal ganglion cell subtype projecting to the medial terminal nucleus in the mouse. PLOS ONE 3:e01533. DOI: https://doi.org/10.1371/journal.pone.0001533

Yonehara K, Ishikane H, Sakuta H, Shintani T, Nakamura-Yonehara K, Kamiji NL, Usui S, Noda M. 2009. Identification of retinal ganglion cells and their projections involved in central transmission of information about upward and downward image motion. PLOS ONE 4:e04320. DOI: https://doi.org/10.1371/journal.pone.0004320

Yonehara K, Balint K, Noda M, Nagel G, Bamberg E, Roska B. 2011. Spatially asymmetric reorganization of inhibition establishes a motion-sensitive circuit. Nature 469:407–410. DOI: https://doi.org/10.1038/nature09711, PMID: 21170022

Yonehara K, Farrow K, Ghanem A, Hillier D, Balint K, Teixeira M, Jüttner J, Noda M, Neve RL, Conzelmann K-K, Roska B. 2013. The first stage of cardinal direction

selectivity is localized to the dendrites of retinal ganglion cells. Neuron 79:1078–1085. DOI: https://doi.org/10.1016/j.neuron.2013.08.005, PMID: 23973208

Yonehara K, Fiscella M, Drinnenberg A, Esposti F, Trenholm S, Krol J, Franke F, Scherf BG, Kusnyerik A, Müller J, Szabo A, Jüttner J, Cordoba F, Reddy AP, Németh J, Nagy ZZ, Munier F, Hierlemann A, Roska B. 2016. Congenital nystagmus gene FRMD7 is necessary for establishing a neuronal circuit asymmetry for direction selectivity. Neuron 89:177–193. DOI: https://doi.org/10.1016/j.neuron.2015.11.032, PMID: 26711119

Yoshida K, Watanabe D, Ishikane H, Tachibana M, Pastan I, Nakanishi S. 2001. A key role of starburst amacrine cells in originating retinal directional selectivity and optokinetic eye movement. Neuron 30:771–780. DOI: https://doi.org/10.1016/s0896-6273(01)00316-6, PMID: 11430810

Zeil J, Nalbach G, Nalbach HO. 1989. Spatial vision in a flat world: optical and neural adaptations in arthropods.

Singh RN, Strausfeld NJ (Eds). Neurobiology of Sensory Systems. Springer US. p. 123–137. DOI: https://doi.org/10.1007/978-1-4899-2519-0_10

Zoccolan D, Graham BJ, Cox DD. 2010. A self-calibrating, camera-based eye tracker for the recording of rodent eye movements. Frontiers in Neuroscience 4:193. DOI: https://doi.org/10.3389/fnins.2010.00193, PMID: 21152259

CHAPTER 3. FUTURE DIRECTIONS: THE OPTOKINETIC REFLEX AS A BIOMARKER OF DISEASE

3.1 Introduction

A foundational principle in the study of information systems is that well-designed encoding and decoding schemes can preserve signal transmission in the face of arbitrary amounts of noise (Shannon, 1948). In biology, this principle is exemplified by the resilience of certain systems to degenerative processes that increase disorder (Care et al., 2020; Geller et al., 1992; Naoi and Maruyama, 1999; Santina et al., 2021). For instance, subjective visual acuity in certain forms of progressive vision loss remains unaffected until more than half of cone photoreceptors are compromised (Ratnam et al., 2013). This phenomenon suggests a remarkable capacity of the human visual system to cope with signal corruption and data loss. However, it also presents a critical challenge to treatment by obscuring symptoms and delaying diagnosis until a significant, and potentially irreversible, degree of degeneration has occurred. Thus, identifying which neural circuits, if any, exhibit early and readily detectable vulnerabilities to degeneration is an important step toward creating high-sensitivity diagnostics and understanding disease.

Among the properties that may increase the likelihood of a circuit's vulnerability to information loss are 1) enhanced sensitivity to small input changes, and 2) functional isolation from computational resources that might otherwise compensate for degeneration. While photoreceptor loss reduces the amount of information captured by the cone array, for example, retinal circuits associated with visual acuity respond

sublinearly (Care et al., 2019; Lee et al., 2022), and downstream cortical resources can be drawn on to recover lost information through inference (Kiebel, 2009). In contrast, a pathway that is already sensitive to subtle input changes, and which lacks the resources to compensate, may be primed to reflect early degeneration.

In Chapter 2, I showed how a particular visual circuit meets these criteria (Harris and Dunn, 2023). The biophysical properties of ON direction selective ganglion cells (oDSGCs) in the retina confer superlinear responses to small input changes (**Figures 2.15-2.19, 2.20-2.22**). Further, oDSGCs do not participate in conventional visual pathways. Instead, they are functionally and physically isolated as the sole visual input to the accessory optic system (AOS) in the brainstem. Here, their spikes serve the specific purpose of driving image stabilizing eye movements known as the optokinetic reflex (OKR) through only a handful of synapses (Dhande et al., 2015; Giolli et al., 2006; Simpson, 1984) and with near linearity (**Figure 2.23-2.25**). These unique properties suggest that oDSGCs, the AOS, and OKR may be especially sensitive to reflect degeneration.

In this chapter, I present preliminary data in support of this hypothesis. Previous work demonstrated that OKR changes in proportion with significant (>50%) cone photoreceptor ablation in mice (Shen et al., 2020). The data presented here show that this result extends to even mild cone loss; both OKR gain and oDSGC spiking reflect photoreceptor loss that is below the level of subjective detectability in humans. The chapter concludes by expanding on the possibility of using OKR in diagnostic contexts and discussing future work that must be done to make these translational aspirations a reality.

3.2 OKR and oDSGCs reflect mild cone loss in mice

OKR gain (the ratio of eye velocity to stimulus velocity) changes with the signal to noise ratio of stimuli, including following contrast manipulations and visual field loss (Dakin and Turnbull, 2016; Donaghy, 1980; Doustkouhi et al., 2020; Harris and Dunn, 2023; Knorr et al., 2021; Leguire et al., 1991; Taore et al., 2022). Thus, we hypothesized that OKR may also reflect modest degeneration of cone photoreceptors. To test this, we induced graded degeneration of M-opsin expressing cones via intramuscular injection of diphtheria toxin (DT) in adult, transgenic mice expressing a floxed copy of the diphtheria toxin receptor gene and Cre-recombinase under the *OPN1MW* promoter ("DTR mice", Care et al., 2019). This approach resulted in mice with approximately 30% cone loss relative to control animals (**Figure 3.1A,** controls consisted of several genotypes, including wildtype animals, $DTR^{-/-}$ littermates, and vehicle injected DTR+ mice). Vertical OKR gain was then measured in head-fixed DTR and control mice in response to full-field, 405 nm oscillating sinusoidal gratings (at least two weeks after DT injections. For methodological details on behavior and eye tracking, see Chapter 2.4.2 – 2.4.5; Harris and Dunn, 2023; Kiraly et al., 2023). Vertical OKR gain in DTR mice was on average 20% lower than in control animals (**Figure 3.1B**). This suggests a sensitive relationship between cone density and OKR gain at degrees of cone ablation that are more mild than existing diagnostic thresholds in humans (Ratnam et al., 2013). However, considering that the DT manipulation ablates only M-opsin expressing cones, and the 405 nm stimulus used to evoke OKR activates M-opsin 60% as much as it activates S-opsin (see Chapter 2.4.3), the relationship between the effective change in retinal drive (i.e., the total photoisomerization rate) and OKR gain may in fact be superlinear.

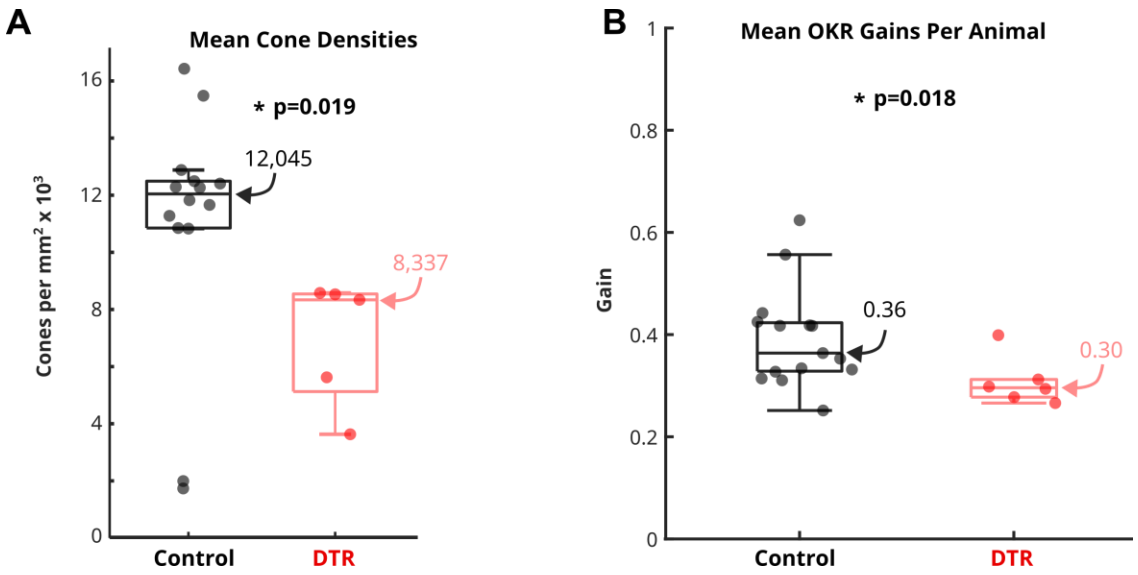

Figure 3.1 Optokinetic reflex (OKR) gain in control and cone ablated mice. (**A**) Quantification of cone photoreceptor density in control (black, n=14) and cone ablated (DTR, red, n=5) mice. Each dot shows the mean cone density from a single animal. Values were averaged across 12 regions of interest over the left retina. Data was collected following the methods described in Care et al., 2019. On average, DTR animals have 30.8% cone loss relative to control animals. (**B**) Vertical OKR gain for control (black, n=14) and DTR (red, n=6) mice. Stimulus parameters and recording methods were identical to those described for the high contrast oscillating grating experiments in Chapter 2. On average, vertical OKR gain is 20% lower in DTR animals than in control animals. For both panels, numbers with arrows identify the median value for each group. Boxes show IQR and whiskers extend to smallest value within 1.5xIQR. p-values are from rank sum tests.

The true effect of the DT injection on net photoisomerization rates is difficult to estimate because most mouse cones co-express M- and S-opsin (Nadal-Nicolás et al., 2020). However, a simplified approximation which assumes equal amounts of M- and S-opsin across the retina suggests that, during the OKR behavior, total photoisomerization rates may only be 12% lower in DTR mice compared to controls. The importance of understanding the precise effect of the DT manipulation on photoisomerization rates *in vivo* underscores the need for more sophisticated analysis techniques. Nonetheless, OKR gain appears to be a sensitive measure of mild cone photoreceptor loss in mice.

We next explored the effect of mild cone loss on oDSGC physiology. We selectively labeled MTN-projecting oDSGCs in DTR and control mice by performing a central injection of a retrograde tracer into MTN. We then targeted Superior and Inferior oDSGCs for electrophysiological recordings using a two-photon microscope (see Chapter 2, **Figures 2.4, 2.5, 2.7**). oDSGCs from DTR mice produced fewer total spikes than those from control animals in response to a bright drifting bar of light (10 deg/s, 8 directions, 100 x 1000 um, 405 nm; **Figure 3.2A**). This result suggests that the spiking activity of oDSGCs is sensitive to mild cone loss, and that the behavioral findings in **Figure 3.1B** are the consequence of this. Further analysis is needed to confirm if a linear subtraction of oDSGC activity is sufficient to explain OKR gain in DTR mice, as it is in wildtype animals. oDSGCs from DTR mice also had sharper tuning curves than those from control animals (**Figure 3.2B**). This finding may reflect superlinear changes in spiking activity associated with nonlinearities at the spike threshold. Thus, these preliminary results indicate that the sensitivity of oDSGCs to modest, stimulus-derived input changes under

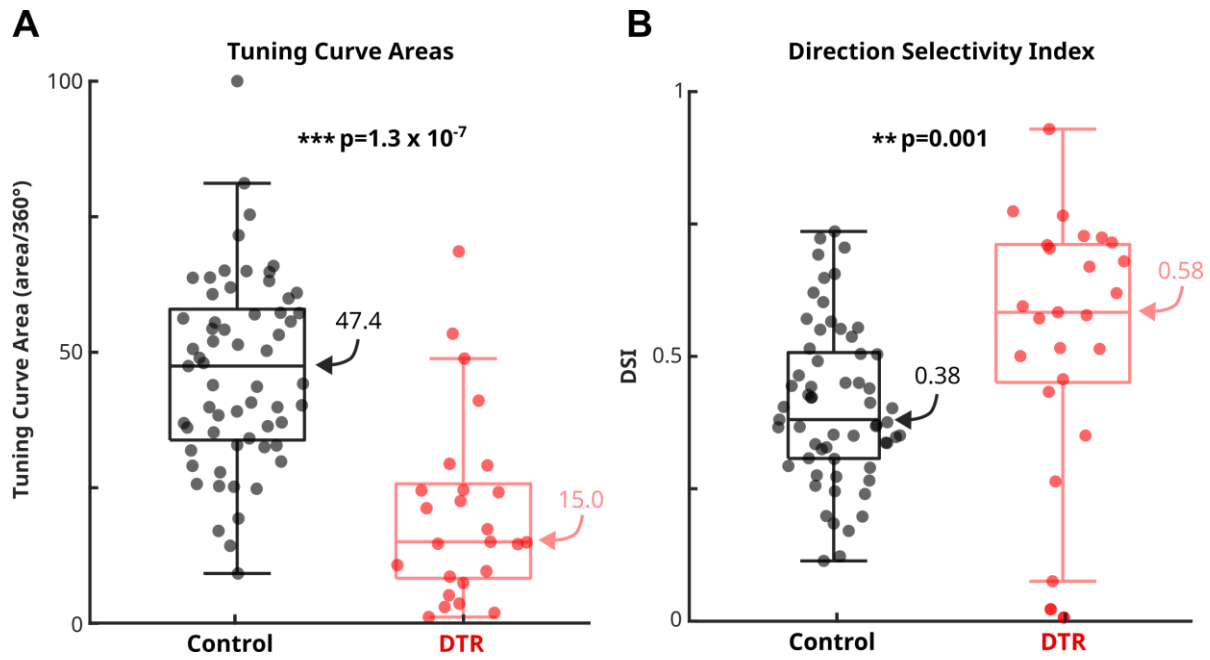

Figure 3.2 Spike responses from ON direction selective retinal ganglion cells (oDSGCs) in control and cone ablated mice. The spike tuning curves of two-photon targeted oDSGCs were recorded in the cell-attached configuration. Stimulus parameters and recording methodologies were identical to those described for the high-contrast drifting bar electrophysiology experiments using two-photon targeting described in Chapter 2. (**A**) Area of the spike tuning curve for oDSGCs from control (black, n=61) and DTR (red, n=26) mice (as in **Figure 2.7A**). On average, oDSGCs from DTR mice produced fewer spikes than those from control animals. (**B**) Direction selectivity index for the same cells (as in **Figure 2.7B**). oDSGCs from DTR mice are more sharply tuned. These results match the relationship identified in **Figure 2.7D**. For both panels, data is combined across Superior and Inferior oDSGCs. Numbers with arrows identify the median value for each group. Boxes show IQR and whiskers extend to smallest value within 1.5xIQR. p-values are from rank sum tests.

control conditions may manifest in disease states as sensitivity to degenerative processes. Coupled with the fact that OKR is an approximately linear readout of oDSGC activity, these results position OKR as potentially valuable tool for detecting early signs of disease and degeneration.

Future work will address the full regime of cone loss across which this relationship extends, and the degree to which plasticity mechanisms may be involved. The former can be achieved by titrating DT injections to induce different degrees of cone loss. To test the latter, the empirical nonlinearity can be computed at each degree of cone loss to map the difference in spiking activity between Superior and Inferior oDSGCs onto OKR gain. Changes to this nonlinearity will indicate the presence of post-retinal plasticity; stability will indicate that the AOS may lack the requisite resources or information needed for homeostatic plasticity.

3.3 The translational potential of OKR

The preliminary results presented above are consistent with the hypothesis that OKR can be a sensitive diagnostic tool. Currently, the clinical relevance of OKR is largely restricted to facilitating the diagnosis of several neuro-ophthalmic conditions, including lesions of the oculomotor plant (Leigh and Zee, 2015; London, 1982; Papanagnu and Brodsky, 2014). The present data suggest, however, that OKR may be generally useful for detecting and/or monitoring any disease that affects the retina. This includes many systemic conditions with known retinal manifestations (Aroch et al., 2008; Yap et al., 2019). There is, indeed, a very real possibility of developing diagnostic OKR biomarkers for indications that extend beyond ophthalmic and oculomotor diseases. However, this will not only require improved technology, but also a more complete understanding of the

neurobiology of OKR. In the following sections, I expand on the motivation for OKR-based diagnostics, survey initial work in this field, and discuss several challenges that currently stand in the way of clinical translation.

3.3.1 Diagnostic advantages of OKR

Beyond its apparent sensitivity to small input changes, several qualities of OKR make it an attractive tool for potential diagnostic applications: 1) Evoking OKR is noninvasive and painless. There are also no lasting consequences beyond the potential for acute mild dizziness when viewing optokinetic stimuli for extended periods of time; 2) OKR is an innate behavior, making it relatively easy to measure in noncompliant patients, including children, older adults, and those for whom communication presents barriers to care; 3) OKR is an objective readout. This contrasts with techniques such as subject visual acuity tests or manual clinical assessment, which can suffer from cognitive and cultural bias and human error (Gopal et al., 2021); 4) OKR can be rapidly assessed, with lower costs and resource burdens than other common diagnostic approaches like imaging and tissue sampling; 5) OKR is well conserved across species (Masseck and Hoffmann, 2009), positioning it to be particularly relevant for translational therapeutic research that extends from animal models to human patients. Together, these qualities indicate that if OKR is as sensitive to small input changes in humans as it is in mice, then OKR-based diagnostics may fill a valuable clinical niche.

3.3.2 Previous approaches to OKR-based diagnostics

Progress toward OKR-based diagnostics has been encouraging. Several investigations - spanning decades - have focused on creating OKR tests for visual acuity. Typically, this involves varying the spatial frequency of an optokinetic stimulus to find the

induction (maximum spatial frequency at which OKR gain is greater than a predetermined value), and/or suppression threshold (minimum spatial frequency at which OKR gain is less than a predetermined value). Several groups have reported strong correlations between objective and subjective visual acuity using these methods, including in children and adults with intellectual disabilities (Aleci et al., 2018; Doustkouhi et al., 2020b; Ohm, 1952; Schwob and Palmowski-Wolfe, 2019; Shin et al., 2006; Weder and Wiegand, 1987). In other cases, however, results have been less promising (Çetinkaya et al., 2008; Khan et al., 1976). These inconsistencies highlight the importance of identifying optimal stimulus parameters, outcome measures, and testing environments (Knapp et al., 2013). Khan et al., posited that certain disease states may also invoke homeostatic plasticity mechanisms that restore OKR to baseline levels despite persistent deficits in subjective acuity. This is an intriguing problem because the supposed plasticity mechanisms would evidently be available to subcortical AOS circuitry, but not to the cortical networks involved in subjective acuity tests. Candidate sites and mechanisms are unknown. Knowledge of which disease contexts might promote homeostatic learning in the AOS is also lacking. Further research into the basic neurobiological mechanisms of OKR and AOS plasticity is thus critical to defining clinical use cases.

A smaller body of work has investigated OKR as a diagnostic tool beyond visual acuity. Cleverly designed stimuli have demonstrated that OKR is a sensitive readout of visual field loss (Doustkouhi et al., 2020a) and color vision deficits (Cavanagh et al., 1984; Taore et al., 2022). Multiple Sclerosis (Todd et al., 2001) and Parkinson's disease (Knapp et al., 2009) also affect OKR, though these signatures may be influenced by motor, as opposed to sensory, deficits. Other data indicate diagnostic potential for OKR in diseases

as far stretching as autism spectrum disorders (Kanari and Kikuchi-Ito, 2021; Scharre and Creedon, 1992) and diabetes (Nicholson et al., 2002). However, work in these areas is lacking, and OKR has generally not been well studied in disease contexts where the visual system is not the primary target of pathology.

The sensitivity of OKR to small input changes (Chapter 2) and mild retinal degeneration (Chapter 3.2) provide reason explore its use as a diagnostic biomarker across a broader range of diseases. It is reasonable to hypothesize, for instance, that OKR may be a sensitive biomarker of neurodegenerative diseases with established retinal manifestations, such as Alzheimer's disease (Koronyo et al., 2017). Future work in this area will help 1) improve our understanding of the biology of systemic diseases and their effects on the visual system, and 2) map changes to OKR across different disease contexts in order to improve diagnostic specificity.

3.3.3 Remaining barriers for diagnostic applications of OKR

To leverage the potential of OKR as a diagnostic tool, several persistent challenges must be addressed. In this section, I highlight key outstanding barriers and offer suggestions for future areas of scientific focus.

3.3.3.1 Beyond linear models of OKR. The predictive success of the simple, deterministic subtraction model of vertical OKR in mice (**Figure 2.23**) underscores the idea that it is an innate, reflexive behavior. However, this portrays the simplest case. OKR is less linear, and less reflexive, under several conditions:

1. Exposure to prolonged optokinetic stimulation causes a gain increase (Collewijn and Grootendorst, 1979). The mechanisms of this plasticity have not been fully elucidated, but are likely associated with long term depression in the cerebellum

(Inoshita and Hirano, 2018; Takeuchi et al., 2008). Better understanding, these learning mechanisms, including how they play out in humans, is of critical importance for determining how OKR can be used as a functional readout of visual health. Without improved models, testing regimens that involve prolonged stimulation and repeated longitudinal measurements are likely to confound the diagnostic utility of OKR.

2. OKR gain can be obscured by the vestibular ocular reflex (VOR) when subjects are not headfixed. The interaction between OKR and VOR gain also does not reflect a linear summation (Schweigart et al., 1997). Fleshing out this relationship psychophysically will be important for controlling for the influence of head and body movements on OKR-based tests.
3. Unlike in rodents, human OKR is not always reflexive. Specifically, human subjects can override pure OKR (sometimes called “stare” OKR in this context) with smooth pursuit eye movements and conscious image stabilization referred to as “look” OKR (Knapp et al., 2013, 2008; Valmaggia et al., 2005). Examiner instructions and stimulus designs can influence whether a subject is likely to perform stare or look OKR. Deploying OKR in diagnostic contexts will require developing better methods and standardizations to control which version of the behavior is elicited. If the AOS primarily controls human stare OKR, then stimuli without persistent local spatiotemporal correlations can perhaps minimize the possibility of confounds from smooth pursuit. Significant work is needed to optimize OKR stimuli to collect well-controlled human data.

These confounds may cause OKR to appear less stereotyped than it actually is. Developing more sophisticated, predictive neurobiological models of OKR might help explain behavioral variance that the simple linear subtraction model cannot. Translationally, this will be critical to optimizing stimuli, examination methodologies, and data interpretation. Encouragingly, normative data suggests that, given the right controls, baseline variance across subjects is manageable (Kullmann et al., 2021). The challenge will be to design testing methodologies that can avoid jumps in unexplained inter-subject and inter-examiner variance when transitioned beyond the laboratory.

3.3.3.2 Test specificity. The specificity of a diagnostic test refers to its ability to correctly identify subjects without a disease. Low test specificity can result in a large number of false positives and significantly reduce clinical utility (Monaghan et al., 2021; van Stralen et al., 2009). For translational applications of OKR, it will be important to determine the extent to which a single behavior can differentiate between diseases. For instance, if OKR gain decreases across many neurodegenerative conditions, its inability to help narrow in on a single diagnosis may result in low clinical utility. A possible solution is to design sophisticated stimuli that can reveal particular disease deficits. In the case of OKR testing for color vision, for instance, the stimulus hue and intensity can be used to selectively reveal deficits in color deficient subjects (Taore et al., 2022). Similarly, specificity may be improved by examining differences between an individual subject's responses to a highly salient stimulus and a second stimulus that is designed to reveal a particular disease (e.g., comparing responses to black and white gratings versus colored gratings to identify color vision deficits). Other strategies might involve identifying

additional outcome metrics beyond OKR gain, such as after nystagmus (Bertolini et al., 2021) or temporal lag, to increase the dimensionality of test results.

3.3.3.3 Technologies. OKR is often assessed subjectively in the clinic. In contrast, diagnostic applications will require objective, robust, and repeatable measurements. The resolution of modern eye tracking technologies is sufficient for the majority of conceivable OKR applications (Holmqvist, 2017), but few dedicated devices exist that are easily integrated into clinical workflows. The translation of OKR tests will depend on reliable and easy to use eye tracking solutions. This includes user-friendly hardware as well as turnkey analysis automations that can obfuscate the labor-intensive data analysis that is common in experimental studies (Kiraly et al., 2023; Segura et al., 2018). Ideally, researchers will use the same devices in basic research to develop new applications.

One promising direction in hardware is the potential to use computer monitors, tablets, and smartphones with webcam-based eye tracking (Valliappan et al., 2020; Wisiecka et al., 2022; Yang and Krajbich, 2021). A key advantage of this approach is that it may improve compliance because patients and doctors are likely to already be comfortable with using such devices. Scientifically, however, more work is needed to understand the consequences of presenting OKR stimuli on screens that do not approach full-field (Kveton et al., 1999). It is conceivable that carefully controlling stimulus presentation in both the fovea and periphery, for instance, will be useful in disease contexts like macular degeneration. In such cases, stereoscopic devices such as virtual reality headsets with built-in eye trackers might be a useful hardware choice. Similarly, it is unclear whether tools that do not constrain head and body movements can be reliably

used for OKR measurement. More psychophysical research in human subjects is needed to better inform technology choices and development across diagnostic use cases.

3.4 Conclusion

OKR is a comparatively simple behavior. That simplicity lends itself to the creation of tractable neurobiological models (Chapter 2), which in turn can inform translational applications (Chapter 3). But even in such modesty there is undeniable complexity. Much is left to be discovered, both about the biology of the behavior itself and about how such basic knowledge can be leveraged to reveal neurobiological dysfunction in disease. The ultimate goal will be to map the complete input space onto the complete output space - a sort of functional connectome. This is evidently a formidable challenge, even in the context of a reflexive behavior in mice. But it is also within reach. Fulfilling this goal can position OKR as a template for neuroscience: exposing translational possibilities while revealing the next generation of questions to ask.

3.5 References

Aleci, C., Scaparrotti, M., Fulgori, S., Canavese, L., 2018. A novel and cheap method to correlate subjective and objective visual acuity by using the optokinetic response. Int. Ophthalmol. 38, 2101–2115. https://doi.org/10.1007/s10792-017-0709-x

Aroch, I., Ofri, R., Sutton, G.A., 2008. Ocular Manifestations of Systemic Diseases. Slatters Fundam. Vet. Ophthalmol. 374–418. https://doi.org/10.1016/B978-072160561-6.50021-6

Bertolini, G., Romano, F., Straumann, D., Keller, K., Palla, A., Feddermann-Demont, N., 2021. Measuring optokinetic after-nystagmus: potential for detecting patients with signs of visual dependence following concussion. J. Neurol. 268, 1747–1761. https://doi.org/10.1007/s00415-020-10359-8

Care, R.A., Anastassov, I.A., Kastner, D.B., Kuo, Y.-M., Santina, L.D., Dunn, F.A., 2020. Mature Retina Compensates Functionally for Partial Loss of Rod Photoreceptors. Cell Rep. 31. https://doi.org/10.1016/j.celrep.2020.107730

Care, R.A., Kastner, D.B., De la Huerta, I., Pan, S., Khoche, A., Della Santina, L., Gamlin, C., Santo Tomas, C., Ngo, J., Chen, A., Kuo, Y.-M., Ou, Y., Dunn, F.A., 2019. Partial Cone Loss Triggers Synapse-Specific Remodeling and Spatial Receptive Field Rearrangements in a Mature Retinal Circuit. Cell Rep. 27, 2171-2183.e5. https://doi.org/10.1016/j.celrep.2019.04.065

Cavanagh, P., Anstis, S., Mather, G., 1984. Screening for color blindness using optokinetic nystagmus. Invest. Ophthalmol. Vis. Sci. 25, 463–466.

Çetinkaya, A., Oto, S., Akman, A., Akova, Y.A., 2008. Relationship between optokinetic nystagmus response and recognition visual acuity. Eye 22, 77–81. https://doi.org/10.1038/sj.eye.6702529

Collewijn, H., Grootendorst, A.F., 1979. Adaptation of Optokinetic and Vestibulo-Ocular Reflexes to Modified Visual Input in the Rabbit, in: Granit, R., Pompeiano, O. (Eds.), Progress in Brain Research, Reflex Control of Posture And Movement. Elsevier, pp. 771–781. https://doi.org/10.1016/S0079-6123(08)60874-2

Dakin, S.C., Turnbull, P.R.K., 2016. Similar contrast sensitivity functions measured using psychophysics and optokinetic nystagmus. Sci. Rep. 6, 34514. https://doi.org/10.1038/srep34514

Dhande, O.S., Stafford, B.K., Lim, J.-H.A., Huberman, A.D., 2015. Contributions of Retinal Ganglion Cells to Subcortical Visual Processing and Behaviors. Annu. Rev. Vis. Sci. 1, 291–328. https://doi.org/10.1146/annurev-vision-082114-035502

Donaghy, M., 1980. The contrast sensitivity, spatial resolution and velocity tuning of the cat's optokinetic reflex. J. Physiol. 300, 353–365.

Doustkouhi, S.M., Turnbull, P.R.K., Dakin, S.C., 2020a. The Effect of Simulated Visual Field Loss on Optokinetic Nystagmus. Transl. Vis. Sci. Technol. 9, 25. https://doi.org/10.1167/tvst.9.3.25

Doustkouhi, S.M., Turnbull, P.R.K., Dakin, S.C., 2020b. The effect of refractive error on optokinetic nystagmus. Sci. Rep. 10, 20062. https://doi.org/10.1038/s41598-020-76865-x

Geller, A.M., Sieving, P.A., Green, D.G., 1992. Effect on grating identification of sampling with degenerate arrays. JOSA A 9, 472–477. https://doi.org/10.1364/JOSAA.9.000472

Giolli, R.A., Blanks, R.H.I., Lui, F., 2006. The accessory optic system: basic organization with an update on connectivity, neurochemistry, and function, in: Büttner-Ennever, J.A. (Ed.), Progress in Brain Research, Neuroanatomy of the Oculomotor System. Elsevier, pp. 407–440. https://doi.org/10.1016/S0079-6123(05)51013-6

Gopal, D.P., Chetty, U., O'Donnell, P., Gajria, C., Blackadder-Weinstein, J., 2021. Implicit bias in healthcare: clinical practice, research and decision making. Future Healthc. J. 8, 40. https://doi.org/10.7861/fhj.2020-0233

Harris, S.C., Dunn, F.A., 2023. Asymmetric retinal direction tuning predicts optokinetic eye movements across stimulus conditions. eLife 12, e81780. https://doi.org/10.7554/eLife.81780

Holmqvist, K., 2017. Common predictors of accuracy, precision and data loss in 12 eye-trackers. https://doi.org/10.13140/RG.2.2.16805.22246

Inoshita, T., Hirano, T., 2018. Occurrence of long-term depression in the cerebellar flocculus during adaptation of optokinetic response. eLife 7, e36209. https://doi.org/10.7554/eLife.36209

Kanari, K., Kikuchi-Ito, M., 2021. Estimation of the degree of autism spectrum disorder by the slow phase of optokinetic nystagmus in typical adults. Heliyon 7, e07751. https://doi.org/10.1016/j.heliyon.2021.e07751

Khan, S.G., Chen, K.F.-C., Frenkel, M., 1976. Subjective and Objective Visual Acuity Testing Techniques. Arch. Ophthalmol. 94, 2086–2091. https://doi.org/10.1001/archopht.1976.03910040746009

Kiebel, S., 2009. Cortical circuits for perceptual inference. Neural Netw., Cortical Microcircuits 22, 1093–1104. https://doi.org/10.1016/j.neunet.2009.07.023

Kiraly, J.K., Harris, S.C., Al-Khindi, T., Dunn, F.A., Kolodkin, A., 2023. A semi-automated method for quantifying optokinetic reflex tracking acuity. BioRxiv Prepr. Serv. Biol. 2023.08.03.551461. https://doi.org/10.1101/2023.08.03.551461

Knapp, C.M., Gottlob, I., McLean, R.J., Proudlock, F.A., 2008. Horizontal and Vertical Look and Stare Optokinetic Nystagmus Symmetry in Healthy Adult Volunteers. Invest. Ophthalmol. Vis. Sci. 49, 581–588. https://doi.org/10.1167/iovs.07-0773

Knapp, C.M., Gottlob, I., McLean, R.J., Rajabally, Y.A., Abbott, R.J., Rafelt, S., Proudlock, F.A., 2009. Vertical optokinetic nystagmus in Parkinson's disease. Mov. Disord. 24, 1533–1538. https://doi.org/10.1002/mds.22634

Knapp, C.M., Proudlock, F.A., Gottlob, I., 2013. OKN Asymmetry in Human Subjects: A Literature Review. Strabismus 21, 37–49. https://doi.org/10.3109/09273972.2012.762532

Knorr, A.G., Gravot, C.M., Glasauer, S., Straka, H., 2021. Image motion with color contrast suffices to elicit an optokinetic reflex in Xenopus laevis tadpoles. Sci. Rep. 11, 8445. https://doi.org/10.1038/s41598-021-87835-2

Koronyo, Y., Biggs, D., Barron, E., Boyer, D.S., Pearlman, J.A., Au, W.J., Kile, S.J., Blanco, A., Fuchs, D.-T., Ashfaq, A., Frautschy, S., Cole, G.M., Miller, C.A., Hinton, D.R., Verdooner, S.R., Black, K.L., Koronyo-Hamaoui, M., 2017. Retinal amyloid

pathology and proof-of-concept imaging trial in Alzheimer's disease. JCI Insight 2. https://doi.org/10.1172/jci.insight.93621

Kullmann, A., Ashmore, R.C., Braverman, A., Mazur, C., Snapp, H., Williams, E., Szczupak, M., Murphy, S., Marshall, K., Crawford, J., Balaban, C.D., Hoffer, M., Kiderman, A., 2021. Normative data for ages 18-45 for ocular motor and vestibular testing using eye tracking. Laryngoscope Investig. Otolaryngol. 6, 1116–1127. https://doi.org/10.1002/lio2.632

Kveton, J.F., Limb, C.J., Bell, M.D., 1999. Comparison of optokinetic nystagmus elicited by full versus partial visual field stimulation: diagnostic implications. Otolaryngol.--Head Neck Surg. Off. J. Am. Acad. Otolaryngol.-Head Neck Surg. 121, 52–56. https://doi.org/10.1016/S0194-5998(99)70124-5

Lee, J.Y., Care, R.A., Kastner, D.B., Della Santina, L., Dunn, F.A., 2022. Inhibition, but not excitation, recovers from partial cone loss with greater spatiotemporal integration, synapse density, and frequency. Cell Rep. 38, 110317. https://doi.org/10.1016/j.celrep.2022.110317

Leguire, L.E., Zaff, B.S., Freeman, S., Rogers, G.L., Bremer, D.L., Wali, N., 1991. Contrast sensitivity of optokinetic nystagmus. Vision Res. 31, 89–97. https://doi.org/10.1016/0042-6989(91)90076-H

Leigh, R.J., Zee, D.S., 2015. The Neurology of Eye Movements. Oxford University Press.

London, R., 1982. Optokinetic nystagmus: a review of pathways, techniques and selected diagnostic applications. J. Am. Optom. Assoc. 53, 791–798.

Masseck, O.A., Hoffmann, K.-P., 2009. Comparative Neurobiology of the Optokinetic Reflex. Ann. N. Y. Acad. Sci. 1164, 430–439. https://doi.org/10.1111/j.1749-6632.2009.03854.x

Monaghan, T.F., Rahman, S.N., Agudelo, C.W., Wein, A.J., Lazar, J.M., Everaert, K., Dmochowski, R.R., 2021. Foundational Statistical Principles in Medical Research: Sensitivity, Specificity, Positive Predictive Value, and Negative Predictive Value. Medicina (Mex.) 57, 503. https://doi.org/10.3390/medicina57050503

Nadal-Nicolás, F.M., Kunze, V.P., Ball, J.M., Peng, B.T., Krishnan, A., Zhou, G., Dong, L., Li, W., 2020. True S-cones are concentrated in the ventral mouse retina and wired for color detection in the upper visual field. eLife 9, e56840. https://doi.org/10.7554/eLife.56840

Naoi, M., Maruyama, W., 1999. Cell death of dopamine neurons in aging and Parkinson's disease. Mech. Ageing Dev. 111, 175–188. https://doi.org/10.1016/S0047-6374(99)00064-0

Nicholson, M., King, J., Smith, P.F., Darlington, C.L., 2002. Vestibulo-ocular, optokinetic and postural function in diabetes mellitus. NeuroReport 13, 153.

Ohm, J., 1952. Use of moving signs in connection with optokinetic nystagmus in order to determine the visual acuity objectively. Klin. Monatsblatter Augenheilkd. Augenarztliche Fortbild. 120, 144–150.

Papanagnu, E., Brodsky, M.C., 2014. Is There a Role for Optokinetic Nystagmus Testing in Contemporary Orthoptic Practice? Old Tricks and New Perspectives. Am. Orthopt. J. 64, 1–10. https://doi.org/10.3368/aoj.64.1.1

Ratnam, K., Carroll, J., Porco, T.C., Duncan, J.L., Roorda, A., 2013. Relationship Between Foveal Cone Structure and Clinical Measures of Visual Function in Patients With Inherited Retinal Degenerations. Invest. Ophthalmol. Vis. Sci. 54, 5836–5847. https://doi.org/10.1167/iovs.13-12557

Santina, L.D., Yu, A.K., Harris, S.C., Soliño, M., Ruiz, T.G., Most, J., Kuo, Y.-M., Dunn, F.A., Ou, Y., 2021. Disassembly and rewiring of a mature converging excitatory circuit following injury. Cell Rep. 36. https://doi.org/10.1016/j.celrep.2021.109463

Scharre, J.E., Creedon, M.P., 1992. Assessment of Visual Function in Autistic Children. Optom. Vis. Sci. 69, 433.

Schweigart, G., Mergner, T., Evdokimidis, I., Morand, S., Becker, W., 1997. Gaze Stabilization by Optokinetic Reflex (OKR) and Vestibulo-ocular Reflex (VOR) During Active Head Rotation in Man. Vision Res. 37, 1643–1652. https://doi.org/10.1016/S0042-6989(96)00315-X

Schwob, N., Palmowski-Wolfe, A., 2019. Objective measurement of visual acuity by optokinetic nystagmus suppression in children and adult patients. J. Am. Assoc. Pediatr. Ophthalmol. Strabismus 23, 272.e1-272.e6. https://doi.org/10.1016/j.jaapos.2019.05.016

Segura, F., Arines, J., Sánchez-Cano, A., Perdices, L., Orduna-Hospital, E., Fuentes-Broto, L., Pinilla, I., 2018. Development of optokinetic tracking software for objective evaluation of visual function in rodents. Sci. Rep. 8, 10009. https://doi.org/10.1038/s41598-018-28394-x

Shannon, C.E., 1948. A mathematical theory of communication. Bell Syst. Tech. J. 27, 379–423. https://doi.org/10.1002/j.1538-7305.1948.tb01338.x

Shen, N., Wang, B., Soto, F., Kerschensteiner, D., 2020. Homeostatic Plasticity Shapes the Retinal Response to Photoreceptor Degeneration. Curr. Biol. S0960982220303717. https://doi.org/10.1016/j.cub.2020.03.033

Shin, Y.J., Park, K.H., Hwang, J.-M., Wee, W.R., Lee, J.H., Lee, I.B., 2006. Objective Measurement of Visual Acuity by Optokinetic Response Determination in Patients With Ocular Diseases. Am. J. Ophthalmol. 141, 327–332. https://doi.org/10.1016/j.ajo.2005.09.025

Simpson, J.I., 1984. The Accessory Optic System. Annu. Rev. Neurosci. 7, 13–41. https://doi.org/10.1146/annurev.ne.07.030184.000305

Takeuchi, T., Ohtsuki, G., Yoshida, T., Fukaya, M., Wainai, T., Yamashita, M., Yamazaki, Y., Mori, H., Sakimura, K., Kawamoto, S., Watanabe, M., Hirano, T., Mishina, M., 2008. Enhancement of Both Long-Term Depression Induction and Optokinetic Response Adaptation in Mice Lacking Delphilin. PLOS ONE 3, e2297. https://doi.org/10.1371/journal.pone.0002297

Taore, A., Lobo, G., Turnbull, P.R., Dakin, S.C., 2022. Diagnosis of colour vision deficits using eye movements. Sci. Rep. 12, 7734. https://doi.org/10.1038/s41598-022-11152-5

Todd, L., King, J., Darlington, C.L., Smith, P.F., 2001. Optokinetic reflex dysfunction in multiple sclerosis. NeuroReport 12, 1399.

Valliappan, N., Dai, N., Steinberg, E., He, J., Rogers, K., Ramachandran, V., Xu, P., Shojaeizadeh, M., Guo, L., Kohlhoff, K., Navalpakkam, V., 2020. Accelerating eye movement research via accurate and affordable smartphone eye tracking. Nat. Commun. 11, 4553. https://doi.org/10.1038/s41467-020-18360-5

Valmaggia, C., Proudlock, F., Gottlob, I., 2005. Look and stare optokinetic nystagmus in healthy subjects and in patients with no measurable binocularity. A prospective study. Klin. Monatsbl. Augenheilkd. 222, 196–201. https://doi.org/10.1055/s-2005-858013

van Stralen, K.J., Stel, V.S., Reitsma, J.B., Dekker, F.W., Zoccali, C., Jager, K.J., 2009. Diagnostic methods I: sensitivity, specificity, and other measures of accuracy. Kidney Int. 75, 1257–1263. https://doi.org/10.1038/ki.2009.92

Weder, W., Wiegand, H., 1987. Determination of visual acuity using optokinetic nystagmus. A newly developed instrument based on Günther's principle. Klin. Monatsbl. Augenheilkd. 191, 149–155. https://doi.org/10.1055/s-2008-1050487

Wisiecka, K., Krejtz, K., Krejtz, I., Sromek, D., Cellary, A., Lewandowska, B., Duchowski, A., 2022. Comparison of Webcam and Remote Eye Tracking, in: 2022 Symposium on Eye Tracking Research and Applications, ETRA '22. Association for Computing Machinery, New York, NY, USA, pp. 1–7. https://doi.org/10.1145/3517031.3529615

Yang, X., Krajbich, I., 2021. Webcam-based online eye-tracking for behavioral research. Judgm. Decis. Mak. 16, 1485–1505. https://doi.org/10.1017/S1930297500008512

Yap, T.E., Balendra, S.I., Almonte, M.T., Cordeiro, M.F., 2019. Retinal correlates of neurological disorders. Ther. Adv. Chronic Dis. 10, 2040622319882205. https://doi.org/10.1177/2040622319882205

Publishing Agreement

It is the policy of the University to encourage open access and broad distribution of all theses, dissertations, and manuscripts. The Graduate Division will facilitate the distribution of UCSF theses, dissertations, and manuscripts to the UCSF Library for open access and distribution. UCSF will make such theses, dissertations, and manuscripts accessible to the public and will take reasonable steps to preserve these works in perpetuity.

I hereby grant the non-exclusive, perpetual right to The Regents of the University of California to reproduce, publicly display, distribute, preserve, and publish copies of my thesis, dissertation, or manuscript in any form or media, now existing or later derived, including access online for teaching, research, and public service purposes.

DocuSigned by:
FA028174355C465...
Author Signature

5/23/2024
Date